

FINITE ELEMENT BASED METHODOLOGY FOR  
PREDICTION OF MATRIX-DOMINATED  
FAILURE IN COMPOSITES

by

GUILLAUME SEON

Presented to the Faculty of the Graduate School of  
The University of Texas at Arlington in Partial Fulfillment  
of the Requirements  
for the Degree of

DOCTOR OF PHILOSOPHY

THE UNIVERSITY OF TEXAS AT ARLINGTON

May 2014

Copyright © by Guillaume Seon 2014

All Rights Reserved





To my dear and missed sister, Laure

## Acknowledgements

First and foremost, I would like to express my deepest gratitude to my advisor Dr. Andrew Makeev, for his wonderful guidance and support during these years. Dr. Makeev inspired me to step into composite materials at the beginning of this journey, when I first had the opportunity to work under his supervision at the Georgia Institute of Technology in Atlanta. Since then, his scientific instinct and tremendous enthusiasm have never stopped to amaze me. His advice and guidance, as well as his wide knowledge in composite material science, truly are the backbone of this work. His experience and perspective, which he shared with me over the last few years, have enriched me far beyond academic grounds. I could not have asked for a better experience while pursuing my graduate education. I will always consider Dr. Makeev as a mentor and a friend.

I am deeply indebted to faculty research engineer Dr. Yuri Nikishkov and would like to personally thank him for his invaluable contributions, especially his help with some of the scripts used in this work for FEM analysis and measurements of CT data. I would like to add that working with Dr. Nikishkov has been a great pleasure and I have truly appreciated and enjoyed all the impromptu, enlightened conversations, and time spent with Dr. Nikishkov scrutinizing X-Ray CT scans in search for failure patterns and defects in composites. I would like to thank Dr. Erian Armanios for being influential in my decision to pursue my education with a doctoral degree and for all his kindness and encouragement. I also want to thank the rest of my committee members, Dr. Haiying Huang, Dr. Kent Lawrence and Dr. Wen Chan, for their valuable comments and suggestions.

Additionally, I would like to express my extreme gratitude to Brian Shonkwiller, Dr. Paige Carpentier and Julia Cline for their invaluable contribution to the experimental work used in this research. I also wish to thank the rest of my colleagues and friends at

the University of Texas at Arlington, and especially Ekatarina Bostaph and Michael Tadros, for making this experience so memorable.

Finally, I wish to thank all the persons close to me, family and friends, for their encouragements and love. I am grateful to Moraima Guzman for sharing with me many aspects of my doctoral journey. I would also like to thank my dear parents, Odile and Roland Seon, for their unconditional support on all my decisions and choices. My gratitude also goes to my grandparents, Monique and Guy Dupas, for their persisting encouragement; I will always remember all the cross-Atlantic telephone conversations with my grandfather Guy, as he was continually inquiring about my progress and research findings during my graduate studies abroad.

This work was sponsored by the Office of Naval Research and the Army Vertical Lift Research Center of Excellence; such support is gratefully acknowledged.

April 21, 2014

## Abstract

# FINITE ELEMENT BASED METHODOLOGY FOR PREDICTION OF MATRIX-DOMINATED FAILURE IN COMPOSITES

Guillaume Seon, PhD

The University of Texas at Arlington, 2014

Supervising Professor: Andrew Makeev

The objective of this work is to develop a computational failure prognosis methodology applicable to virtual testing of composites. The major motivation for the establishment of virtual testing is the ability to reduce actual testing of composite structures, which is oftentimes expensive and time consuming, by numerical simulations. A successful virtual test methodology should be applicable to monotonic and fatigue loading, account for strong anisotropy of composite materials and capture the effects of manufacturing irregularities. This work proposes to use three-dimensional finite element modelling for predicting the onset and progression of matrix-dominated failures modes, such as matrix cracks and delaminations, which are the primary modes of failure in composite laminates utilized in aerospace composite structural designs. The ability of the method to predict strength, damage topography and fatigue cycles to failure is verified using actual standard tests of multi-directional laminates. High-fidelity nondestructive inspection techniques, based on micro-focus X-Ray computed tomography, are used to integrate manufacturing defects including porosity/voids into finite element models, and contribute to greater understanding of the effects of defects on the strength and fatigue

performance of composites. Finally, the ability to transition the methodology, developed and verified at the material scale, to larger composite structural elements is evaluated.

## Table of Contents

Acknowledgements .....	iv
Abstract.....	vi
List of Illustrations .....	xii
List of Tables.....	xviii
Chapter 1 Introduction.....	1
1.1 Motivation .....	1
1.2 Outline .....	5
1.3 Literature Survey.....	7
1.3.1 Stress-based Failure Predictions in Composites .....	7
1.3.2 Progressive Damage .....	8
1.3.3 Progressive Fatigue Failure.....	10
1.3.4 Effects of Manufacturing Defects.....	12
Chapter 2 Constitutive Model and Failure Criteria.....	16
2.1 Governing Length Scale .....	16
2.2 Constitutive Model .....	18
2.2.1 Explicit Modelling.....	18
2.2.2 Material Constitutive Properties.....	19
2.2.2.1 Stress-strain Relations .....	19
2.2.2.2 Strength Properties .....	22
2.3 Failure Criteria .....	22
2.3.1 Transverse Tensile Matrix Failure .....	23
2.3.2 Transverse Compressive Matrix Failure .....	25
2.3.3 Fiber Compressive Failure .....	27
2.3.4 Delamination .....	29

2.4 Recovery of Interlaminar Stresses.....	31
2.4.1 Stress Recovery Procedure.....	31
2.4.2 Benchmark Validation.....	34
Chapter 3 Progressive Failure .....	38
3.1 Failure Damage Progression .....	39
3.2 Mesh Dependency .....	43
3.3 Fatigue Damage Progression Algorithm .....	47
3.4 Failure Predictions for Open-hole Tension Specimens .....	49
3.4.1 FE Model.....	50
3.4.2 Static Failure of OHT Coupons.....	52
3.4.2.1 Test Results .....	52
3.4.2.2 FE Simulations and Test Correlations.....	53
3.4.3 Fatigue of OHT Coupons.....	56
3.4.3.1 Fatigue Tests and Calibration of the FE Model .....	56
3.4.3.2 Fatigue Progression of Three-dimensional Damage and Interaction .....	60
3.4.3.3 Fatigue Prediction for Different Peak Loads.....	63
3.5 Failure Predictions for Open-hole Compression Specimens.....	65
3.5.1 Damage Model for Compressive Failure .....	65
3.5.2 Static Failure of OHC Coupons .....	68
3.5.2.1 Tests and FE Results.....	68
3.5.2.2 Correlation with X-Ray Micro-CT Inspection .....	73
Chapter 4 Integration of Manufacturing Defects.....	76
4.1 Non-destructive Inspection of Manufacturing Defects by X-Ray Tomography.....	76

4.2 Measurement of the Three-dimensional Defect Geometry .....	80
4.3 Effect of Porosity Defects on Interlaminar Tension Performances .....	84
4.3.1 Curved-beam Test.....	84
4.3.2 Interlaminar Tensile Strength .....	86
4.3.3 Interlaminar Tensile Fatigue S-N Curve .....	92
4.4 Refinement of the Curved-beam Test Method to Account for Porosity .....	95
4.4.1 Local Stress Analysis .....	95
4.4.2 Refinement of the ILTS by Integration of Defects.....	97
4.4.3 Comparison with ILT Short-Beam Test.....	105
4.4.4 Application to ILT Fatigue Behavior.....	109
Chapter 5 Transition to the Structural Scale .....	112
5.1 Structural Test Articles.....	113
5.2 Measurements of Defects .....	115
5.3 Methodology for Failure Predictions.....	119
5.3.1 Principle.....	119
5.3.2 Global Model .....	120
5.3.3 Local Model .....	123
5.4 Local Meshing of Defect Areas .....	124
5.4.1 Mesh Morphing Technique .....	124
5.4.2 Mesh Morphing in Cartesian and Polar Coordinates .....	125
5.4.3 Meshing of Defects with In-plane Fiber Waviness.....	127
5.4.4 Meshing of Defects with Out-of-plane Waviness .....	130
5.5 Failure Predictions in Caron/Epoxy Flapping Specimens .....	132
5.5.1 Predictions of Static Failure in Defect-free Specimens.....	132
5.5.2 Failure Prediction Using the Local Model .....	135



5.5.3 Predictions of Fatigue Failure .....	138
5.5.4 Summary of Failure Predictions .....	139
Chapter 6 Conclusion and Future Work .....	141
Appendix A Determination of the Number of Cycles to Failure for Matrix	
Tensile Failure.....	147
Appendix B Generation of a Circular Oriented Mesh .....	150
References.....	155
Biographical Information .....	162

## List of Illustrations

Figure 2-1 Three levels of FE representation of laminated composites .....	16
Figure 2-2 Schematic view of the fracture plane for transverse tensile matrix failure.....	23
Figure 2-3 Schematic view of the fracture plane for transverse compressive matrix failure (left) and components of the stress tensor acting on the fracture plane (right) .....	25
Figure 2-4 Fiber misalignment frame $m$ for fiber kinking .....	28
Figure 2-5 Schematic view of the fracture plane for delamination failure in the delamination layer .....	30
Figure 2-6 Interlaminar nodal forces at the interface between ply (1) and ply (2) .....	32
Figure 2-7 Geometry (left) and FE model (right) for the $[+45/-45]_S$ axial extension laminate benchmark problem .....	34
Figure 2-8 Comparison of normal interlaminar stress $\sigma_{yy}$ at $+45/-45$ interface for axial extension of $[+45/-45]_S$ laminate .....	36
Figure 2-9 Comparison of shear interlaminar stress $\sigma_{xy}$ at $+45/-45$ interface for axial extension of $[+45/-45]_S$ laminate .....	36
Figure 3-1 Propagation of matrix cracks in a radially oriented submodel mesh for 90 degree surface ply in a $[45/0/-45/90]_{2S}$ OHT coupon.....	44
Figure 3-2 Propagation of matrix cracks in a fiber-oriented submodel mesh for 90 degree and 45 degree plies in OHT coupon.....	46
Figure 3-3 Global and local fiber-aligned oriented FE mesh for Open Hole coupon .....	50
Figure 3-4 Sub-model with fiber-oriented mesh and detail of through-the-thickness discretization .....	52
Figure 3-5 Surface-ply ultimate failure cracks in OHT coupons .....	53
Figure 3-6 Surface strains at 22.41 kN (5037 lb) tensile load .....	55
Figure 3-7 Surface strains at 32.20 kN (7239 lb) tensile load .....	55

Figure 3-8 2D X-Ray images and simulation results for matrix cracks .....	56
Figure 3-9 DIC and FEM based measurement of the longest matrix crack length in surface 45 degree ply of OHT specimen at 1,000,000 cycles .....	58
Figure 3-10 Comparison of the longest surface crack fatigue growth for different FE crack band width $e$ and correlation with tests .....	58
Figure 3-11 Comparison of the longest surface crack fatigue growth for different number of failed elements per fatigue step .....	59
Figure 3-12 Comparison of FE fatigue failure predictions and CT scan of test specimen for layup 1 .....	61
Figure 3-13 Matrix cracks in 45 degree surface ply and delamination in the sub-surface interface for FE predictions and CT data for layup 1 specimen at 1,000,000 cycles .....	62
Figure 3-14 Matrix cracks in 45-degree surface ply and delamination in the sub-surface interface for FE predictions and CT data for layup 2 specimen at 1,000,000 cycles .....	63
Figure 3-15 Comparison of FE predictions (top) and CT scans (bottom) for surface matrix crack and sub-surface delaminations for layup 2 specimens .....	64
Figure 3-16 3D CT reconstruction of OHC specimen showing structural damage after 10,000 lbs (44.5 kN) compressive loading .....	69
Figure 3-17 Development of matrix compression cracks and compressive fiber failure (dark grey) and delaminations (lighter grey) in OHC surface $0^\circ$ ply .....	70
Figure 3-18 Development of matrix cracks (dark grey) and delaminations (lighter grey) in OHC first sub-surface $45^\circ$ ply .....	71
Figure 3-19 Integrated load frame for CT scan under load .....	74
Figure 3-20 Comparison of FE predictions and CT data under loading for OHC specimens .....	75
Figure 4-1 North Star Imaging industrial micro-CT system .....	77

Figure 4-2 Operation basics and major components of the CT system.....	78
Figure 4-3 Cross-section CT slides of carbon/epoxy unidirectional curved beam specimens manufactured at a) 80 psi curing pressure (nominal) and b) 25 psi showing porosity defects. ....	79
Figure 4-4 Pixel histogram for a Carbon/Epoxy specimen and determination of the gray value threshold for air/material separation .....	81
Figure 4-5 Elliptical fits in cylindrical coordinates (in red) for the detection of porosity voids in cross-section CT images of unidirectional carbon/epoxy curved beam specimens .....	83
Figure 4-6 ASTM D 6415 test setup and tensile delamination failure of a unidirectional Carbon/Epoxy curved-beam specimen .....	85
Figure 4-7 FE-based ILT stress distribution in the radius area of the curved-beam specimen at 232 lbs (1.03 kN).....	89
Figure 4-8 Delamination crack passing through critical voids in the radius area of the curved-beam specimens .....	89
Figure 4-9 Dependency of curved-beam failure load on the area of the critical void.....	91
Figure 4-10 Examples of delaminations in IM7/8552 curved-beam fatigue specimens...	93
Figure 4-11 ILT S-N curve based on the ASTM D 6414 ILT stress approximation .....	94
Figure 4-12 Details of the void geometry in the CT scans of curved-beam specimens...	96
Figure 4-13 3D structured FE global mesh of a curved-beam coupon and a local submodel of the critical void.....	97
Figure 4-14 ILT stress concentration at the edges of the critical void (left) and decrease of ILT stress versus the radial distance from the void surface (right) .....	99
Figure 4-15 Location of the maximum ILT stress and the maximum interlaminar shear (ILS) stress at the surface of the critical void .....	100

Figure 4-16 ILT stresses as a function of the distance from the critical void for the ten IM7/8552 curved-beam specimens for the point-stress method.....	101
Figure 4-17 ILT stresses as a function of the distance from the critical void for the ten IM7/8552 curved-beam specimens for the average-stress method.....	102
Figure 4-18 Average ILT strength (ILTS) and COV as a function of radial distance from the void surface in the point-stress method.....	103
Figure 4-19 Average ILT strength (ILTS) and COV as a function of radial distance from the void surface in the average-stress method .....	104
Figure 4-20 A short-beam method to measure multiple stress-strain properties of composites: specimen configurations, test setup, and measured strains (DIC) .....	106
Figure 4-21 Failure modes of short-beam specimens .....	106
Figure 4-22 Refined ILT S-N curve based on the point-stress method (19 $\mu$ m characteristic distance) .....	110
Figure 4-23 Refined ILT S-N curve based on the average-stress method (19 $\mu$ m characteristic distance) .....	110
Figure 5-1 Flapping element in a three-point bend test setup with bolted fixture (top) and geometry details (bottom) .....	113
Figure 5-2 Flapping element under bending loading with surface spray-painted for DIC strain measurements (left) and DIC interlaminar shear strain field showing delamination crack at failure load (right).....	114
Figure 5-3 CT scan details in S2/8552 Glass/Epoxy flapping element showing out-of-plane (top right) and in-plane (bottom right) fiber waviness around a seeded void defect .....	116

Figure 5-4 CT scan details in IM7/8552 Carbon/Epoxy flapping element showing out-of-plane (top right) and in-plane (bottom right) fiber waviness around a seeded void defect .....	117
Figure 5-5 Global FE model of the flapping specimen .....	121
Figure 5-6 Comparison of FE-based global load-displacement response with test results for Glass/Epoxy flapping specimens .....	122
Figure 5-7 Comparison of FE-based and DIC test measurements for global interlaminar surface shear strain field in Glass/Epoxy flapping specimens at 1350 lbs (6.0 kN) .....	122
Figure 5-8 CT data (left) and approximation of the void 3D surface using density-based contouring (right) for a seeded porosity defect in the flapping specimens.....	123
Figure 5-9 Source and target mesh for morphing in Cartesian coordinates .....	125
Figure 5-10 Source and target mesh for morphing in polar coordinates .....	127
Figure 5-11 Source and target mesh for the composite material (top) and resin-rich area (bottom) for one ply layer of the local FE model with in-plane fiber waviness .....	128
Figure 5-12 Local fiber orientation around the defect in the local FE model with in-plane fiber waviness .....	129
Figure 5-13 Assembly of oriented ply layers and cross-section of the local FE model with in-plane fiber waviness.....	130
Figure 5-14 Source and target mesh for the composite material (top) and resin-rich area (bottom) for one ply layer of the local FE model with out-of-plane ply waviness .....	131
Figure 5-15 Assembly of ply layers and cross-section of the local FE model with out-of-plane ply waviness .....	131
Figure 5-16 Interlaminar shear stress concentration in the global FE model for IM7/8552 flapping element at 4100 lbs (18.2 kN).....	133

Figure 5-17 LaRC04 failure criteria in the defect-free global FE mesh for IM7/8552 flapping element at 5640 lbs (25.1 kN).....	133
Figure 5-18 LaRC04 failure criteria calculated from stresses at element integration points (top) and using the interlaminar stress-recovery procedure (bottom) at two critical 0°/45° ply interfaces .....	134
Figure 5-19 Cross-section cut showing local mesh of the critical defect embedded in the global FE mesh .....	135
Figure 5-20 LaRC04 failure criteria for the defect-free global model (top) and embedded local model with defect (bottom) at the same cross-section of specimen L3 at 5050 lbs (22.5 kN) .....	137
Figure 5-21 Failed void section of the CT scan of L3 specimen (failed at 4900lbs (21.8 kN)) .....	137
Figure 5-22 . Contour plot of the Log(number of cycles to failure) in the local model for specimen R3b (left) and comparison with the crack location from the CT data (right). The contour plot from FEM simulation is superimposed using transparency on the CT image (right).....	139

## List of Tables

Table 3-1 Cross-section dimensions and failure load for static OHT coupons .....	53
Table 3-2 FEM-based and actual test loads for various stages of matrix cracking .....	56
Table 3-3 Comparison of simulation and test measurements for surface crack lengths and delaminations in OHT fatigue articles.....	65
Table 3-4 FE-based simulation of matrix cracks and fiber failure developments in OHC specimens .....	72
Table 4-1 Failure load and ASTM D 6415 ILTS for IM7/8552 curved-beam specimens .	88
Table 4-2 ASTM D 6415 and refined ILTS for curved-beam specimens with porosity defects .....	104
Table 5-1 Comparison between FE simulation and test data for static and fatigue failures of IM7/8552 flapping elements .....	140



## Chapter 1

### Introduction

#### 1.1 Motivation

Fiber reinforced polymer-matrix composites have been increasingly used in the aerospace industry due to their low weight, increased durability and the potential for elastic tailoring making them desirable for replacement of conventional metallic structures. However, the ability to predict structural failure of composite materials is challenging due to their complex nature, including strong anisotropy and manufacturing flaws. Failure of laminated composites typically involves multiple failure mechanisms and their interaction. Matrix-dominated failure modes, such as matrix cracks and delaminations, are the primary source of structural damage for flight-critical and fatigue-critical aircraft composite structures.

Assessment of structural performance of composite structures used in aerospace structural designs by testing alone can be prohibitively expensive due to the large amount of tests required to characterize all key material properties, structural configurations and loading scenarios. Multiple standard test types are required to characterize the material constitutive properties of any new composite system. Coupon tests at the material scale are conducted to cover all material layups and stress states anticipated in the structure, including response to monotonic, fatigue, impact loading and environmental constraints such as high temperatures. Coupon tests are followed by tests of larger elements, subcomponents, and components. Tests of structures up to the full scale are required to achieve structural certification [1].

The motivation of this work is the need in the development of computational prediction methodologies for matrix-dominated failures in composites used in aerospace

structural designs. The use of computational models for predicting deformation, damage topography, strength, and cycles to failure in composites, or “virtual tests” as advocated by Brian Cox [2], can significantly reduce development costs by replacing some of the physical tests while providing valuable insight to achieve optimized designs. The objective is to contribute to the development of a reliable computational methodology that captures essential physics with a minimum amount of complexity and provides failure prediction ability useful for the design of composite structures.

Improvements in computer hardware have led to a growing interest in using Finite Element (FE) models for prediction of failure in composites. In particular, three-dimensional (3D) solid FE analysis can become a practical tool to capture the complex interaction between in-ply and interlaminar matrix-dominated failure mechanisms, such as matrix cracking and delamination, for the most complex combinations of geometry, loading, material system or layup. Recent developments of material characterization methods based on full-field measurements of deformation for assessment of 3D material constitutive properties of composite materials [3-6], including in-plane and interlaminar shear stress-strain non-linear relations and strength, can serve as the basis for the development of a 3D FE stress-based failure analysis methodology. Stress-based failure criteria that consider each failure mechanism separately, such as the set of LaRC criteria proposed by Davila et al. [29], have achieved wide acceptance and are used in this work for prediction of failure initiation in multidirectional composite laminates. Defining composite failure as the onset of damage might prove overly conservative, since composites usually exhibit significant residual structural capability after first failure event. Prediction of damage progression to significant (detectable) size that captures the interaction and interlaminar matrix-dominated failure modes is necessary for accurate assessment of the residual capability and useful life of composite parts. In this work, a

comprehensive structural analysis methodology that does not require a priori assumptions of the initial damage or the damage propagation path, is implemented at the material scale and validated for standard multidirectional laminated composite test coupons.

One of the major challenges in the design of composite structures for both fixed-wing and rotary-wing aircraft applications is also the ability to predict their performance under cyclic loads. In particular, helicopter rotor systems are subject to extreme fatigue environments. Fatigue capability is a limiting factor for high-cycle components found in helicopter dynamic systems [7]. Typical examples of fatigue-critical primary composite structures include main rotor blade spars and yokes in commercial and military helicopters [8]. In this work, progressive failure models are extended to fatigue loading for predictions of fatigue damage progression and failure modes interactions in open-hole laminate coupons.

Accurate strength material properties are essential for the development of stress-based failure prediction methods. However, due to their sensitivity to manufacturing defects, strength properties can be difficult to determine and standard test results may reflect manufacturing quality as much as material properties. The sensitivity of composite materials behavior to defects has motivated many researchers to apply fracture mechanics concepts to composite failure, as an alternative to the strength-based approach. If fracture-based methods have been successful in the study of delamination and debonding [18], there are obstacles to their implementation into a virtual test methodology. Fracture mechanics analyses typically require assumptions of initial crack length; and not all fracture mechanics parameters are currently able to be determined reliably by existing test methods. Such restrictions limit the applicability of fracture mechanics to virtual testing. On the other hand, recent advances in non-destructive

inspection techniques, such as micro-focus X-Ray Computed Tomography (CT), allow for high-fidelity detection and measurements of defects and show strong potential in providing valuable information for improved understanding of structural response of composites in presence of manufacturing defects. Although it might not be practical to eliminate all defects in a composite part, it is possible to avoid assumptions of the worst-case scenario and address improved part durability and damage tolerance once the defects and their effects are captured. Advanced structural methods that account for manufacturing defects in composite parts are needed to enable accurate assessment of their capability and useful life and enhance current design and maintenance practices. In this work, CT measurements of defects in composites are transferred into the FE models used in the failure prediction methodology for integration of the defects and assessment of their effects on structural performances.

One of the remaining key questions is related to the ability of transitioning the virtual test methodology developed at the material scale to larger composite structures. Are laminate-scale virtual tests sufficient to predict failure of larger-scale structures? Indeed, structures might have phenomena not encountered in smaller coupons, and therefore transition of material information might be challenging. The results of a feasibility assessment targeting the scaling of knowledge and methods acquired at the material scale, to larger structural elements are presented in this work.

## 1.2 Outline

The remainder of this thesis develops as follows.

The constitutive model derived at the ply-scale and implemented in FE models using ABAQUS FE software is presented in Chapter 2. The LaRC failure criteria proposed by Davila et al. [29] are used in this work for prediction of initiation of matrix-dominated failures. The LaRC failure criterion for tensile matrix cracking is extended for prediction of delamination in a layer of solid elements at the ply interface. Accurate evaluation of interlaminar stresses can be critical for accurate prediction of delamination failure in multidirectional laminate composites. However, continuity of interlaminar stresses is difficult to enforce at the ply interface using regular  $C^0$  interpolated finite elements. A stress recovery procedure based on the work by Fagiano et al. [9] is proposed to improve the calculation of interlaminar stresses in the 3D solid FE models and validated using an axial extension benchmark problem.

Chapter 3 presents the model for progressive damage based on a continuum damage mechanics approach. Introduction of a solid element delamination layer at the interface between plies allows for the formulation of a fully three-dimensional continuum damage model applicable to prediction of interactions between interlaminar and intralaminar failures. An oriented mesh approach with crack band regularization [10] to alleviate mesh dependency issues typically found in continuum damage mechanics methods is proposed. The model is extended to simulation of progression of fatigue damage using a fatigue progression algorithm based on the combination of LaRC failure criteria and damage accumulation due to variable stress conditions under fatigue cycling. Predictions of progression of damage under monotonic and fatigue loading in Carbon/Epoxy open-hole tension and compression laminate coupons are presented with

subsequent correlation with test results. Post-failure sub-surface three-dimensional inspection based on X-Ray Computed Tomography (CT) provides unique insights for observation of damage mode interactions and validation of the virtual test methodology. Some of the work presented in this chapter has been published in Refs. [11-13].

In Chapter 4, the methodology for integration of porosity defects into FE models for assessment of their effects on strength and fatigue constitutive properties is provided. Carbon/Epoxy curved-beam test articles are used to validate the method. X-Ray CT measurements of porosity defects present in curved-beam specimens are integrated into FE-based stress analysis to capture the effects of defects on the InterLaminar Tensile Strength (ILTS) and ILT fatigue behavior. Once the effects of manufacturing defects are captured through transfer of the CT measurements into a three-dimensional FE model, their contribution to the scatter in the test data can be quantified, and reliable interlaminar material properties determined. The work presented in this section has been published in Refs.[14-16].

The scaling of the virtual test and methodology for integration of defects acquired at the material scale to larger structural elements is presented in Chapter 5. Two feet (60 cm) long thick laminates representative of structural components used in the rotorcraft industry are used for a feasibility assessment. The method includes advanced meshing techniques and integration of high-fidelity CT measurements of manufacturing defects representative of irregularities observed at the structural scale. Failure predictions and correlations with test results for Carbon/Epoxy articles are presented.

Conclusions and perspectives are stated in the final chapter.

### 1.3 Literature Survey

#### *1.3.1 Stress-based Failure Predictions in Composites*

The first step toward accurate failure predictions in composites is the development of reliable failure criteria. Significant research efforts have been conducted to utilize fracture mechanics principles for characterizing failures in composites. In particular, models based on fracture mechanics have been developed to predict delamination growth onset from a simulated initial delamination [18]. Acceptance of such techniques requires successful demonstration at the structural level. One concern is that defining component failure as the onset of delamination growth from initial delamination flaw might prove overly conservative. This is true because energy-absorbing mechanisms, other than delamination, may occur in structural components for a variety of reasons, such as branching of the initial delamination through matrix ply cracks into other interfaces in tape laminates. Accurate damage tolerance models must account for interaction of in-ply and interlaminar failure modes.

As opposed to the approach based on fracture mechanics, a large body of research work has been dedicated to the definition of stress-based failure criteria for composites. Stress-based failure criteria can be classified whether they are physically-based and consider separately different failure mechanisms, or are so-called generalized and typically combine failure modes in a polynomial approximations. Generalized failure criteria, including the popular Tsai-Wu quadratic failure criterion proposed in 1971 [17], continue to be widely used in the industry, as they are easy to use and typically require few standard ply material properties. If generalized failure criteria can offer valuable guidance to designers, their abilities to accurately predict failures in most aerospace

composite structures remain limited, as complex loadings, discrete failure events and failure mechanisms interactions are typically involved.

Hashin and Rotem [21] were the first to introduce a new generation of physically-based failure criteria for composites, where failure mechanisms are described separately. In [21], they proposed two separate criteria for fiber and matrix failure with a quadratic interaction assumed between the tractions acting on the fracture plane. In [23], Hashin proposed to distinguish tension and compression matrix failures and used a quadratic interaction between stress invariants, to overcome the difficulty in finding the fracture plane. Sun et al. [24] modified Hashin's criterion to account for the beneficial effect of transverse compression on the matrix shear strength. Puck [25] and Puck and Schürmann [26] incorporated elements of the Mohr and Coulomb theory [27] into Hashin's criterion to introduce the concept of the fracture plane and fracture angle, and formulated a comprehensive mechanics-based theory for fiber and matrix failure. Based on the ideas by Hashin, improvements by Sun and Puck, and fracture mechanics concepts from the Hahn and Johansson's proposal [28], Davila and Camanho [29] proposed the LaRC failure criteria as the most recent set of separate stress-based failure criteria for fiber and matrix failure mechanisms where no curve-fitting parameters are required. Latest improvements of the LaRC criteria were proposed by Pinho et al. in [30].

### *1.3.2 Progressive Damage*

The ability to predict damage progression to ultimate failure is useful for enabling less conservative failure predictions in laminated composite designs. Many efforts have been dedicated to the development of progressive damage models. Analytical or semi-analytical approaches have been developed to relate the applied load to the residual stiffness and strength of laminates [31]. However these methods are limited to situations



when the laminate is uniformly loaded and when matrix cracking is the main failure mechanism. The formalism of continuum damage mechanics, based on the pioneering work by Kachanov [35], allows considering propagation of multiple failure mechanisms under the most complex geometries, loadings and boundary conditions. Maimí et al. implemented a continuum damage model based on failure initiation using the LaRC failure criteria in shell elements for in-plane failures [36]. The approach allowed prediction of the onset and evolution of different failure mechanisms, but was limited to intralaminar failure. Camanho et al. [38] introduced cohesive elements placed at the interfaces between laminae for prediction of the initiation and growth of interlaminar failure, based on the Dugdale-Barenblatt cohesive zone approach [40]. Cohesive elements were formulated to overcome some of the difficulties associated with determination of the initial delamination size and location of the crack front in classic fracture mechanics-based formulations, such as the virtual crack closure technique [39]. Cohesive elements typically combine strength-based failure criteria to predict the onset of damage and fracture mechanics principles to simulate damage propagation.

To predict progression of both delamination and ply failures, efforts have been made to combine cohesive elements that simulate delamination, with continuum damage models for in-ply failure [42], and more recently with the regularized extended Finite Element Method (Rx-FEM) used for intralaminar failure [43]. Although these approaches can be successful in some configurations, they are based on two different kinematic representations for interlaminar and intralaminar failures. This incompatibility can prevent accurate capture of failure mode interactions. Ply elements with continuum damage strain-softening models typically soften without being able to correctly unload the adjacent cohesive elements, which could result in non-conservative predictions. To ensure consistent kinematic representation between the different failure mechanisms,

Wisnom and coworkers [44] used cohesive zone models for both intralaminar and interlaminar failure mechanisms. Although this approach has proven accurate to simulate the interaction between failure mechanisms, its major limitations are in the need to know in advance the planes of crack propagation or to add cohesive interfaces for all possible planes where fracture might occur, which can be extremely costly numerically. Maimí et al. [45] proposed a three-dimensional continuum damage model that considers activation of both intralaminar and interlaminar failures within the same solid finite element. The drawback of this approach is that delamination failure is not physically localized at the ply interface; therefore calculation of the out-of-plane stress components used for activation of interlaminar damage might not be accurate. Also, three-dimensional regularization of the strain-softening behavior of elements failing in both interlaminar and intralaminar modes is not straightforward and the solution might suffer from significant mesh dependency.

In this work, continuum damage models for both intralaminar and interlaminar failure mechanisms are implemented using a discrete delamination layer of solid elements at the ply interface. This allows for full three-dimensional interaction of failure mechanisms, while a mesh oriented approach and separate crack band regularizations can be used to alleviate mesh dependency issues.

### *1.3.3 Progressive Fatigue Failure*

The first application of stress-based failure criteria to fatigue failure analysis was proposed by Hashin and Rotem [21]. The method was based on adjusting material strengths according to  $S-N$  curves for constant amplitude loading. For variable amplitude loading, in addition to the Miner's Rule for linear damage accumulation [46], a number of

cumulative damage rules based on residual life approach were proposed specifically for composites, such as Broutman and Sahu [47], and Hashin and Rotem [21]. A review of analysis methods for variable amplitude fatigue loading is available in [48]. An alternative to residual life was a method introduced by the “wear-out” model [49] that used residual strength as measure of fatigue degradation of the material. A review of methods based on residual strength and their comparison with tests can be found in [50]. Hashin also demonstrated that methods based on residual life and residual strength are equivalent if Hashin–Rotem damage accumulation rule is used [51].

Another approach of estimating fatigue life under variable loading is based on measurements of residual stiffness. One of its first applications was the critical-element model by Reifsnider and Stinchcomb [52]. Shokrieh and Lessard [53] combined fatigue failure analysis based on residual stiffness with stress-based failure criteria based on residual strength measurements. Their approach required large number of tests to characterize fatigue behavior of a unidirectional material. Methods to decrease the number of tests were later proposed by Shokrieh and Taheri-Behrooz [54]. However, oftentimes residual stiffness shows significant drop only shortly before failure so that the prediction methodologies based on residual stiffness are highly dependent on the experimental qualification of rapidly decreasing stiffness. For low cycle fatigue in general, it has been shown [55] that failure is typically of a “sudden death” type so that the residual strength remains equal to static strength before reducing drastically at failure.

Finite element simulations of fatigue failure have been proposed extensively during the last decade. In addition to works by Shokrieh et al. [53], Tserpes et al. [56] used the Hashin’s fatigue failure prediction method at the element level combined with gradual and sudden stiffness degradation to simulate failure. Lian and Yao [57] have conducted extensive test program and FEA simulations based on stiffness degradation

and assumed proportional residual strength degradation to predict failure using quadratic stress-based criteria. Other examples of using progressive failure approach can be found in works by Basu et al. [58] that provided failure predictions in laminated panels using 2D FEA; and Hufner and Accorsi [59] that demonstrated FEA-based simulations for open-hole tensile tests of woven composites and experimental verification using digital image correlation.

In this work, the fatigue damage progression algorithm combines stress-based fatigue failure (based on  $S-N$  curves) and the three-dimensional continuum damage scheme for damage accumulation under variable stress conditions and interaction of intralaminar and interlaminar failure mechanisms.

#### *1.3.4 Effects of Manufacturing Defects*

The effects of inadequate design method and manufacturing process used to produce Carbon/Epoxy and Glass/Epoxy composite aircraft flight-critical components could manifest themselves as porosity/voids, and such defects impact the performance and the service life of these components [60]. The defects must be accurately measured, and the measurements must be converted into structural models to assess the effects of the defects on structural properties.

To date, significant numbers of studies have addressed the effects of voids on mechanical properties of composites. Matrix-dominated properties were shown to be strongly dependent on the presence of porosity/voids [63]. Reduction of interlaminar shear [62] and transverse [62] properties have been reported. Wisnom et al. [65] reported a reduction ranging between 8% and 31% of the interlaminar shear strength of glass/epoxy and carbon/epoxy unidirectional laminates, depending on the void size.

Hagstrand et al. [66] found that flexural modulus and strength decrease by about 1.5% for each 1% of voids up to a void content level of 14%.

Most of the existing studies on porosity analysis in composites have focused on attempts to relate the specimen strength to the void volume percentage. One approach used ultrasonic inspection for detecting voids and correlated the laminate strength to the void percentage by the Mar-Lin criterion modified for the void analysis [63]:

$$\sigma_f = H(\alpha)^{-m} \quad (1.1)$$

Where H is the laminate toughness,  $\alpha$  is the absorption coefficient (in db/mm), and m is the order of the stress singularity at the crack tip between the plies; H and m were found by curve fitting.

Good correlation was reported for the interlaminar flexural strength of Carbon/Epoxy fabric [63] and Carbon/Bismaleimide fabric laminates [64]. Other proposals included representation of the stiffness/strength reduction as a linear [65] or second-order polynomial [67] function of the void volume fraction. While all research works report decreasing strength for higher void volume content, quantitative results demonstrate a lot of scatter. It was suggested that this could result from the different manufacturing processes used to generate specimens with different void contents.

Huang and Talreja [68] attributed the scatter in using the Mar-Lin criterion to the strong influence of void geometry and locations on the failure loads. An approach based on the void geometry using micrograph images was proposed. In particular, this study attempted to correlate the dimensions of the void to the volume percentage of the voids obtained by ultrasonic inspection. A parametric study based on a finite element (FE) model was used to correlate the reduction of stiffness to the void geometry. It was shown that fiber modulus was only slightly affected by the void content and that out-of-plane

properties degrade more than in-plane properties with the increase in void content; effect of voids on strengths was not considered.

Published computational approaches include a model to evaluate mode I strain energy release rate with voids placed ahead of the crack tip [69] and a model using cohesive elements at ply layer interfaces that simulated voids as pre-delaminations [70]. To illustrate the effect of porosity on strength and failure, micrographs of failed specimens were used to demonstrate crack initiation at voids [64] and accurate detection of porosity shapes was advocated [71]. However, the 3D geometries and locations of all sub-surface defects in a specimen were neither obtained nor used in analysis by any of these methods. Recently, a detailed study of fatigue failure of Glass/Epoxy composite laminates by microfocus CT demonstrated good experimental correlation of void geometry and location data with fatigue performance while no such correlation was found for the total void content [72].

Interlaminar tensile strength (ILTS) and fatigue properties, which could be the weakest link of a laminated composite system, have been among the most difficult basic material properties to characterize. One of the major barriers to accurate determination of the ILT properties is their extreme sensitivity to manufacturing defects including porosity. Currently, the American Society for Testing and Materials (ASTM) uses the standard ASTM D 6415 [73] based on four-point bending curved-beam specimens for measuring the ILT strength. Jackson and Martin [74], who first studied the curved-beam test configuration to establish a method for assessing ILT strength, observed a drastic (up to a factor of four) curved-beam strength reduction in low-quality curved-beam specimens due to large (macroscopic) voids detected based on a cross-section cut using a diamond saw. However, they could not explain large scatter in the strength data observed in high

quality curved-beam specimens, due to lack of available three-dimensional nondestructive inspection (NDI) techniques with micro-focus ability at that time.

Recent advances in high-resolution non-destructive evaluation (NDE) methods such as 3D X-ray Computed Tomography (CT) lead to fundamental change in defect analysis methods by allowing high-fidelity detection of defects in composites and automatic transition of the defect information to structural analysis models. This work presents a methodology that includes accurate detection and measurements of the porosity present in curved-beam test specimens by X-ray Computed Tomography; and transfer of critical defect information into finite element analysis to determine interlaminar tensile properties for pristine (porosity free) material conditions. This work shows that microscopic defects present in high-quality curved-beam specimens (with extremely low porosity content) affect the ILT strength and cause large scatter in the curved-beam test data; and captures the effects of such defects on the ILT strength.

## Chapter 2

### Constitutive Model and Failure Criteria

#### 2.1 Governing Length Scale

The methodology presented in this work for prediction of matrix-dominated failures in composites is based on the Finite Element Method (FEM). A critical consideration in the definition of FE models for composite materials is the determination of the scale at which the material behavior will be modeled. Typically, three scales can be considered when modeling a laminated composite: the macroscopic or structural level, the meso-scale level or ply-scale level and the microscopic level, as illustrated in Figure 2-1.

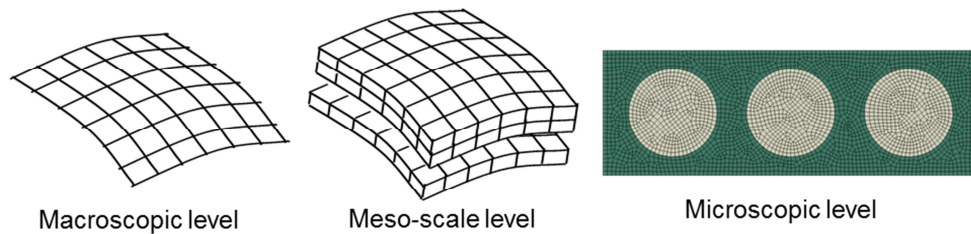


Figure 2-1 Three levels of FE representation of laminated composites

At the macroscopic level, the laminate is regarded as a thin shell structure where the orientations of the material layers are taken into account through an anisotropic elasticity model. The Classical Laminate Theory [75] is a typical representation of a composite laminate at the macroscopic level. The length scale is defined by the in-plane dimensions. In a FE model, the composite structure is typically represented as a laminated shell. Laminated shell models are very useful tools for the design at the



component level, as they require low computational resources. However models based on laminated plate theories are limited in the assessment of interlaminar stresses, which are critical to capture delamination failure. In addition, the in-plane length scale might not be appropriate for the integration of most manufacturing defects, such as fiber waviness or porosity voids, since their representative dimensions are typically several orders of magnitude smaller than in-plane dimensions.

The length scale below is the ply length scale and is the length scale considered in this work. The ply thickness is the governing length scale and plies are discretized and modeled separately as continua using orthotropic material properties. This scale is well adapted for discrete modeling of matrix crack failures, as matrix cracks typically develop within a single ply layer. Fiber failure is defined in a smeared manner over the ply thickness. The ply length scale is adequate for accurate determination of interlaminar stresses and therefore suitable for simulation of delamination failure. Three dimensional solid elements are used to represent the ply continuum (or a group of stacked plies with the same orientation). Since the aspect ratio of 3D finite elements is typically limited for accurate stress calculation, the modeling of a composite laminate system at such a scale level can lead to a considerable number of degrees of freedom that can quickly exceed computational capabilities. To overcome these difficulties, the sub-modeling technic is used to limit mesh refinements and accurate stress calculations to critical regions of interests.

The further level of length scale refinement for a composite material is when individual fibers are modeled and can be referred to as the micro-scale level. The fiber diameter is the governing length scale. Micro-scale models allow discrete modeling of fiber breakage and debonding. A micro-scale model alone has limited utility, as it is obvious that such a refinement would exceed the capacities of even the most powerful

computers. This is why these models are usually used in multiscale approaches, where different levels of observation are considered and connected. An example of multiscale approach is the use of a Representation Volume Element (RVE) [76] at the micro-scale to obtain ply-scale continuum material properties. The development of a unified multiscale model which could be used for failure predictions at the material and structural level using only micro-scale properties of fiber, resin and fiber/resin interface, is an extremely complex task which lies outside the scope of this work.

## 2.2 Constitutive Model

### 2.2.1 *Explicit Modelling*

A classical explicit approach based on generalized stress-strain relationships derived from the potential of the system is used to define the constitutive model of the composite materials used in this work. Explicit constitutive models are the most common approach, however it is worth noting that implicit and hybrid models (hybrid models combine explicit and implicit features) have also been used by researchers to simulate the response of composite structures. One example of implicit model includes the use of neuronal networks to define highly complex material behavior by extracting a mathematical relationship between the inputs and output of the system, with no attempt to represent any of the underlying physics [77]. If such a modeling approach can be successful, it is usually limited to specific material behavior within the range for which it was developed. The focus of this work is to present a methodology that could be extended to several geometries, layups and material systems using basic material properties obtained from unidirectional test articles. Therefore the use of implicit or hybrid models is not considered.

FEM analyses are performed using commercial FE code ABAQUS [78]. User subroutine UMAT is used to define non-linear material behavior, as well as to implement the failure model. The Python scripting capability provided by ABAQUS/CAE preprocessing software is used for parametric generation of complex FE mesh geometries and assignment of element properties and material orientation.

### *2.2.2 Material Constitutive Properties*

#### *2.2.2.1 Stress-strain Relations*

The constitutive models used in this work to simulate the response and failure of composite materials are developed in the context of continuum damage mechanics at the ply scale. Accurate ply material constitutive properties are essential for understanding the complex failure mechanisms of composite materials that show highly anisotropic properties. While the use of in-plane material properties is sometimes sufficient for failure predictions, critical applications such as composite helicopter rotor components may require full 3D material characterization to capture failure initiation. Thick glass-fiber and carbon-fiber reinforced epoxy-matrix tape composites frequently used in the design of helicopter rotor systems are considered in this work.

A recent methodology for material characterization based on full-field strain measurement techniques using the digital image correlation (DIC) technique and tests of unidirectional coupons has been developed by Makeev and coworkers [3]. Ply constitutive material properties for Carbon-IM7/Epoxy-8552 and Glass-S2/Epoxy-8552 listed in [3] are used in this work.

Non-linear shear stress-strain behavior is typically observed in polymer matrix composite materials [79]. Shear behavior in fiber-reinforced composites is matrix-

dominated and the non-linearity can be related to the formation of micro-cracks and viscoelastic behavior of the polymer matrix. Makeev et al. used a log-linear Ramberg-Osgood [80] relation to generalize the shear stress-strain data obtained from full-field deformation measurements in short beam shear tests [79] :

$$\begin{aligned}\gamma &= \frac{\tau}{G} + \left(\frac{\tau}{K}\right)^{\frac{1}{n}}, \tau \geq 0 \\ \gamma &= \frac{\tau}{G} - \left(\frac{|\tau|}{K}\right)^{\frac{1}{n}}, \tau < 0\end{aligned}\tag{2.1}$$

Where  $\gamma$  is the shear strain,  $\tau$  the shear stress, and the linear shear modulus  $G$ , the secant-intercept  $K$  and the exponent  $n$  are material constants determined from least-squares fit of test data.

Since unloading or hysteresis in shear response is not considered in this work, the constitutive model can be derived in the framework of elasticity. Elastic stress-strain relations for linear orthotropic material are modified to account for the shear non-linearity using relation (2.1) expressed in the three material planes. The constitutive stress-strain relations for an orthotropic composite material, including shear non-linearity, are expressed as:

$$\begin{aligned}\begin{bmatrix} \varepsilon_{11} \\ \varepsilon_{22} \\ \varepsilon_{33} \end{bmatrix} &= \begin{bmatrix} \frac{1}{E_{11}} & \text{Symmetric} \\ -\nu_{12} & \frac{1}{E_{22}} \\ -\nu_{13} & -\nu_{23} & \frac{1}{E_{33}} \end{bmatrix} \begin{bmatrix} \sigma_{11} \\ \sigma_{22} \\ \sigma_{33} \end{bmatrix} \\ \gamma_{12} &= \frac{\tau_{12}}{G_{12}} + \left(\frac{\tau_{12}}{K_{12}}\right)^{\frac{1}{n_{12}}} \\ \gamma_{13} &= \frac{\tau_{13}}{G_{13}} + \left(\frac{\tau_{13}}{K_{13}}\right)^{\frac{1}{n_{13}}}\end{aligned}\tag{2.2}$$

$$\gamma_{23} = \frac{\tau_{23}}{G_{23}} + \left( \frac{\tau_{23}}{K_{23}} \right)^{\frac{1}{n_{23}}}$$

Relations (2.2) can be used to derive the incremental expression of the Jacobian compliance matrix  $\frac{\partial \Delta \epsilon}{\partial \Delta \sigma}$  at the  $k^{\text{th}}$  increment during the non-linear FE analysis:

$$\begin{bmatrix} \frac{\partial \Delta \epsilon}{\partial \Delta \sigma} \end{bmatrix}^k = \begin{bmatrix} \frac{1}{E_{11}} & \frac{-\nu_{12}}{E_{11}} & \frac{-\nu_{13}}{E_{11}} & 0 & 0 & 0 \\ \frac{-\nu_{12}}{E_{11}} & \frac{1}{E_{22}} & \frac{-\nu_{23}}{E_{22}} & 0 & 0 & 0 \\ \frac{-\nu_{13}}{E_{11}} & \frac{-\nu_{23}}{E_{22}} & \frac{1}{E_{33}} & 0 & 0 & 0 \\ 0 & 0 & 0 & \frac{1}{G_{12}^*} & 0 & 0 \\ 0 & 0 & 0 & 0 & \frac{1}{G_{13}^*} & 0 \\ 0 & 0 & 0 & 0 & 0 & \frac{1}{G_{23}^*} \end{bmatrix}^k \quad (2.3)$$

In which,

$$\frac{1}{G_{ij}^*} = \frac{1}{G_{ij}} + \frac{1}{n_{ij}} \frac{1}{K_{ij}} \left( \frac{\tau_{ij}^k}{K_{ij}} \right)^{\frac{1}{n_{ij}}-1} \text{ with } ij = 12, 13 \text{ or } 23 \quad (2.4)$$

Where  $\tau_{ij}^k$  is the stress at the beginning of the  $k^{\text{th}}$  increment.

Since the Ramberg-Osgood relation defined by (2.1) is a continuous and non-singular function of  $\mathbf{R} \rightarrow \mathbf{R}$ , the Jacobian compliance matrix  $\frac{\partial \Delta \epsilon}{\partial \Delta \sigma}$  given in Eq. (2.3) can be inverted to obtain the Jacobian stiffness (or tangent stiffness) matrix  $\frac{\partial \Delta \sigma}{\partial \Delta \epsilon}$  at the  $k^{\text{th}}$  increment:

$$J = \frac{\partial \Delta \sigma}{\partial \Delta \epsilon} = \left[ \frac{\partial \Delta \epsilon}{\partial \Delta \sigma} \right]^{-1} \quad (2.5)$$

The analytical expression of the Jacobian stiffness matrix derived from Eq. (2.5) is implemented in the user subroutine UMAT to define the constitutive model in ABAQUS

FE models. The Jacobian  $J$  is also used to update the stresses in the subroutine UMAT at the end of the  $k^{\text{th}}$  increment using the following relation:

$$\sigma_{ij}^{k+1} = \sigma_{ij}^k + J^k \Delta \varepsilon_{ij}^k \quad (2.6)$$

Where  $\sigma_{ij}$  is the vector of stress components and  $\Delta \varepsilon_{ij}$  the vector of incremental strain components passed in by the FE code.

#### 2.2.2.2 Strength Properties

Accurate three-dimensional strength properties are also required for failure predictions using the failure criteria presented in section 2.3. Short beam shear results in [3] are used for the in-plane and interlaminar shear strengths of the IM7/8552 composite material considered in the simulations. Results in [16] are used for interlaminar tensile strength properties. The methodology for characterization of shear material properties was extended to fatigue loading by Makeev in [6] and the  $S-N$  curves provided in [6] are used in the fatigue simulations.

### 2.3 Failure Criteria

Physically-based failure criteria for prediction of the initiation of matrix dominated failures in composites are considered. This work uses the set of LaRC04 failure criteria proposed by Davila et al. in [29] for transverse tensile and compressive matrix failure and for fiber compression failure. The LaRC04 failure criteria for transverse matrix failure is modified and applied to delamination failure by introducing a thin layer of solid elements at the ply interface. Chapter 3 demonstrates that this approach enables to accurately capture the failure mode interactions typically observed in progressive failure of laminated composites.

### 2.3.1 Transverse Tensile Matrix Failure

Matrix transverse tensile failure, or matrix tensile cracking, for a ply subject to transverse tensile ( $\sigma_{22} > 0$ ) and in-plane shear stresses is assumed to occur in a fracture plane perpendicular to the loading direction, as illustrated in Figure 2-2. For references, 1 refers to the material fiber direction, 2 the transverse direction and 3 the thickness direction. Using microscopic assessment of the fracture surface under various types of loading, Hahn and Johannesson [28] proposed a mixed-mode toughness-based failure criterion to predict the initiation of matrix cracking:

$$(1 - g) \sqrt{\frac{G_I}{G_{Ic}}} + g \frac{G_I}{G_{Ic}} + \frac{G_{II}}{G_{IIc}} = 1 \quad (2.7)$$

Where  $G_{Ic}$  and  $G_{IIc}$  are the Mode I and Mode II fracture toughness values and  $g$  the fracture toughness ratio  $g = G_{Ic}/G_{IIc}$ .

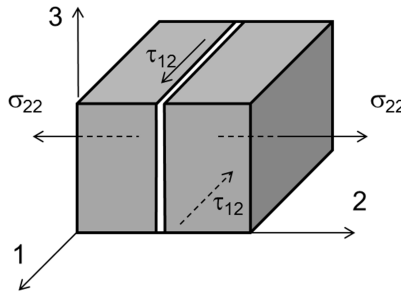


Figure 2-2 Schematic view of the fracture plane for transverse tensile matrix failure

Using fracture mechanics-based analysis for a slit crack in a ply, Davila et al. [29] showed that the Hahn criterion could be written using the transverse tensile  $\sigma_{22}$  and shear  $\tau_{12}$  stress components as:

$$(1 - g) \frac{\sigma_{22}}{S_{22}^T} + g \left( \frac{\sigma_{22}}{S_{22}^T} \right)^2 + \left( \frac{\tau_{12}}{S_{12}} \right)^2 \leq 1 \quad (2.8)$$

Where  $S_{22}^T$  and  $S_{12}$  are the transverse tensile and in-plane shear strengths, respectively.

For non-linear shear behavior, the last term in Eq. (2.8) must be modified. Using the approach by Sandhu [81] where the strain energy density is used for prediction of failure in materials exhibiting non-linear behavior, Camanho et al. [82] proposed the general form of the LaRC04 failure criterion for matrix cracking under transverse tension and in-plane shear:

$$(1 - g) \frac{\sigma_{22}}{S_{22}^T} + g \left( \frac{\sigma_{22}}{S_{22}^T} \right)^2 + \frac{\chi(\tau_{12})}{\chi(S_{12})} \leq 1, \quad \sigma_{22} \geq 0 \quad (2.9)$$

Where  $\chi(\tau_{12})$  is the strain energy density:

$$\chi(\tau_{12}) = \int_0^{\tau_{12}} \tau_{12} d\gamma_{12} \quad (2.10)$$

Using the Ramberg-Osgood relation given in (2.1) for composite material shear non-linearity, the analytical expression of  $\chi(\tau_{12})$  in Eq. (2.10) is given by:

$$\chi(\tau_{12}) = \frac{\tau_{12}^2}{2G_{12}} + \frac{K_{12}}{\frac{1}{n_{12}} + 1} \left( \frac{|\tau_{12}|}{K_{12}} \right)^{\frac{1}{n_{12}} + 1} \quad (2.11)$$



### 2.3.2 Transverse Compressive Matrix Failure

Matrix cracking under transverse compression ( $\sigma_{22} < 0$ ) and in-plane shear is assumed to occur in a fracture plane with a normal  $\mathbf{n}$  forming an angle  $\alpha$  with the transverse loading direction, as illustrated in Figure 2-3.

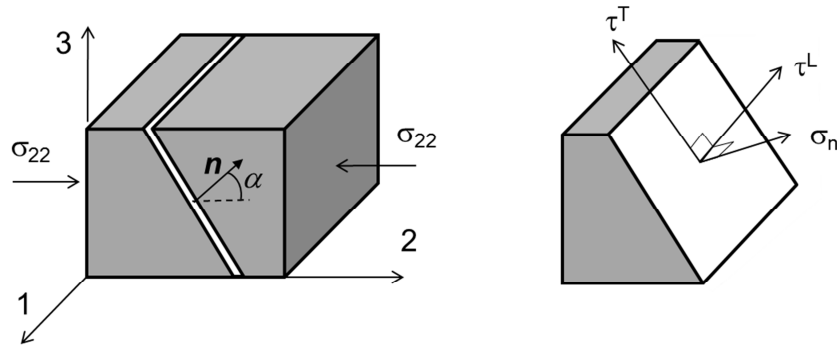


Figure 2-3 Schematic view of the fracture plane for transverse compressive matrix failure (left) and components of the stress tensor acting on the fracture plane (right)

The orientation of the fracture plane in a general loading situation depends on the combination of normal ( $\sigma_n$ ) and shear ( $\tau^T$  and  $\tau^L$ ) tractions, as shown in Figure 2-3. Using 3D transformation equations for an angle  $\alpha$  in the interval  $]-\pi, \pi]$  (where  $-\pi$  is not included), the tractions can be obtained from the components of the 3D stress tensor:

$$\begin{aligned}\sigma_n &= \frac{\sigma_{22} + \sigma_{33}}{2} + \frac{\sigma_{22} - \sigma_{33}}{2} \cos(2\alpha) + \tau_{23} \sin(2\alpha) \\ \tau^T &= -\frac{\sigma_{22} - \sigma_{33}}{2} \sin(2\alpha) + \tau_{23} \cos(2\alpha) \\ \tau^L &= \tau_{12} \cos(\alpha) + \tau_{31} \sin(\alpha)\end{aligned}\tag{2.12}$$

To establish the LaRC04 failure criteria for matrix cracking under compression, Davila et al. [29] considered the Mohr-Coulomb criterion in the case where  $\tau^L = 0$  which states that fracture occurs when the effective transverse shear stress  $\tau_{eff}^T = \tau^T + \eta^T \sigma_n$  is equal to the transverse shear strength  $S^T$ :

$$\tau_{eff}^T = |\tau^T| + \eta^T \sigma_n = S^T \quad (2.13)$$

Where  $\eta^T$  is the coefficient of transverse influence obtained for a fracture angle  $\alpha_0$  in pure transverse compression such as:

$$\tan(2\alpha_0) = -\frac{1}{\eta^T} \quad (2.14)$$

Puck [26] showed experimentally that  $\alpha_0 = 53^\circ$  for most unidirectional graphite-epoxy composites, such as the Carbon-IM7/Epoxy-8552 used in this work.

Using the Mc Cauley bracket  $\langle \cdot \rangle$  defined as:

$$\langle x \rangle = \begin{cases} 0 & x \leq 0 \\ x & x > 0 \end{cases} \quad (2.15)$$

The Mohr-Coulomb criterion in eq. (2.13) can be expressed as:

$$\frac{\langle \tau_{eff}^T \rangle}{S^T} = 1 \quad (2.16)$$

In a general case with  $\tau^L \neq 0$ , the effective shear stress must be defined in both tangential directions, by adding the contribution of the longitudinal effective stress  $\tau_{eff}^L$ :

$$\tau_{eff}^L = |\tau^L| + \eta^L \sigma_n \quad (2.17)$$

Where the coefficient of longitudinal influence  $\eta^T$  can be defined as [29]:

$$\eta^L = -\frac{S^L \cos(2\alpha_0)}{Y^C \cos^2(\alpha_0)} \quad (2.18)$$

With  $S^L$  and  $Y^C$  the longitudinal shear and transverse compressive strengths, respectively.

Based on the proposal by Puck and Schürmann [26] and the Mohr-Coulomb criterion in Eq. (2.16), Davila and al. [29] used a quadratic interaction between the effective shear stresses acting on the fracture plane to define the LaRC04 failure criterion for matrix compression:

$$\left(\frac{\langle \tau_{eff}^T \rangle}{S^T}\right)^2 + \left(\frac{\langle \tau_{eff}^L \rangle}{S^L}\right)^2 \leq 1, \quad \sigma_{22} < 0 \quad (2.19)$$

The fracture angle  $\alpha$  is determined numerically as the angle maximizing the failure criterion in (2.19). The 3D stress components in Eq. (2.12) are obtained from the FE analysis and the longitudinal and transverse shear strengths  $S^L$  and  $S^T$  defined along the fracture plane are equal to the transverse and interlaminar material shear strengths determined by SBS tests (see section 2.2.2.2), due to the assumption of transverse isotropy:  $S^L = S^T = S_{12} = S_{13}$ . Data from the prepreg manufacturer can be used for the transverse compressive strength  $Y^C = S_{22}^C$  in Eq. (2.18).

### 2.3.3 Fiber Compressive Failure

Failure criteria and models for fiber failure in compression are still the objects of on-going research and development. Most works consider that compressive fiber failure occurs as a result of shear kinking and damage in the matrix [30]. This failure mode is therefore largely affected by the resin behavior and might develop relatively early during the loading history. Failure criteria and damage propagation scheme for fiber compressive failure are required in this work to predict propagation of damage to a detectable sized in composite laminates loaded in compression, such as in the Open Hole Compression (OHC) test specimens considered in section 0.

Davila et al. in [29] assumed that kinking is the result of matrix shear failure, prompted by an initial misalignment of the fiber. Therefore, the criteria for matrix tension

failure given in Eq. (2.9) and matrix compression failure in Eq. (2.19) can be applied in the misalignment frame to predict fiber compressive failure, whether the transverse stress  $\sigma_{22}$  is positive or negative, respectively.

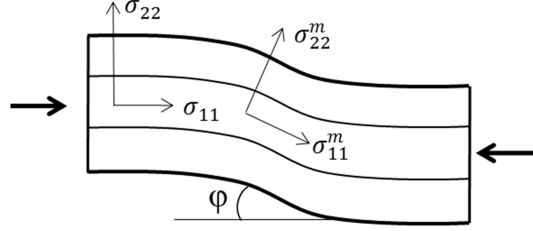


Figure 2-4 Fiber misalignment frame  $m$  for fiber kinking

The fiber misalignment is idealized as a local region of waviness, as show in Figure 2-4. In the misalignment coordinate system, the 2D ply stresses can be expressed as:

$$\begin{aligned}\sigma_{11}^m &= \cos^2(\varphi)\sigma_{11} + \sin^2(\varphi)\sigma_{22} + 2\sin(\varphi)\cos(\varphi)|\tau_{12}| \\ \sigma_{22}^m &= \sin^2(\varphi)\sigma_{11} + \cos^2(\varphi)\sigma_{22} - 2\sin(\varphi)\cos(\varphi)|\tau_{12}| \\ \tau_{12}^m &= -\sin(\varphi)\cos(\varphi)\sigma_{11} + \sin(\varphi)\cos(\varphi)\sigma_{22} + (\cos^2(\varphi) - \sin^2(\varphi))|\tau_{12}|\end{aligned}\quad (2.20)$$

For fiber compression with matrix tension, the stresses in the misalignment frame given by Eqs. (2.20) are substituted in Eq. (2.9):

$$(1 - g)\frac{\sigma_{22}^m}{S_{22}^T} + g\left(\frac{\sigma_{22}^m}{S_{22}^T}\right)^2 + \frac{\chi(\tau_{12}^m)}{\chi(S_{12})} \leq 1, \quad \sigma_{11} < 0 \text{ and } \sigma_{22}^m \geq 0 \quad (2.21)$$

For fiber compression with matrix compression, it is assumed that the failure is dominated by the shear stress  $\tau_{12}$  rather than the transverse stress  $\sigma_{22}$  [29]. The angle  $\alpha$  of the fracture plane is then equal to  $0^\circ$ , leading to  $\tau_{eff}^T = 0$ . Using this assumption, the matrix compression failure criterion in Eq. (2.19) becomes:

$$\left(\frac{\langle \tau_{eff}^L{}^m \rangle}{S^L}\right)^2 \leq 1, \sigma_{11} < 0 \text{ and } \sigma_{22}^m < 0 \quad (2.22)$$

Where:

$$\tau_{eff}^L{}^m = |\tau_{12}^m| + \eta^L \sigma_{22}^m \quad (2.23)$$

And  $S^L$  and  $\eta^L$  are defined as previously.

#### 2.3.4 Delamination

When introducing the LaRC04 failure criteria in [30], the authors suggest the use of cohesive elements to predict initiation and propagation of delamination failure. Cohesive elements can be combined with continuum damage models of solid ply elements to simulate both delamination and intralaminar ply failure. Although this approach has proved to be successful in some configurations [42], its application is limited if strong interaction occurs between transverse matrix cracking and delamination. This is due to the difference in kinematic representation between continuum damage and cohesive damage models. When transverse cracking occurs in a solid element including strain softening, the damaged element softens without being able to correctly unload the adjacent cohesive element at the interface. To accurately predict the interaction between interlaminar and intralaminar failure, a thin layer of solid elements is introduced at the interface of the ply, as illustrated in Figure 2-5. The solid elements used for delamination allows unloading of transverse cracks and include a continuum damage progression scheme presented in section 3.1 for propagation of delamination failure.

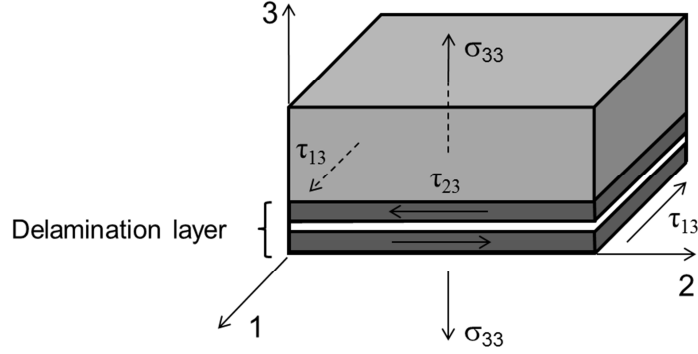


Figure 2-5 Schematic view of the fracture plane for delamination failure in the delamination layer

Delamination occurs by matrix failure at the interface under the effects of interlaminar tensile and shear stresses. Therefore, the LaRC04 failure criterion for matrix tensile failure can be applied for prediction of the onset of delamination. The delamination layer is in three-dimensional stress state and all three stress components acting on the fracture plane normal to material direction 3, as illustrated in Figure 2-5, must be accounted for. It also assumed that compressive out-of-plane normal stresses do not contribute to the failure of the interface. Eq. (2.9) for the initiation of delamination takes the following form:

$$(1 - g) \frac{\sigma_{33}}{S_{33}^T} + g \left( \frac{\sigma_{33}}{S_{33}^T} \right)^2 + \frac{\chi(\tau_{13})}{\chi(S_{13})} + \frac{\chi(\tau_{23})}{\chi(S_{23})} \leq 1, \quad \sigma_{33} > 0 \quad (2.24)$$

$$\frac{\chi(\tau_{13})}{\chi(S_{13})} + \frac{\chi(\tau_{23})}{\chi(S_{23})} \leq 1, \quad \sigma_{33} \leq 0$$

## 2.4 Recovery of Interlaminar Stresses

### 2.4.1 Stress Recovery Procedure

Accurate evaluation of interlaminar stresses at the ply interface might be critical in some situations to correctly capture initiation of delamination failures using the failure criteria introduced in Eq. (2.24). Three-dimensional FE models are usually required for acceptable accuracy of interlaminar stresses calculations. However, it is well known that continuity of interlaminar stresses in the FE analysis of laminates is difficult to enforce at the ply interface using regular  $C^0$  interpolated elements. In commercial FE codes, stress fields are usually retrieved at the nodes using extrapolation technics from stress results at integration points, which may lead to spurious stress oscillations when two different material orientations are assigned at the interface. Mesh refinements in order to increase the number of elements along the ply thickness could alleviate the problem, but this approach is oftentimes not adequate due to limitations of computational capacities.

A stress recovery procedure based on equilibrium considerations and calculation of interlaminar contact forces is considered to improve the accuracy of evaluation of interlaminar stresses at the ply interface in multilayered composite laminates. The procedure is based on the approach proposed by Fagiano et al. [9], where interlaminar stresses are recovered from calculation of interlaminar forces acting at the interface using equilibrium and compatibility considerations. The formulation is well suited for the FE representation of laminate composites at the ply length scale used in this work, with each ply modelled as a separate layer. Figure 2-6 shows a representation of a typical interface between ply (1) and ply (2).

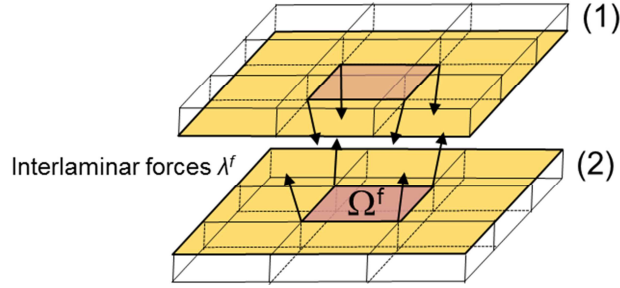


Figure 2-6 Interlaminar nodal forces at the interface between ply (1) and ply (2)

For an element at the ply interface, equilibrium and compatibility equations at the interfacial nodes can be written as a system of linear equations:

$$\begin{bmatrix} K^{(1)} & 0 & B^{(1)T} \\ 0 & K^{(2)} & B^{(2)T} \\ B^{(1)} & B^{(2)} & 0 \end{bmatrix} \begin{bmatrix} u^{(1)} \\ u^{(2)} \\ \lambda^f \end{bmatrix} = \begin{bmatrix} f^{(1)} \\ f^{(2)} \\ 0 \end{bmatrix} \quad (2.25)$$

Where  $K^{(1)}$  and  $K^{(2)}$  are the stiffness matrices of the two adjacent plies,  $u^{(1)}$  and  $u^{(2)}$  the nodal displacement vectors,  $f^{(1)}$  and  $f^{(2)}$  the nodal load vectors,  $B^{(1)}$  and  $B^{(2)}$  Boolean matrices used to ensure equality of the displacements and  $\lambda^f$  are Lagrange multipliers representing interlaminar forces introduced to enforce the compatibility constraints between the plies.

The system of equations in (2.25) is solved for the nodal displacements  $u^{(1)}$  and  $u^{(2)}$  and for the interlaminar forces  $\lambda^f$ . The nodal traction vector  $t^f$  is obtained using the matrix of element areas  $M^f$ :

$$M^f t^f = \lambda^f \quad (2.26)$$

With  $M^f$  the matrix of element area defined as:

$$M^f = \int_{\Omega_f} N^T N d\Omega_f \quad (2.27)$$



$N$  is the matrix of  $C^0$  interpolation shape functions and  $\Omega^f$  the surface of the element at the interface, as illustrated in Figure 2-1.

Normal and shear interlaminar stress components  $\sigma_{33}$ ,  $\tau_{13}$  and  $\tau_{23}$  at each interfacial node are obtained by projection of the traction vector into the material coordinate frame.

Similar to the work by Fagiano et al. in [83], the stress recovery approach is implemented in ABAQUS FE models using tied contact interactions at the ply interface to enforce compatibility between the layers and retrieve interlaminar nodal forces and stresses. The tied contact formulation in ABAQUS uses Lagrange multipliers to constraint the translational degrees of freedom of the master and slave surface forming the contact pair for the duration of the simulation [78]. A surface-to-surface contact formulation is used for improved accuracy.

Post-processing of interlaminar nodal forces and stresses can be easily carried out using Python scripting interface with ABAQUS/CAE and generate node-based contour plots of interlaminar stresses and failure index for delamination. Interlaminar nodal forces and stresses can also be written at the end of each increment in the ABAQUS results file (.fil) and accessed during the analysis in the user subroutine UMAT by using the utility subroutine DBFILE. This enables to implement the stress recovery procedure for propagation of delamination failure, by using the interlaminar recovered stresses in the LaRC04 failure criterion to activate damage in the delamination layer elements. Detailed description of the failure model for damage progression is provided in Chapter 4.

### 2.4.2 Benchmark Validation

The stress-recovery procedure is validated using the uniform axial extension benchmark problem analyzed by Pipes and Pagano in [84]. Pipes and Pagano considered a symmetric  $[+45/-45]_s$  4-ply graphite-epoxy laminate under axial loading, as illustrated in Figure 2-7. They provided numerical results for the three-dimensional stress distribution at the  $+45/-45$  ply interface using a finite difference numerical method to solve the differential equations of the exact elasticity problem. Makeev and Armanios [85] also proposed an iterative method to obtain a weak form solution of the stress field for the same axial extension laminate. The cross-ply symmetric axial extension laminate is a classic illustration of the singular interlaminar stress field that can arise at the free-edge in multi-directional laminates.

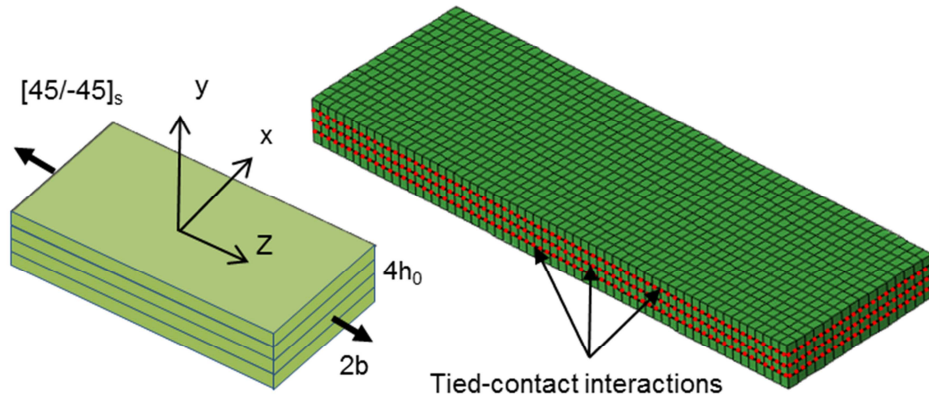


Figure 2-7 Geometry (left) and FE model (right) for the  $[+45/-45]_s$  axial extension laminate benchmark problem

The stress-recovery is implemented in an ABAQUS FE model of the  $[+45/-45]_s$  laminate with one solid element per ply and tied-contact surface-to-surface interactions

assigned at the three ply interfaces, as illustrated in Figure 2-7. A 10% ply-thickness thin delamination layer of solid elements is also defined at the interface, as illustrated in Figure 2-5. The FE model includes linear 8-noded hexagonal 3D elements with reduced integration scheme (C3D8R) from the ABAQUS element library. Linear elastic orthotropic material properties for a typical graphite-epoxy composite material with  $E_{11} = 20$  ksi (138 MPa),  $E_{22} = E_{33} = 2.1$  ksi (14 MPa),  $G_{12} = G_{13} = G_{23} = 0.85$  ksi (6 MPa),  $\nu_{12} = \nu_{13} = \nu_{23} = 0.21$  are assigned to the FE model, as listed in [84]. The dimensions are such as  $b = 8h_0$ , with  $h_0$  the ply thickness and  $b$  the half width of the laminate.

Distribution of interlaminar stresses  $\sigma_{yy}$  and  $\sigma_{xy}$  along the normalized half width  $x/b$  at the 45/-45 ply interface for  $z = h_0$  are presented in Figure 2-8 and Figure 2-9, respectively. Stress results from the recovery procedure are compared with data from Pipes and Pagano in [84] and the two-term approximation proposed by Makeev in [85]. Results are presented for three different mesh discretization along the half width of the laminate, with 8, 16 and 32 elements considered. Interlaminar stresses obtained from  $C^0$  nodal interpolation of stresses calculated at element integrations points in the delamination layer are also presented, for the smallest mesh discretization.

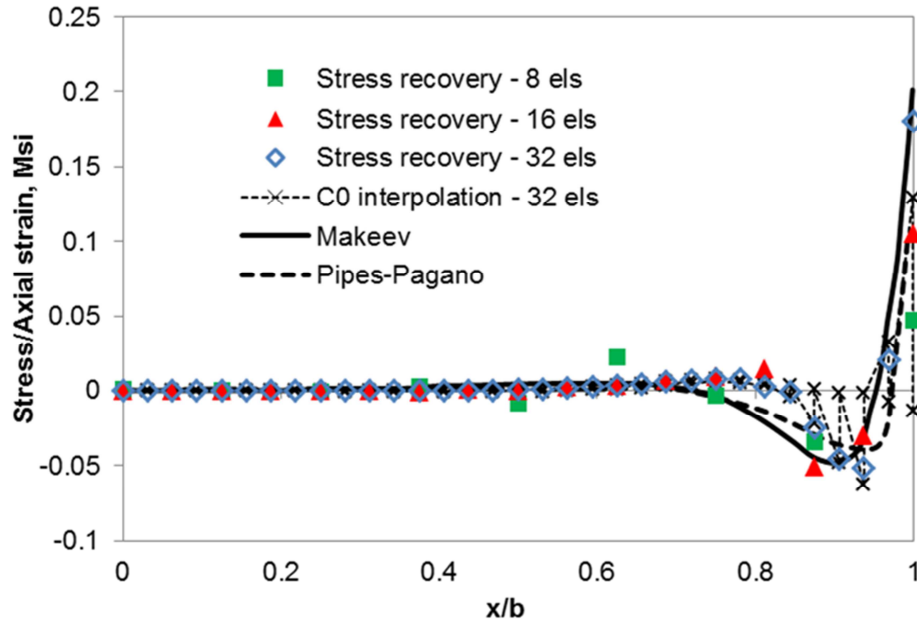


Figure 2-8 Comparison of normal interlaminar stress  $\sigma_{yy}$  at +45/-45 interface for axial extension of  $[+45/-45]_S$  laminate

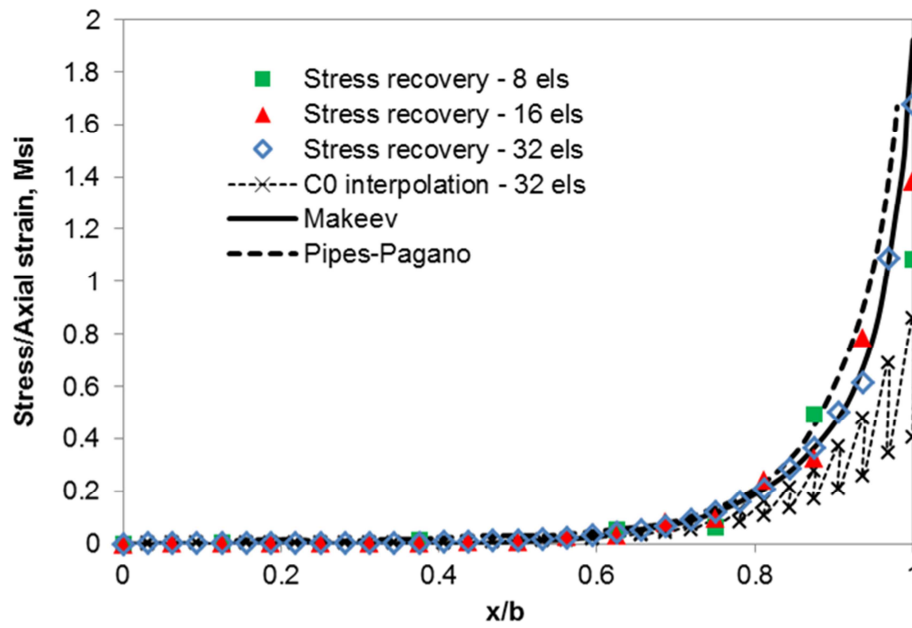


Figure 2-9 Comparison of shear interlaminar stress  $\sigma_{xy}$  at +45/-45 interface for axial extension of  $[+45/-45]_S$  laminate

Results from the stress recovery procedure compare well with the predictions by Pipes and Pagano [84] and Makeev [85] for both interlaminar normal and shear stress. The recovery procedure is able to capture the strong singularity at the free edge and rapid convergence is demonstrated. It is worth noting that stress distributions obtained using  $C^0$  interpolation of solid element stress results at integration points exhibit typical oscillatory behavior and do not capture correctly the high stress gradients at the free-edge, which could lead to inaccurate predictions of delamination failures in laminates.

## Chapter 3

### Progressive Failure

Defining composite failure as the onset of delamination growth might prove overly conservative due to branching of the initial delamination through matrix ply-cracks into other interfaces that typically occurs in multi-directional tape laminates. Prediction of damage progression to significant (detectable) size that accounts for the interaction of in-ply and interlaminar matrix-dominated failure modes is necessary for accurate assessment of composite part condition.

This Chapter presents the implementation of a damage progression procedure for the matrix-dominated failure modes identified in Chapter 3 in the definition of the failure initiation criteria. The progressive damage model for quasi-static failure is extended to fatigue loading by combination with fatigue damage accumulation rules. Initial damage and a predefined path for damage progression are not required. Failure predictions and subsequent test correlations are presented for static and fatigue of Open-Hole Tension (OHT) and Open-Hole Compression (OHC) standardized coupon tests. FE simulations for propagation of surface cracks are compared to post-failure surface inspections and to cracks detected from Digital Image Correlation (DIC) surface strains measurements. Three-dimensional volumetric visualization by X-ray Computed Tomography (CT) is used to inspect damage in tested specimens and correlate with simulation results.

### 3.1 Failure Damage Progression

This work uses a continuum damage model based on the approach originally proposed by Kachanov [35] where an internal scalar damage variable is used to characterize the local loss of load-carrying capacity in the material, once a failure criterion is met. One of the simplest ways to characterize damage in an isotropic material is to introduce a single damage variable  $d$  to define the damage state by the variation in elastic modulus  $E$ , as proposed by Lemaitre and Chaboche [86]:

$$E(d) = (1 - d)E \quad (3.1)$$

Where  $d_s$  varies from 0 to 1 for an undamaged to a fully damaged state.

To apply continuum damage models to composite materials, the orthotropic and inhomogeneous nature has to be taken into consideration. Damage in composites can occur in various levels of scale and with preferred directions for crack growth. It is therefore essential to identify the failure mechanisms for damage propagation, as well as the scale at which the material is considered homogeneous for application of the continuum damage model. As presented in section 2.1, the ply length scale is used as the governing length in this work, and the composite plies are homogenized separately as continua. The continuum damage model is defined for the matrix-dominated failure modes presented in section 2.3.

The loss of stiffness due to damage is assumed to occur in the plane of cracking, once the failure criterion associated to the failure mode is met. Following this assumption and using Eq. (3.1), the stress-strain relations for matrix tensile cracking and delamination failure for a solid FE element including damage and shear non-linearity take the following forms:

- *Matrix tensile cracking:*

Matrix tensile cracking occurs in the (1-3) material plane, as presented in section 2.3.1. Damage variable  $d_m$  is introduced to define the loss of stiffness in the transverse material direction (2) as well as shear stiffness loss in the (1-2) and (2-3) planes.

$$\begin{bmatrix} \epsilon_{11} \\ \epsilon_{22} \\ \epsilon_{33} \end{bmatrix} = \begin{bmatrix} \frac{1}{E_{11}} & \text{Symmetric} \\ -\nu_{12} & \frac{1}{(1-d_m)E_{22}} \\ -\nu_{13} & \frac{-\nu_{23}}{E_{22}} & \frac{1}{E_{33}} \end{bmatrix} \begin{bmatrix} \sigma_{11} \\ \sigma_{22} \\ \sigma_{33} \end{bmatrix}$$

$$\gamma_{12} = \frac{\tau_{12}}{(1-d_m)G_{12}} + \left( \frac{\tau_{12}}{(1-d_m)K_{12}} \right)^{\frac{1}{n_{12}}} \quad (3.2)$$

$$\gamma_{13} = \frac{\tau_{13}}{G_{13}} + \left( \frac{\tau_{13}}{K_{13}} \right)^{\frac{1}{n_{13}}}$$

$$\gamma_{23} = \frac{\tau_{23}}{(1-d_m)G_{23}} + \left( \frac{\tau_{23}}{(1-d_m)K_{23}} \right)^{\frac{1}{n_{23}}}$$

- *Delamination:*

Delamination cracks propagate in the (1-2) material plane and damage variable  $d_d$  is introduced to define the loss of stiffness in the transverse material direction (3) as well as shear stiffness loss in the (1-3) and (2-3) planes.

$$\begin{bmatrix} \epsilon_{11} \\ \epsilon_{22} \\ \epsilon_{33} \end{bmatrix} = \begin{bmatrix} \frac{1}{E_{11}} & \text{Symmetric} \\ -\nu_{12} & \frac{1}{E_{22}} \\ -\nu_{13} & \frac{-\nu_{23}}{E_{22}} & \frac{1}{(1-d_d)E_{33}} \end{bmatrix} \begin{bmatrix} \sigma_{11} \\ \sigma_{22} \\ \sigma_{33} \end{bmatrix} \quad (3.3)$$

$$\gamma_{12} = \frac{\tau_{12}}{G_{12}} + \left( \frac{\tau_{12}}{K_{12}} \right)^{\frac{1}{n_{12}}}$$



$$\gamma_{13} = \frac{\tau_{13}}{(1 - d_d)G_{13}} + \left( \frac{\tau_{13}}{(1 - d_d)K_{13}} \right)^{\frac{1}{n_{13}}}$$

$$\gamma_{23} = \frac{\tau_{23}}{(1 - d_d)G_{23}} + \left( \frac{\tau_{23}}{(1 - d_d)K_{23}} \right)^{\frac{1}{n_{23}}}$$

The damage variables  $d_m$  and  $d_d$ , respectively for matrix tensile cracking and delamination, are activated by the LaRC04 stress-based and fracture-based criteria defined for the appropriate plane of failure. The damage model assumes that the crack is “smeared” over the volume of an element. This concept is known as the “crack band model” introduced by Bazant and Planas [10]. The smeared crack band model is intended to capture the behavior of a region where numerous microcracks have initiated, also called the process zone, and coalesce to form a larger crack. The crack band model, originally developed by Bazant for failure in concrete material, has been successfully applied to failures in composites [37]. Fiber-reinforced composites are known to develop micro-damage in the matrix or at the fiber/matrix interface long before the apparition of visible cracks [26]; this could be considered as the basis for application of the crack band model to composite failure.

A number of damage evolution laws have been proposed to simulate both the material response to micro- and macro-cracking. In this work, it is assumed that the damages variables go from zero to one as fast as practically possible to allow for convergence of the numerical procedure. This technic is similar to the sudden stiffness degradation approach used in [56]. The degradation evolution law for damage variable  $d$  is expressed as:

$$d(t) = \begin{cases} 0, & t < t_f \\ (1 - k_f) \frac{t - t_f}{\Delta t_r}, & t_f \leq t \leq t_f + \Delta t_r \\ 1 - k_f, & t > t_f + \Delta t_r \end{cases} \quad (3.4)$$

Where  $t$  represents the step time parameter defined in a FE analysis using ABAQUS Standard.  $t_f$  corresponds to the time parameter at which the element fails, which is given by the step time at which the failure criteria is met in a static analysis;  $\Delta t_r$  is the time of damage relaxation determined from convergence requirements; and  $k_f$  is the remaining stiffness ratio that is small enough to simulate full element failure. The time variable is proportional to the applied load in quasi-static analysis and to the number of loading cycles in fatigue analysis. A damage relaxation time  $\Delta t_r$  of 5% of the total time step and a residual stiffness ratio  $k_f$  of  $10^{-6}$  were typically used.

The damage model is implemented in ABAQUS FE models by use of the user subroutine UMAT [78], which also includes the definition of the non-linear shear stress-strain relations, as discussed in section 2.2.2.1. The subroutine UMAT is called for each element integration point at each iteration of every increment of the non-linear analysis. The UMAT subroutine requires definition of the incremental material Jacobian matrix of the constitutive model,  $\partial \Delta \sigma / \partial \Delta \epsilon$ , and update of stresses and solution-dependent state variables at the end of the increment.

The Jacobian matrix for the damage model can be derived using the strain-stress relation given by Eqs. (3.2) and (3.3), similar to the procedure presented in section 2.2.2.1. The Jacobian matrix for the damage model is computed by replacing the undamaged material stiffness  $E_{ij}$ ,  $G_{ij}$  and  $K_{ij}$  by their expressions including damage,  $(1-d)E_{ij}$ ,  $(1-d)G_{ij}$  and  $(1-d)K_{ij}$ , respectively. Due to non-linearity in shear stress-strain relations, values of the shear stress components are required to compute the terms  $J_{44}$ ,  $J_{55}$  and  $J_{66}$  in the Jacobian matrix. The value of the stress tensor from the previous

increment that is passed in at the beginning of the increment in the subroutine UMAT is used to compute the Jacobian matrix. For each failure mode, the value of the damage variable  $d$  is assigned to a state variable STATEV, which is passed in at the beginning of the increment and updated at the end of the increment using Eq. (3.4).

The step time  $t$  in Eq. (3.4) is available through variable TIME(1) [78], which is passed in for information by the solver at the beginning of the increment. The time  $t_f$  for damage initiation is computed through a state variable that stores the step time value TIME(1) of the increment for which the failure initiation criterion reaches one, for the corresponding failure mode. Stresses are updated at the end of the increment using stresses at the beginning of the increment, the Jacobian matrix and the strain increments, according to Eq. (2.6). Once the stresses are updated, the failure criteria are computed and stored in state variables. The state variable corresponding to the failure initiation criteria and the damage index can be output to the ABAQUS output database, in order to visualize the initiation and propagation of failure.

### 3.2 Mesh Dependency

Numerical methods that simulate damage by strain-softening are known to produce mesh-dependent results. The continuum damage approach considered in this work implicitly assumes variation of deformation in a smooth manner, since the model is expressed in terms of averaged material constitutive properties at the ply level. When damage occurs and stiffness properties of damaged elements are degraded, the model increasingly displays localization and the simulation becomes affected by the mesh size and mesh alignment, which could lead to non-physical failure predictions.

The dependency on mesh alignment is illustrated for the propagation of matrix cracks in a  $[45/0/-45/90]_{2S}$  OHT laminate coupons. The specimen is loaded in tension in the longitudinal direction (fiber direction for the zero degree plies). The first failure events are matrix cracks that initiate at stress concentrations around the hole in the 90 degree plies. Figure 3-1 presents the contour plot of the matrix failure damage index for the propagation of cracks in the first surface 90 degree plies, using a FE mesh with elements oriented radially around the hole. Submodeling is used to simplify the mesh generation and allow sufficient mesh refinements around the hole for stress convergence. A global model with coarser mesh is used to define displacement boundary conditions at the external circumferential surface of the submodel, as illustrated in Figure 3-1.

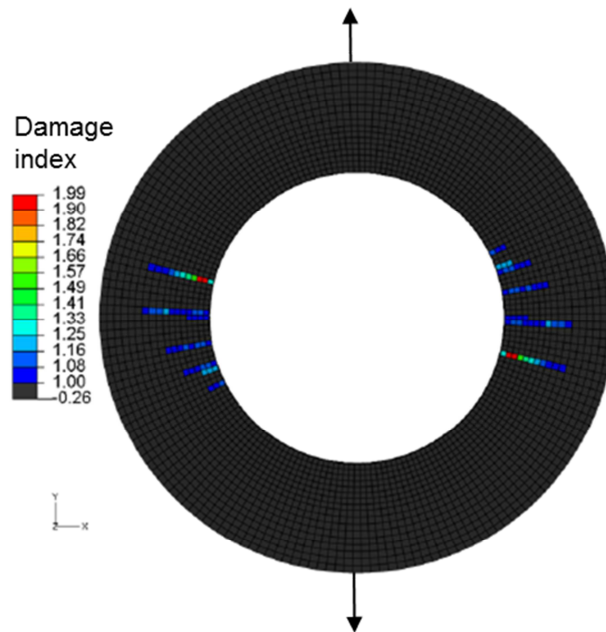


Figure 3-1 Propagation of matrix cracks in a radially oriented submodel mesh for 90 degree surface ply in a  $[45/0/-45/90]_{2S}$  OHT coupon

Figure 3-1 shows that matrix cracks propagate along the radial direction, accordingly to the alignment of the elements. Physical matrix cracks are always supposed to occur along the fiber direction, i.e. perpendicular to the loading axis for the 90 degree plies, which is in contradiction with the FE simulation. The same observation can be done for the first developments of matrix cracks in 45 degree plies.

To address the dependency on mesh alignment, a fiber-aligned mesh approach is introduced. In this approach the FE mesh for each ply is structured such that the element edges are parallel to the fiber directions. Python scripting capability integrated to ABAQUS/CAE for pre-processing of ABAQUS FE models is used to generate the fiber-aligned mesh. The procedure starts with a structured mesh of a rectangular surface from which elements are deleted, merged and reshaped in order to fit the exact geometric boundaries of the sub-model. Details on the procedure to generate fiber oriented meshes are presented in Appendix B. Since the ply meshes are incompatible at their interfaces, surface-based mesh tie constraints are used to hold the mesh assembly together. Figure 3-3 in section 3.4.1 shows a typical global mesh and fiber-oriented mesh with mesh tie constraints for an open hole coupon.

Developments of matrix cracks in the fiber-oriented mesh for the OHT problem are illustrated in Figure 3-2 in 90 degree and 45 degree plies. It is shown that cracks develop along the fiber direction, as expected experimentally due to the weaker properties of the matrix. Correct simulation of the direction of propagation of matrix crack is necessary to capture the interactions with delamination and redistribution of stresses that lead to final failure. Subsequent test correlations for crack sizes, crack locations and failure loads using the fiber-aligned approach are presented in section 3.4 and section 0 for static and fatigue failure of OHT and OHC coupons.

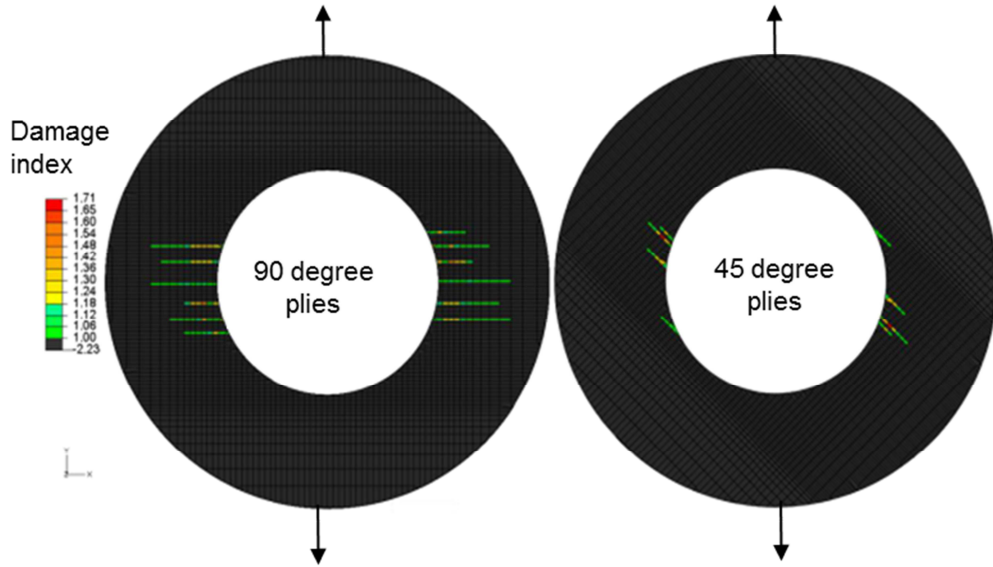


Figure 3-2 Propagation of matrix cracks in a fiber-oriented submodel mesh for 90 degree and 45 degree plies in OHT coupon

Damage simulation methods with material softening are also known to introduce dependence on the element mesh size, due to strain-localization. Strain-localization is the result of loss of positive-definiteness of the tangent stiffness tensor in the post-peak softening region [87]. Due to strain localization, the strain energy required to fail an element becomes proportional to the size of the element. In the limit as the element size is decreased, zero energy is required to fail the element.

Bazant [10] showed that the fracture energy  $G$  in the crack band model, defined as the energy consumed in the formation and opening of microcracks per unit area, could be related to the effective width  $w_c$  of the crack band measured in the direction perpendicular to the direction of crack propagation:

$$G = w_c \int \sigma d\varepsilon \quad (3.5)$$

In a numerical FE model with the fracture plane parallel to the mesh lines, such as in the fiber-oriented mesh used in this work, the effective width corresponds to the element size perpendicular to the crack path. The objectivity of the FE numerical models used in this work is ensured by selection of mesh size parameters that allow for the best agreement with test results for measurements of surface crack length.

### 3.3 Fatigue Damage Progression Algorithm

The damage model is extended to predictions of damage progression under fatigue loading. The fatigue damage progression algorithm is based on the combination of strength-based LaRC failure initiation criteria and damage accumulation due to variable stress conditions under fatigue cycling. At any cycle, a fatigue failure criterion can be defined by assuming that the material strengths follow the material  $S$ - $N$  curves:

$$S_{ij}^f = S_{ij}^{static} a_{ij} (\log N)^{-b_{ij}} \quad (3.6)$$

Where  $S_{ij}^f$  is the fatigue strength,  $S_{ij}^{static}$  the static strength,  $N$  the number of cycles and  $a_{ij}$  and  $b_{ij}$  are fitting parameters determined experimentally.

The fatigue failure criteria are obtained by substitution of Eqs. (3.6) in the LaRC failure criteria, and can be expressed as a function  $F$  of the stresses  $\sigma$  and the number of cycles  $N$ :

$$F(\sigma, N) = 1 \quad (3.7)$$

The fatigue failure criterion is assumed to provide prediction of the number of cycles to failure for an undamaged element under fixed peak stress. The Miner's rule [46] for linear damage accumulation is used to include effect of cyclic loading history on the

load-carrying capacity of the elements. It is worth noting that any other damage accumulation rule based on the number of cycles to failure could be used.

The fatigue progression algorithm can be summarized in the following steps:

1. The fatigue peak load is applied first and a static FE analysis is ran to obtain element stresses at zero cycle
2. At iteration k, Eq. (3.7) is solved to obtain the number of cycle to failure  $N_{el}^f$  for each undamaged elements:

$$F(\sigma_{el}^{(k)}, N_{el}^f) = 1 \quad (3.8)$$

3. For each element, the progressive failure cycle  $N_{el}^{pf(k)}$  is found based on the fatigue damage from the previous step:

$$N_{el}^{pf(k)} = (1 - d_{el}^{(k-1)})N_{el}^f \quad (3.9)$$

The damage at zero cycle is assumed to be equal to zero for all the elements

4. Find the element with the minimum progressive cycle to failure  $N_{el}^{pf(k)}$ , noted  $N^{(k)}$ , for the first element failure.
5. Advance cycle counter by  $N^{(k)}$
6. For each non-failed element calculate the new fatigue damage state by accumulation of damage due to the  $N^{(k)}$  cycles, using Miner's rule:

$$d_{el}^{(k)} = d_{el}^{(k-1)} + \frac{N^{(k)}}{N_{el}^f} \quad (3.10)$$

7. Fail the element with minimum progressive cycle to failure  $N^{(k)}$ , according to the damage model presented in section 1.3.2 and recalculate the stresses  $\sigma^{(k+1)}$  under the fatigue peak load. The stresses are redistributed due to element failure.



8. Re-iterate the procedure from step 2 until a detectable damage size is reached or an ultimate failure criterion is satisfied.

The fatigue progression algorithm is implemented in user subroutine UMAT. To speed up the fatigue calculation, multiple elements can be failed at step 7 during a single iteration. In this scenario, elements are sorted at step 4 by their progressive cycles to failure  $N_{el}^{pf(k)}$ . Instead of failing only the element with the minimum cycles to failure, a desired number of elements with the lowest cycles to failure are failed, and the cycle counter at step 5 is therefore advanced to the highest number of cycles to failure among this group of elements. Also, to avoid numerical overflow, a threshold selection based on element stresses is performed at the beginning of each iteration, to limit the search to regions more likely to fail first. Only elements with stresses higher than 15% of respective fatigue strengths (given by Eqs. (3.6)) are considered in the search.

It is worth noting that Eq. (3.8) in step 2 is a non-linear algebraic equation, therefore a numerical procedure is required to solve for the number of cycles to failure. The iterative Newton-Raphson method was used. Details on the procedure, including derivation of the analytical expression of the derivative function, are provided in Appendix A for matrix tensile cracking. As shown in Appendix A, the derivative is always positive for a number of cycles  $N > 1$ , therefore the algebraic Eq. (3.8) has only one single root.

### 3.4 Failure Predictions for Open-hole Tension Specimens

Simulation results and subsequent test correlations for static and fatigue failure of 16-ply IM7/8552 Carbon/Epoxy open-hole tensile laminates are presented. The OHT specimens were manufactured per ASTM standard D 5766 specifications [89]. The

coupon dimensions were  $1.5 \times 7.5 \times 0.104$  in. ( $38.1 \times 190.5 \times 2.642$  mm) with a 0.25 in. 6.35 mm (6.35 mm) hole diameter.

### 3.4.1 FE Model

A three-dimensional solid FE model of the OHT coupon was built. The OHT FE model includes a global model and a sub-model used to model the circumferential area around the hole with appropriate mesh refinements for stress convergence. Figure 3-3 shows the 3D global and sub-model FE mesh for the OHT coupon. The sub-model is an assembly of circular fiber-oriented structured meshes for each plies layers connected by surface-based mesh tie constraints. Details on the scripting procedure used to generate a circular oriented mesh are presented in Appendix B.

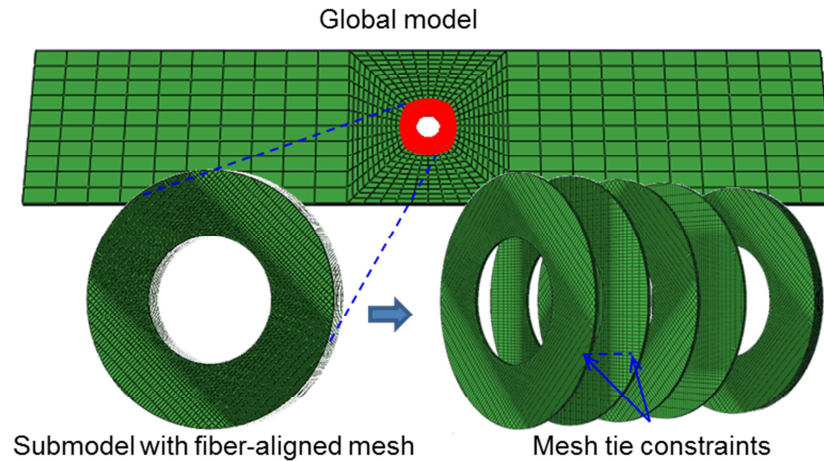


Figure 3-3 Global and local fiber-aligned oriented FE mesh for Open Hole coupon

Half of the coupon in the thickness direction (8 plies) was considered in the analysis due to symmetry of the layup and to reduce the computational effort. Symmetry

boundary conditions were applied at the half-thickness plane. Boundary conditions also included fixed displacements at the bottom end, and fixed transverse displacements and uniform axial (vertical) displacements with applied tensile force at the top end. The finite element model used 8-noded three-dimensional linear elements with reduced integration (C3D8R elements in ABAQUS) [25]. Each element had a single integration point so that the damage is activated for the whole element.

Displacements from the global model were applied as boundary conditions for the local model. Appropriate numbers of elements in the thickness and in-plane directions were determined by a stress convergence study. The smallest finite element size in the global mesh was 0.01 in. (0.25 mm) resulting in about 33,000 DOF. The outer radius for the sub-model was equal to 0.75 in. (19.05 mm), i.e. three times the hole radius and the smallest element size of  $4.9 \times 10^{-3}$  in. (0.124 mm). The sub-model used 5 elements per ply, including the layer of elements used for representation of delamination damage, as discussed in section 2.3.4. The size of the delamination element layer was selected as 10% of the ply thickness, based on calibration with test results. Figure 3-4 shows the fiber-oriented sub-model and the mesh discretization in the thickness direction for each ply layers.

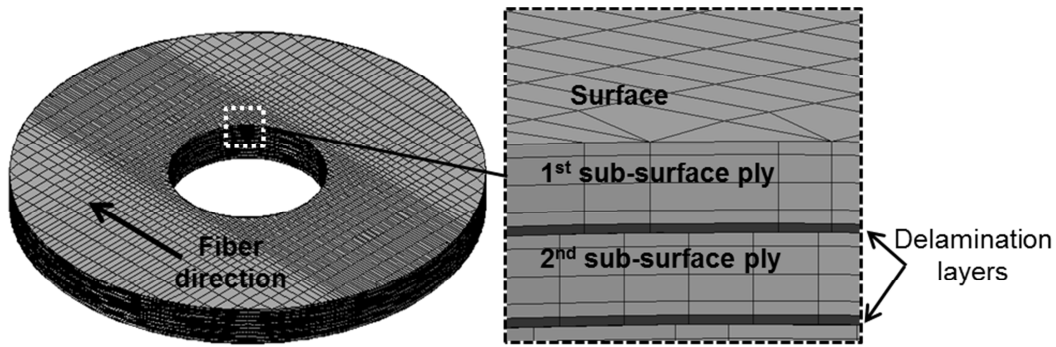


Figure 3-4 Sub-model with fiber-oriented mesh and detail of through-the-thickness discretization

### 3.4.2 Static Failure of OHT Coupons

#### 3.4.2.1 Test Results

Three 16-ply IM7/8552 carbon/epoxy coupons with symmetric  $[45/0/-45/90]_{2S}$  were quasi-statically loaded to ultimate failure with a 0.05in./min head displacement rate. Cross-section dimensions and failure loads are listed in Table 3-1. The DIC technique was used to monitor surface strains during loading. A random texture using white and black spray paint was generated on the surface of the specimen and a stereo digital camera set was used with commercially available DIC software Vic3D to measure the 3D surface shape and deformation. Figure 3-5 shows post failure pictures of the specimens with ultimate surface-ply failure. For specimen OHT3, it was possible to stop the test right after development of ultimate surface cracks, before the split-up of the specimen into two parts occurs by fiber cracking in the zero degree plies. Specimen OHT3 was subjected to post-failure two-dimensional X-Ray inspection. An additional specimen OHT4 was loaded to 36.92 kN (8300 lb) and inspected by 2D X-Ray under loading, before development of

ultimate failure, in order to provide better observation of matrix cracks in zero-degree plies.

Table 3-1 Cross-section dimensions and failure load for static OHT coupons

Specimen	Width, mm (in.)	Thickness, mm (in.)	Failure Load, kN (lbs)
OHT1	38.12(1.501)	2.641 (0.1040)	38.88 (8740)
OHT2	38.13(1.501)	2.638 (0.1039)	38.26 (8601)
OHT3	38.19(1.504)	2.642 (0.1040)	37.19 (8361)
AVG	38.15(1.502)	2.640 (0.1039)	38.11 (8567)

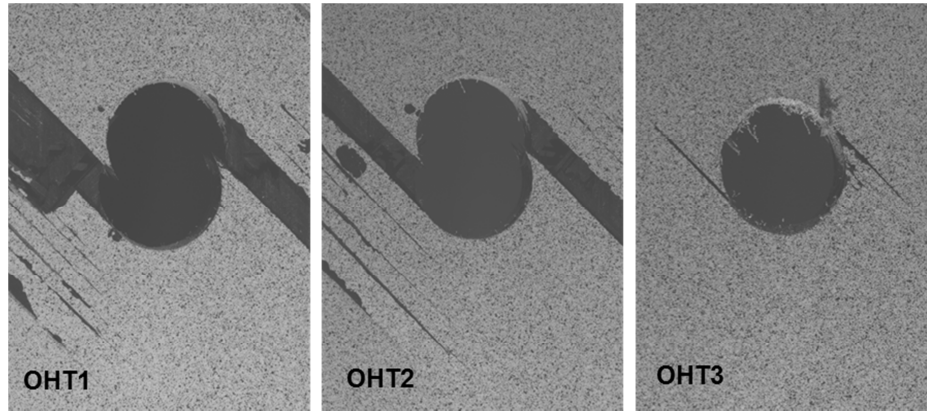


Figure 3-5 Surface-ply ultimate failure cracks in OHT coupons

#### 3.4.2.2 FE Simulations and Test Correlations

The progressive failure analysis showed that matrix cracks initiated first in the 90 degree plies around 20 kN (4500 lbs), growing from the locations of stress concentrations around the hole. As cracks develop in the 90° plies, they are accompanied by matrix cracking in the 45° plies and delaminations in the adjacent plies. As the load increases, one crack in the 45° surface ply ultimately grows further than any other 45° matrix crack,

leading to unstable crack propagation and ultimate failure. The development of matrix cracks in the zero degree plies happened shortly before ultimate failure was also observed.

Figure 3-6 compares FEM surface strains with DIC measurements at 22.41 kN (5037 lbs) tensile load, which corresponds to the onset of matrix cracks in the 45 degree surface ply. Figure 3-7 shows FEM and DIC strains at 32.20 kN (7239 lbs), with development of the ultimate 45 degree surface-ply matrix crack. Figure 3-8 displays the matrix cracks in all layers of the laminate based on 2D X-ray inspections of OHT3 and OHT4 specimens and FEM simulation results at 35.59 kN (8000 lbs).

Table 3-2 summarizes the simulation results and test data for loads and various damage events. Note that the ultimate failure for FEM simulation is reported when the surface crack reaches approximately a length equals to the radius of the hole, after which unstable growth was observed.

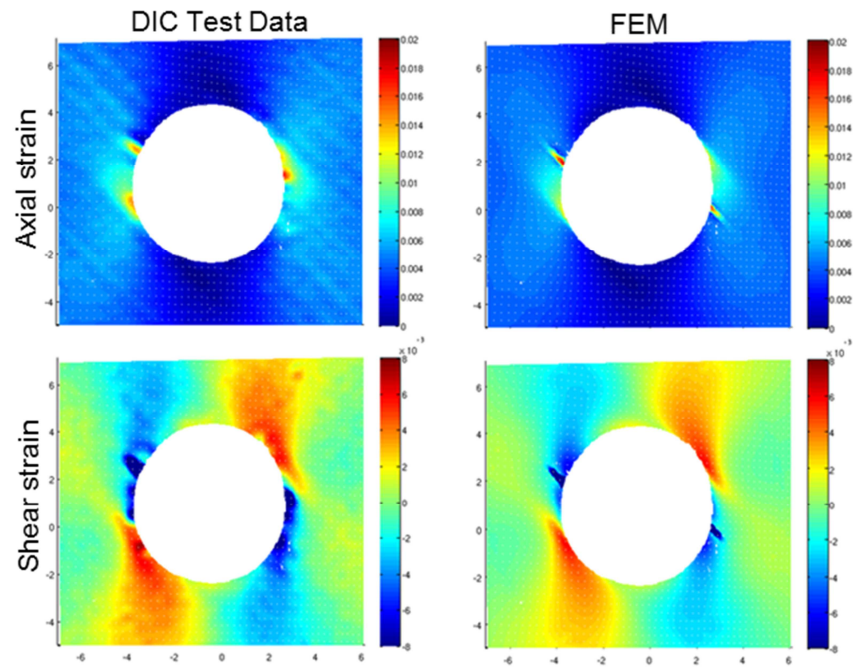


Figure 3-6 Surface strains at 22.41 kN (5037 lbs) tensile load

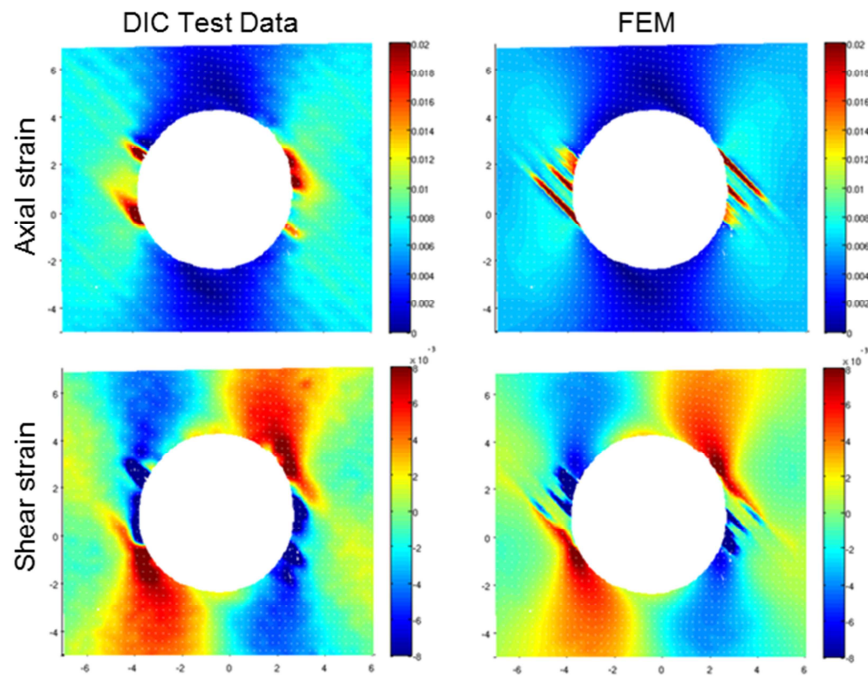


Figure 3-7 Surface strains at 32.20 kN (7239 lbs) tensile load

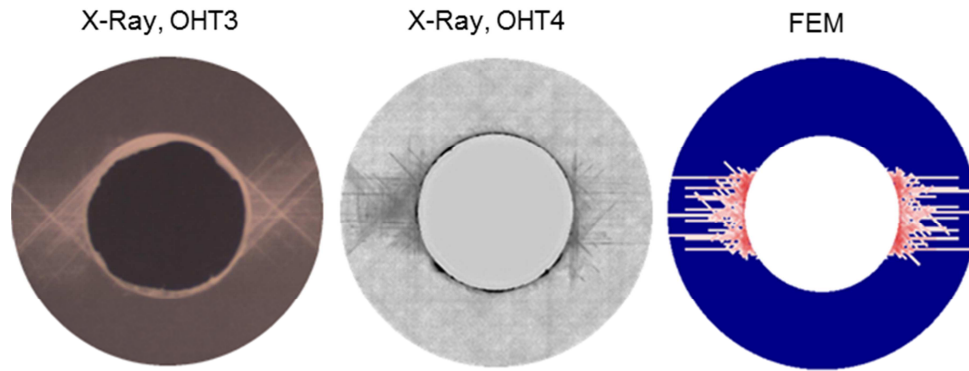


Figure 3-8 2D X-Ray images and simulation results for matrix cracks

Table 3-2 FEM-based and actual test loads for various stages of matrix cracking

Damage stage	FEM, kN (lbs)	Test OHT3, kN (lbs)	Test Average, kN (lbs)
First crack 90-deg. ply	20.4 (4586)	-	-
First surface crack 45-deg. ply	21.5 (4834)	22.4 (5038)	-
Development of ultimate surface crack 45-deg. ply	31.7 (7127)	32.5 (7313)	-
Ultimate failure	38.7 (8707)	37.2 (8361)	38.1 (8567)

### 3.4.3 Fatigue of OHT Coupons

#### 3.4.3.1 Fatigue Tests and Calibration of the FE Model

16-Ply quasi-isotropic IM7/8552 carbon/epoxy tape OHT coupons have been manufactured and tested to the ASTM Standard D7615 specifications [90]. The coupon dimensions and hole diameter were the same than for the static OHT tests. Two quasi-isotropic layups were considered:  $[45/0/-45/90]_{2S}$  (layup 1) and  $[45/90/-45/0]_{2S}$  (layup 2).



Layup 1 coupons were subject to constant amplitude load at 10 Hz frequency, up to 1,000,000 cycles. The minimum load was 2.22 kN (500 lbs) and the maximum load was 22.2 kN (5000 lbs). Layup 2 coupons were subject to constant amplitude loads ranging from 21.4 kN (4800) lbs to 24.9 kN (5600 lbs), same load ratio of 0.1, up to the number of cycles that resulted in approximately the same length of the ultimate surface crack.

The FE model used for failure simulation is similar to the model presented in section 3.4.1, and includes a local circumferential sub-model of the material around the hole where failure cracks are expected to develop. Displacement boundary conditions are provided by a global model, as illustrated on Figure 3-3. Symmetry boundary conditions are applied to the nodes lying on the half-thickness plane, as only one half of the model is represented. A fiber-oriented mesh with surface-based tie constraints between layers is used, as described previously. A sensitivity study was performed for the in-plane element size that simulates width of matrix cracks in the sub-model to ensure the objectivity of the crack band damage model, as discussed in section 3.2. The fatigue growth of the longest matrix surface crack (45 degree surface ply) was compared for different sizes and correlated with test results. DIC images taken throughout the cycling loading history of the specimen were used for measurements of crack length, as shown in Figure 3-9 for measurements at 1,000,000 cycles. Figure 3-10 shows the fatigue crack growth predictions for different in-plane element size (crack band width  $e$ ). As expected, reducing the crack band width results in faster fatigue crack growth, i.e. longer crack length for the same number of cycles. The best correlation with test measurements was found for an element size of 0.124 mm, as shown in Figure 3-10.

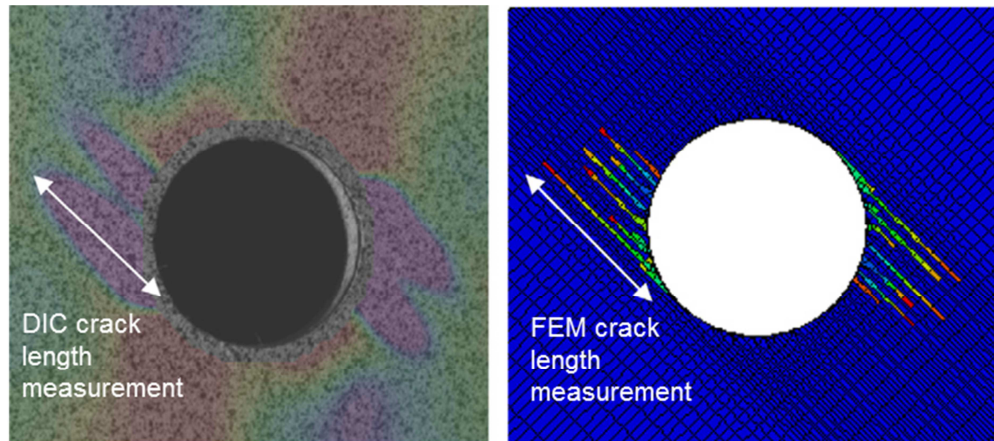


Figure 3-9 DIC and FEM based measurement of the longest matrix crack length in surface 45 degree ply of OHT specimen at 1,000,000 cycles

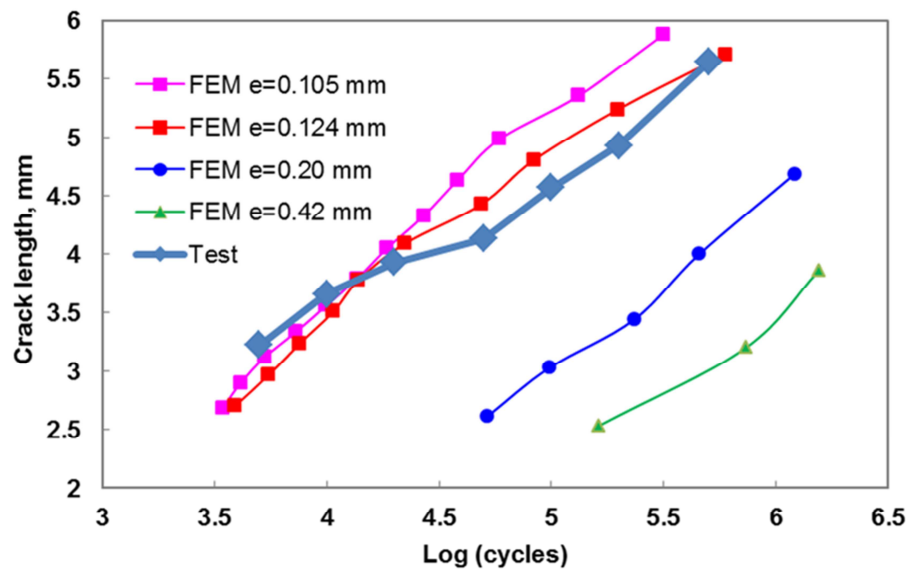


Figure 3-10 Comparison of the longest surface crack fatigue growth for different FE crack band width  $e$  and correlation with tests

As mentioned in the description of the fatigue damage algorithm in section 3.3, it is desirable to fail several elements during one fatigue step, to speed up the simulation. The cycle counter is then advanced accordingly, and stresses are recalculated due to element damage. Using higher number of failed elements per step enables faster simulation but failing too many elements at once can lead to incorrect simulation of the effects of progressive stress recalculation and result in inaccurate predictions. Figure 3-11 compares fatigue growth of the longest surface crack for different number of failed elements per fatigue step. Convergent behavior is observed with number of failed elements per step decreasing. Based on the results shown in Figure 3-11, a number of 50 failed elements per step was selected for the fatigue damage FE simulations in OHT coupons.

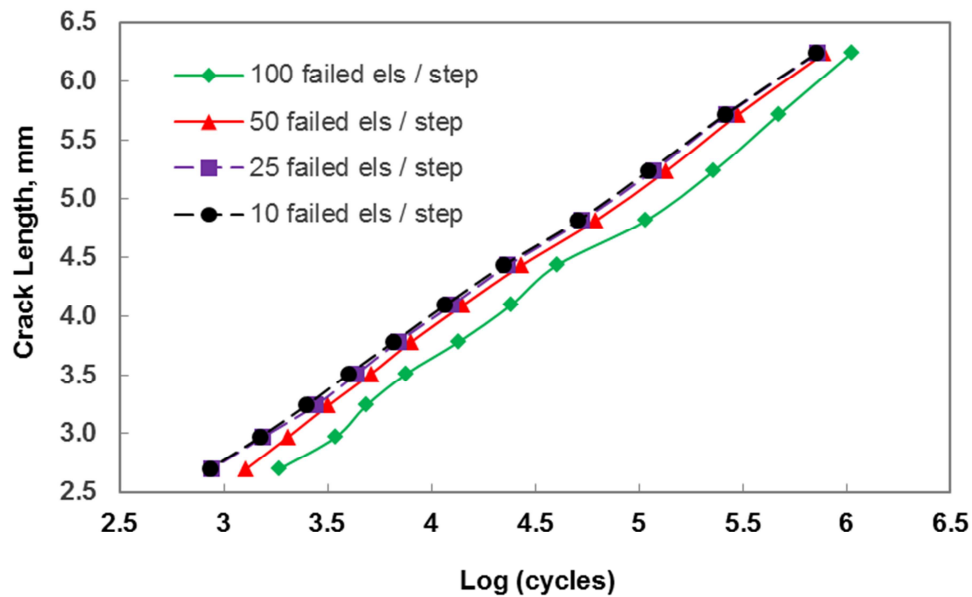


Figure 3-11 Comparison of the longest surface crack fatigue growth for different number of failed elements per fatigue step

#### 3.4.3.2 Fatigue Progression of Three-dimensional Damage and Interaction

FE simulation results for progression of matrix cracks and delamination were compared with three-dimensional micro-CT reconstructions of the OHT fatigue coupons. Over the past recent years, commercially available micro-CT systems have proven their abilities to detect manufacturing defects and structural damage in composites. A X5000 industrial CT system made by North Star Imaging Inc. with a 225 kV Microfocus X-ray tube and Varian 4030E series Flat Panel detector was utilized in this work. Details of the CT system used are provided in section 4.1. CT inspections of the OHT specimens were performed for different number of cycles throughout the fatigue loading; tests were stopped to allow for CT scans, and then started again.

Figure 3-12 shows the FE predictions of matrix cracks and delaminations, and the CT scan of the specimen compared after 1,000,000 cycles of fatigue loading for a test specimen with layup 1.

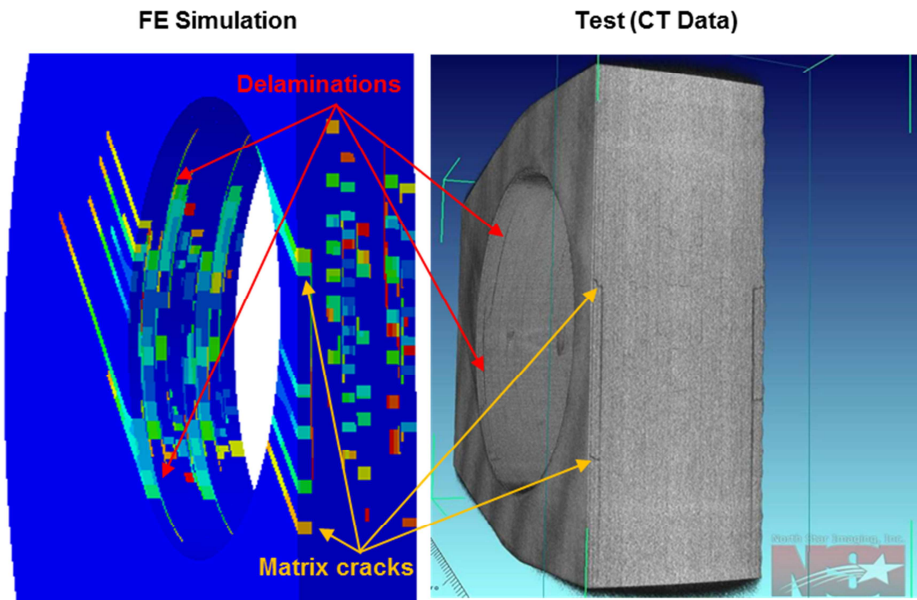


Figure 3-12 Comparison of FE fatigue failure predictions and CT scan of test specimen for layup 1

In the FE model, matrix cracks can be seen as lines of colored elements along the fiber direction on the surface of the specimen; they are also shown as colored squares at the inner hole surface and the through-the-thickness section of the model. Delaminations can be seen at the same through-the-thickness surfaces as thin lines of colored elements between the plies. Colors encode cycles to failure: elements in blue to green colors failed at low cycles ( $N < 100,000$ ) and elements in yellow to red colors failed at higher cycles ( $100,000 < N < 1,000,000$ ). The CT scan data shows both matrix cracks and delaminations as dark lines (due to lower density) oriented along fiber directions or between the plies, respectively. Matrix cracks and delaminations in the two plies just below the surface of the specimen are clearly identified since they remain open after unloading; a detailed inspection of the CT scan also reveals matrix cracks of smaller widths in further sub-surface plies. Figure 3-12 demonstrates excellent correlation for the

locations of major matrix cracks in surface and sub-surface plies and for the delaminations between these plies. Both the FE model and the CT scan show that matrix cracks and delaminations in the two top sub-surface plies demonstrate strong interaction and need to be modeled simultaneously to account for their reciprocal effects.

Figure 3-13 and Figure 3-14 show the comparison of matrix crack length and delamination sizes for the specimens with two different quasi-isotropic layups fatigued to 1,000,000 cycles. The Figures again demonstrate excellent comparison with subsurface CT measurements for both location and size of damage. Both simulations and tests clearly show cracks shifting from the surface matrix to delamination in the 1<sup>st</sup> sub-surface interface and to cracks in the 2<sup>nd</sup> sub-surface ply. The difference in delamination sizes and shapes between the two layups is captured by the FE simulation and is due to different fiber orientations at the 2<sup>nd</sup> sub-surface ply (zero-degree for layup 1 and 90-degree for layup 2), that lead to different matrix-dominated failure interaction.

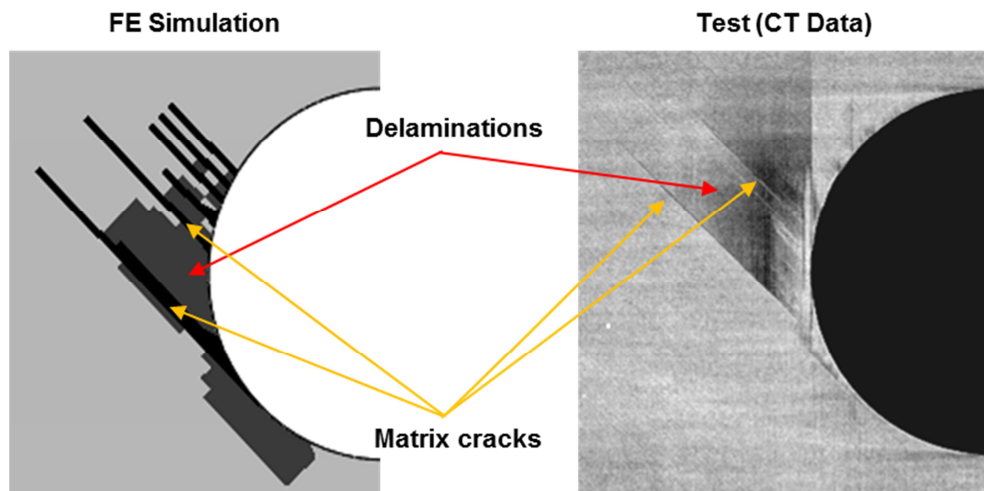


Figure 3-13 Matrix cracks in 45 degree surface ply and delamination in the sub-surface interface for FE predictions and CT data for layup 1 specimen at 1,000,000 cycles

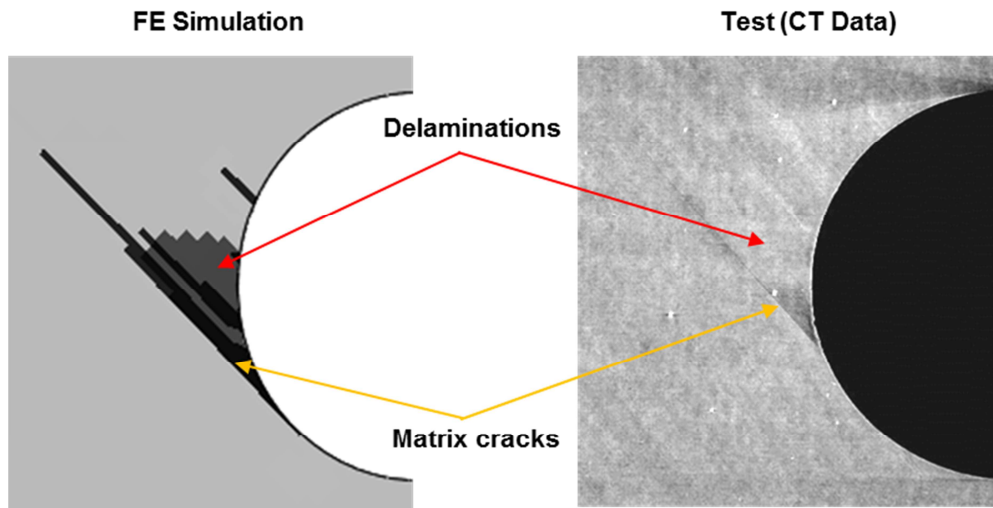


Figure 3-14 Matrix cracks in 45-degree surface ply and delamination in the sub-surface interface for FE predictions and CT data for layup 2 specimen at 1,000,000 cycles

#### 3.4.3.3 Fatigue Prediction for Different Peak Loads

Five OHT specimens with  $[45/90/-45/0]_{2S}$  layup 2 were tested at different peak loads for different number of cycles such that the longest surface crack reached approximately the same length. The loads and cycles are shown in Table 3-3. Load ratio was maintained at 0.1. Five different FE simulations were performed for the different peak load levels and simulation results were compared to tests at the number of cycles listed in Table 3-3.

Comparison with CT data is provided on Figure 3-15 showing surface ply-cracks and sub-surface interface delaminations for specimens at three different peak loads and fatigue cycles. The predictions demonstrate excellent agreement with tests for the locations of matrix cracks and delaminations. Good agreement is found also between FE-based and test measurements of the longest surface crack length. It is worth noting

however that for most specimens, predictions seem to overestimate the size of the delaminations. The delamination size is measured as illustrated on Figure 3-15. This could be due to delamination cracks partially closing up after unloading and therefore not being entirely detected in the CT-scans.

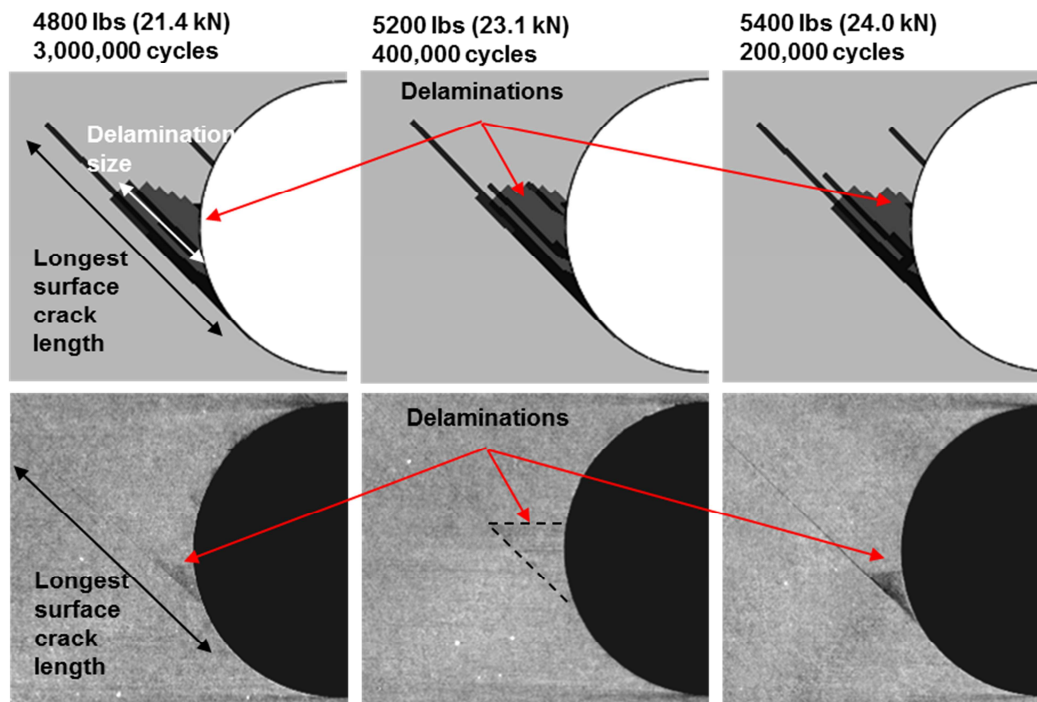


Figure 3-15 Comparison of FE predictions (top) and CT scans (bottom) for surface matrix crack and sub-surface delaminations for layup 2 specimens



Table 3-3 Comparison of simulation and test measurements for surface crack lengths and delaminations in OHT fatigue articles

Peak load, kN (lbs)	Cycles	Surface crack length, mm		Delamination size, mm	
		FEM	Tests	FEM	Tests
21.4 (4800)	3,000,000	6.2	7.5	2.0	1.0
22.2 (5000)	1,000,000	6.2	6.8	1.7	1.0
23.1 (5200)	400,000	6.2	6.2	1.8	1.0
24.0 (5400)	200,000	6.2	6.8	1.8	0.9
24.9 (5600)	100,000	6.2	6.2	1.8	1.1
22.2 (5000) layup 1	1,000,000	6.2	6.8	1.9	3.8

### 3.5 Failure Predictions for Open-hole Compression Specimens

#### 3.5.1 Damage Model for Compressive Failure

A continuum damage model is used for fiber and matrix compression failure, similar to the approach presented previously for matrix tension cracking and delamination in OHT coupons. For matrix compression failure, transverse material stiffness as well as shear stiffness properties are degraded to zero for a fully damaged element. As mentioned in section 2.3.2, it is assumed that failure under transverse compression is shear dominated and occurs in a fracture plane whose normal is rotated of angle  $\alpha$  along the fiber direction, as illustrated in Figure 2-3. Stresses expressed in the rotated coordinate system must be used in the failure criteria. Also, in a general case, degradation of the stiffness properties should be applied to the stiffness matrix derived in the rotated coordinate system.

However, it is worth noting that the fiber reinforced polymer matrix composite materials considered in this work, such as IM7-carbon/8552-epoxy, typically exhibit transverse isotropic material properties with respect to the fiber direction. Therefore, the material stiffness matrix is the same for any rotation about the fiber axis, which includes the rotation of angle  $\alpha$  of the fracture plane. The Jacobian matrix with degraded stiffness properties, which is required in the subroutine UMAT, can thus be calculated using the stress-strain relations given in the material planes in Eq. (2.2). The degraded Jacobian matrix can be used to update stresses in the material coordinate system, as required by UMAT and using Eq. (2.6).

For fiber compression failure, shear properties in the (1,2) and (1,3) material planes are degraded to zero and the normal Young's modulus in the fiber direction is degraded to the matrix Young's modulus (transverse Young's modulus), for convergence purposes. The damage model is summarized in the expressions below, with  $d_{cm}$  and  $d_{cf}$  the damage variables for matrix compression failure and fiber compression failure respectively.

- *Matrix compression failure:*

$$\begin{bmatrix} \varepsilon_{11} \\ \varepsilon_{22} \\ \varepsilon_{33} \end{bmatrix} = \begin{bmatrix} \frac{1}{E_{11}} & \text{Symmetric} \\ -\frac{\nu_{12}}{E_{11}} & \frac{1}{(1-d_{cm})E_{22}} \\ -\frac{\nu_{13}}{E_{11}} & -\frac{\nu_{23}}{E_{22}} & \frac{1}{E_{33}} \end{bmatrix} \begin{bmatrix} \sigma_{11} \\ \sigma_{22} \\ \sigma_{33} \end{bmatrix}$$

$$\gamma_{12} = \frac{\tau_{12}}{(1-d_{cm})G_{12}} + \left( \frac{\tau_{12}}{(1-d_{cm})K_{12}} \right)^{\frac{1}{n_{12}}} \quad (3.11)$$

$$\gamma_{13} = \frac{\tau_{13}}{G_{13}} + \left( \frac{\tau_{13}}{K_{13}} \right)^{\frac{1}{n_{13}}}$$

$$\gamma_{23} = \frac{\tau_{23}}{(1-d_{cm})G_{23}} + \left( \frac{\tau_{23}}{(1-d_{cm})K_{23}} \right)^{\frac{1}{n_{23}}}$$

- *Fiber compression failure:*

$$\begin{bmatrix} \varepsilon_{11} \\ \varepsilon_{22} \\ \varepsilon_{33} \end{bmatrix} = \begin{bmatrix} \frac{1}{(1-d_{cf})E_{11}} & \text{Symmetric} \\ -\frac{\nu_{12}}{E_{11}} & \frac{1}{E_{22}} \\ -\frac{\nu_{13}}{E_{11}} & -\frac{\nu_{23}}{E_{22}} & \frac{1}{E_{33}} \end{bmatrix} \begin{bmatrix} \sigma_{11} \\ \sigma_{22} \\ \sigma_{33} \end{bmatrix}$$

$$\gamma_{12} = \frac{\tau_{12}}{(1-d_{cf})G_{12}} + \left( \frac{\tau_{12}}{(1-d_{cf})K_{12}} \right)^{\frac{1}{n_{12}}} \quad (3.12)$$

$$\gamma_{13} = \frac{\tau_{13}}{(1-d_{cf})G_{13}} + \left( \frac{\tau_{13}}{(1-d_{cf})K_{13}} \right)^{\frac{1}{n_{13}}}$$

$$\gamma_{23} = \frac{\tau_{23}}{G_{23}} + \left( \frac{\tau_{23}}{K_{23}} \right)^{\frac{1}{n_{23}}}$$

The damage evolution law presented in Eq. (3.4) is used for progressive failure. As mentioned previously, the normal stiffness properties in the fiber direction are degraded to the matrix stiffness, which is assumed to be an isotropic material. Therefore

the  $k_f$  stiffness ratio for the damage variable  $d_{fc}$  in the fiber direction is assigned to the ratio of transverse Young's modulus to the Young's modulus in the fiber direction, i.e.  $k_f = E_{22}/E_{11}$ . For all other material directions and for matrix compressive failure, the elements are fully degraded with  $k_f = 10^{-6}$ .

The FE model used for simulation of compressive failure of OHC specimens was similar to the model developed for the OHT specimens described in section 3.4.1. The tensile load applied to the global model is replaced by a compressive load with the same boundary conditions, and the sub-modeling approach with oriented local mesh around the hole is used for failure simulations. Similarly to the OHT model, only one half of the specimen was represented due to symmetry of the layup. Damage model for delamination failure is assigned to the discrete layer of delamination elements at the ply interface, as discussed previously.

### 3.5.2 Static Failure of OHC Coupons

#### 3.5.2.1 Tests and FE Results

12-ply [0/-45/90/45]<sub>s3</sub> IM7/8552 OHC coupons were manufactured and tested in quasi-static loading per ASTM D 6484 specifications [91].

The DIC technique was used to monitor surface strains and progression of surface-ply cracks. Quasi-static compressive loading of the specimen was stopped at 10,000 lbs (44.5 kN) when fiber failure in the zero degree surface ply is well developed and visible, but before ultimate structural failure of the laminate. The specimens were then subject to post-failure non-destructive inspection with the North Star X-Ray micro-CT system. Figure 3-16 shows the 3D reconstruction results for an OHC specimen after 10,000 lbs compressive loading. A fiber failure crack is shown to develop in the 0-degree

surface-ply from both side of the hole with matrix-cracks and delaminations along the crack path. Fiber failure accompanied by matrix cracks and delamination was also found in the adjacent plies, although less visible.

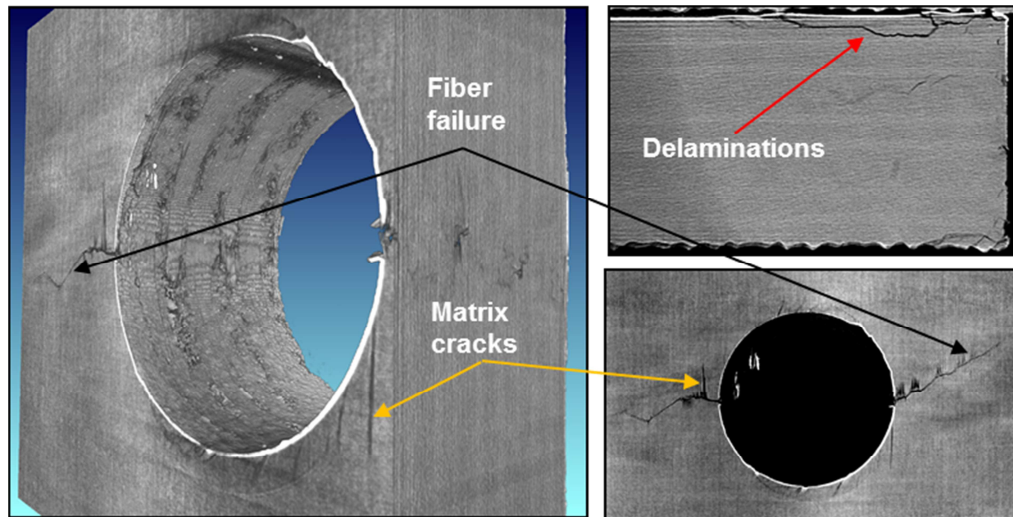


Figure 3-16 3D CT reconstruction of OHC specimen showing structural damage after 10,000 lbs (44.5 kN) compressive loading

The fiber-aligned sub-model of the OHC coupon around the hole was used for FE simulation of failure progression. The analysis showed that failure initiated with matrix compression cracking developing in the zero degree plies around 5000 lbs (22.2 kN), accompanied by delaminations at the interface with the adjacent ply. The simultaneous development of matrix compression cracks and delaminations suggests strong interaction between the two failure mechanisms, as shown in Figure 3-17. Matrix cracks in the 45-degree plies start to appear around 6000 lbs (26.7 kN), as compression matrix cracks and delaminations develop further in 0-degree plies. Figure 3-18 demonstrates that strong interaction is also observed between matrix cracks and the development of

delaminations at the ply interface of 45-degree plies. Compression matrix failures and delaminations in the surface and sub-surface 0-degree plies lead to compressive fiber failure which initiates around 6600 lbs (29.4 kN). Matrix cracks in the 90-degree plies start to grow around 7800 lbs (34.7 kN). The simulation stopped at 9500 lbs (42.2 kN), as the growth of fiber failure in the surface 0-degree ply leads to local buckling in the FE model with large element distortion resulting in difficulties to obtain a converged solution. A summary of matrix and fiber cracks developments in the FE model is presented in Table 3-4.

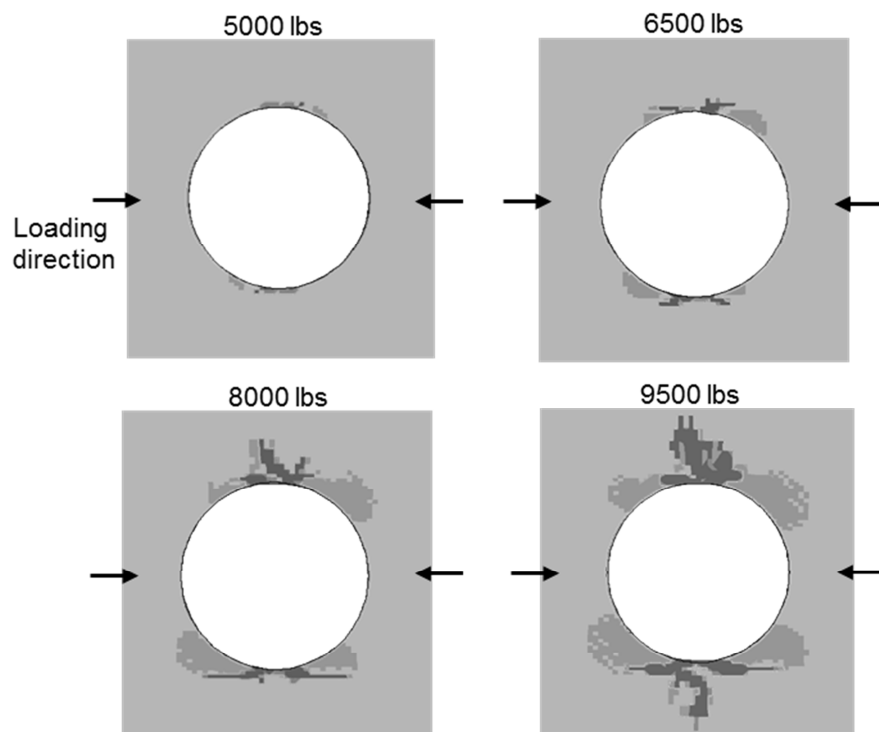


Figure 3-17 Development of matrix compression cracks and compressive fiber failure (dark grey) and delaminations (lighter grey) in OHC surface 0° ply

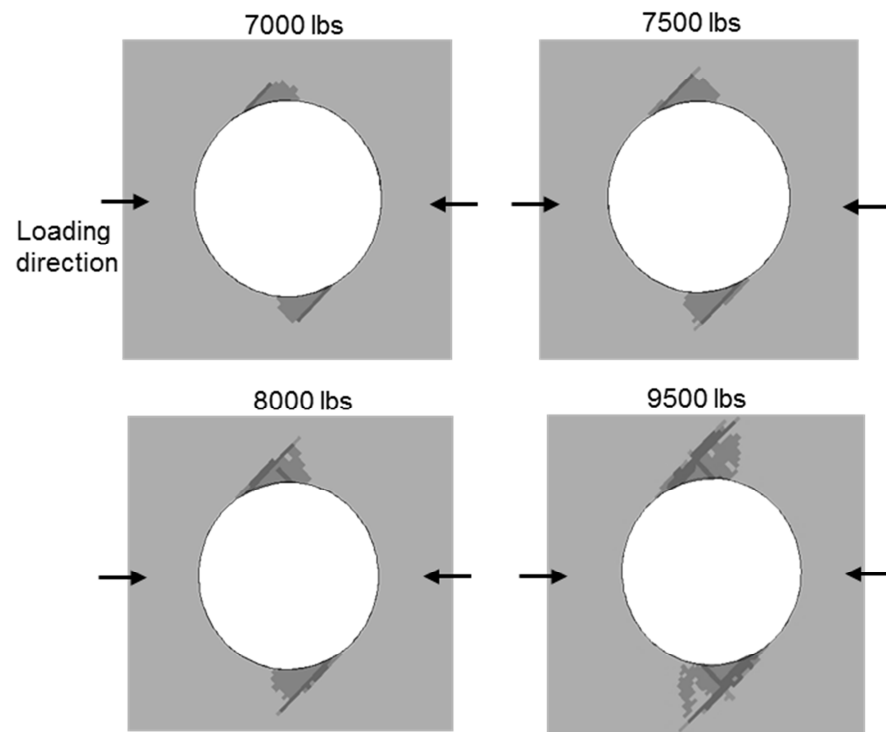
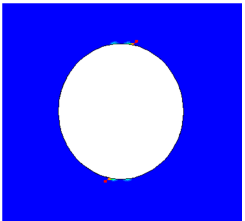
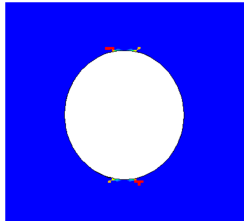
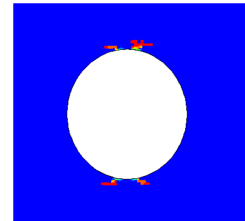
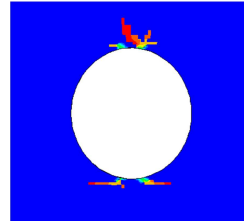
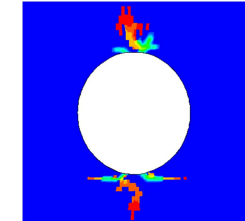
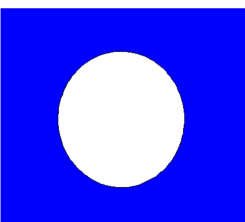
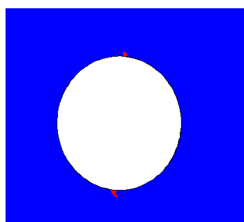
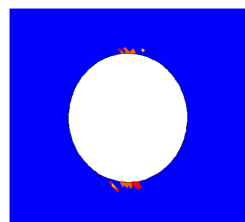
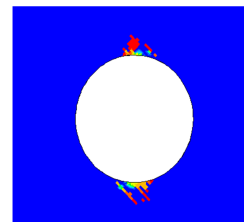
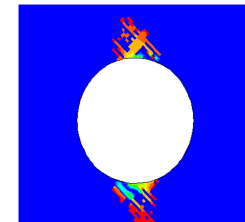
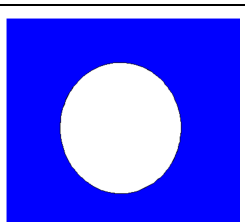
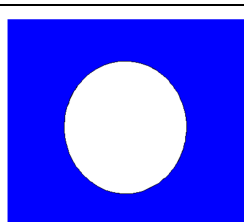
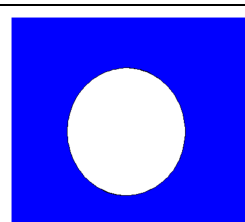
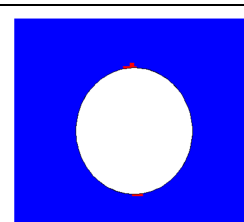
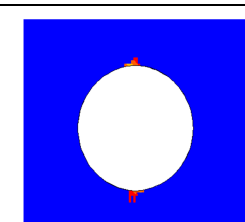


Figure 3-18 Development of matrix cracks (dark grey) and delaminations (lighter grey) in  
OHC first sub-surface 45° ply

Table 3-4 FE-based simulation of matrix cracks and fiber failure developments in OHC specimens

Compressive load	5000 lbs (22.2 kN)	6000 lbs (26.7 kN)	6600 lbs (29.4 kN)	7800 lbs (34.5 kN)	9500 lbs (42.3 kN)
0° ply (surface ply #1)					
45° ply (ply #10)					
90° ply (ply #10)					
Failure event	Initiation of compressive matrix cracking in 0° plies	Initiation of matrix cracking in 45° plies	Development of compressive fiber failure in 0° plies	Initiation of compressive matrix cracking in 90° plies	Growth of 0° ply fiber failure leading to large element distortion



#### 3.5.2.2 Correlation with X-Ray Micro-CT Inspection

A first attempt to correlate FE simulation results for crack growth and location with 3D CT reconstructions of OHC specimens after 10,000 lbs (44.5 kN) compressive loading seemed to indicate that crack lengths and developments were over-estimated in the numerical model. Also, significant matrix cracks and delaminations were predicted at locations where no apparent damage was visible in the CT data. In fact, only fiber failure in the zero degree plies and delamination in the adjacent plies were observed in the CT reconstructions, whereas the FE model predicted matrix cracks and delaminations for each laminate ply groups, as shown in Figure 3-18 and Table 3-4. Closer local CT inspections using maximal magnification suggested that cracks were probably present at expected locations, but fracture surfaces “closed up” during unloading of the specimens, preventing successful damage detection in the CT scans.

New equipment developed under US Office of Naval Research’s Defense University Research Instrumentation Program (DURIP) grant became available for the North Star CT system used in this work, enabling CT non-destructive inspection under load. Figure 3-19 shows the integrated load frame with 10,000 lbs tensile loading capacity customized for the North Star X 5000 system. The load frame includes a load cell for load control and a rotational platform synchronized with the CT system during acquisition of the 2D X-Ray images used for 3D reconstruction.



Figure 3-19 Integrated load frame for CT scan under load

The integrated load frame was used to apply a 5000 lbs (22.2 kN) tensile load to the OHC specimens after static tests at 10,000 lbs (44.5 kN). The stabilized displacement suggested that no further damage developed in the specimens due to tensile loading. The tensile load allowed to “open-up” the fracture surfaces generated during compression loading and many cracks previously undetected in unloaded specimens became clearly visible. Figure 3-20 shows the comparison between FEM results at 9,500 lbs (42.3 kN) and CT data under tensile load after OHC test at 10,000 lbs (44.5 kN). Excellent correlation between simulation and test data is demonstrated with very good agreement for crack lengths and crack locations of matrix and fiber failures in each ply group of the OHC laminate.

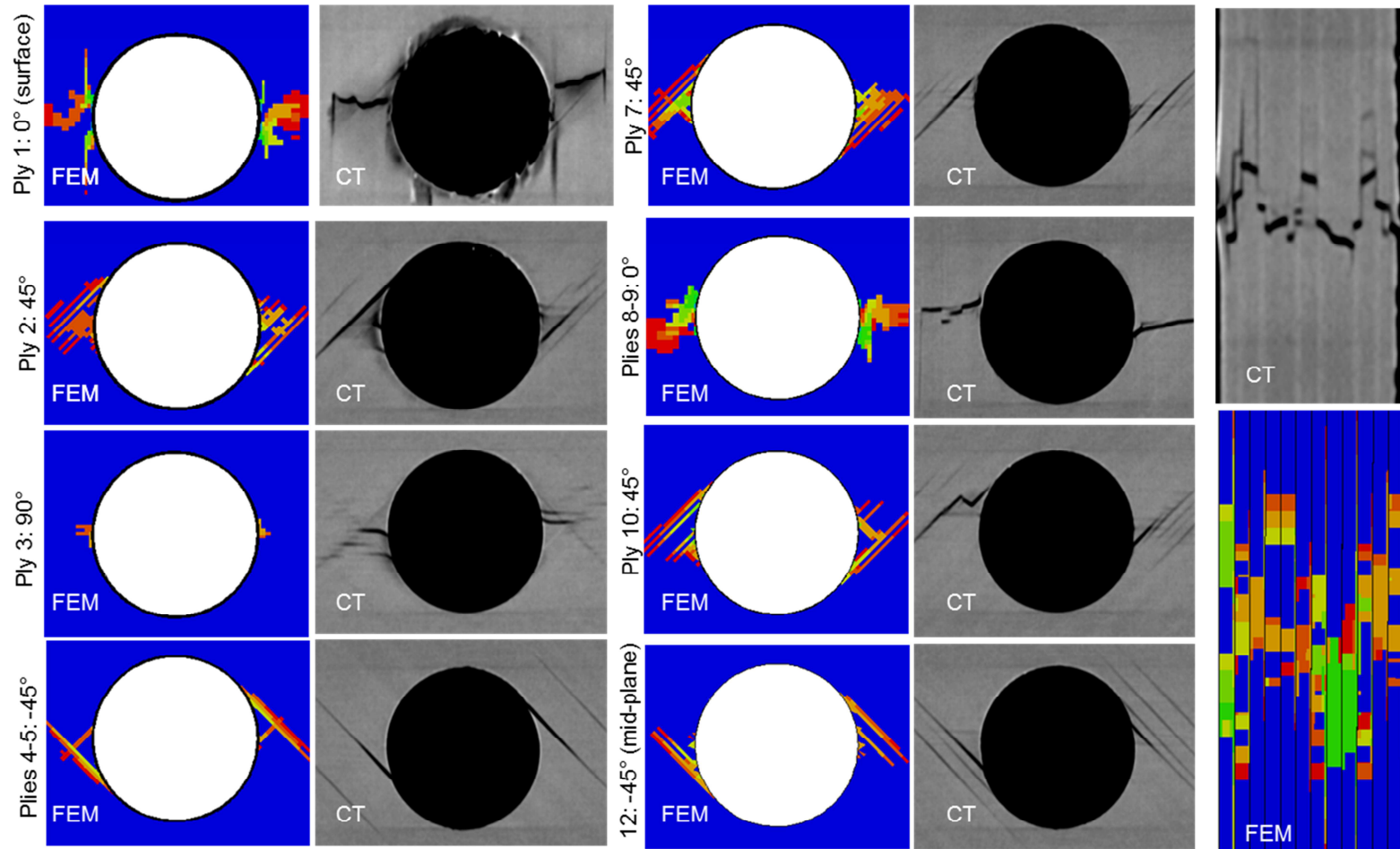


Figure 3-20 Comparison of FE predictions and CT data under loading for OHC specimens

## Chapter 4

### Integration of Manufacturing Defects

This chapter presents a structural analysis methodology for integration of porosity defects into FE models for assessment of their effects on strength and fatigue constitutive properties. Unique features of this methodology include X-Ray CT three-dimensional measurements of the defect features and integration into FE-based stress analysis for assessment of strength and fatigue performance. Curved-beam test articles are used to validate the method. X-Ray CT measurements of porosity defects present in CB specimens are integrated into FE-based stress analysis to capture the effects of defects on the InterLaminar Tensile Strength (ILTS) and ILT fatigue behavior. Once the effects of manufacturing defects are captured through transfer of the CT measurements into a three-dimensional FE model, their contribution to the scatter in the test data could be quantified, and reliable interlaminar material properties determined.

#### 4.1 Non-destructive Inspection of Manufacturing Defects by X-Ray Tomography

Recent advances in high-resolution non-destructive evaluation methods based on X-Ray computed Tomography lead to a fundamental change in the defect analysis in composites from just detection to accurate non-destructive measurement of defect three-dimensional geometry and location. Since the pioneering work of Hounsfield in the 1970s [92], X-Ray Computed Tomography has been applied to a variety of problems in material research, in addition to its original application in medicine imaging. The recent appearance of commercial CT systems has made micro-CT more accessible for industrial and laboratory testing. Improvements in spatial resolution and computer hardware used for reconstruction of 3D volumes have also made X-Ray computed micro-

tomography practical for characterization of damage and internal flaws in composite materials [72].

An industrial micro-CT system with a 225 kV Microfocus X-Ray tube and Varian 4030E series flat panel detector built by North Star Imaging, Inc presented in Figure 4-1 is utilized in this work. Figure 4-2 shows the operation basics and major components of the CT system used.



Figure 4-1 North Star Imaging industrial micro-CT system

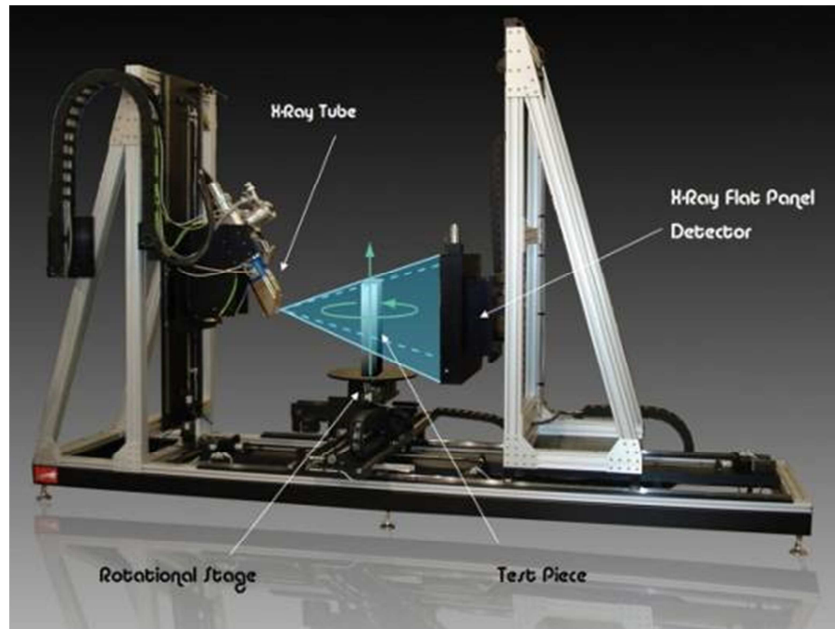


Figure 4-2 Operation basics and major components of the CT system

The X-ray tube produces a conic beam of electrons that penetrates the object to be analyzed and generates a 2D radiograph projection on the X-ray flat panel detector. The object is positioned on a precision rotational stage and a series of 2D radiograph images are captured during the 360 degrees (complete) or 180 degrees (half) rotation of the object at a constant step. From the series of radiograph, CT reconstruction algorithms are used to generate the 3D volumetric representation of the object. The efX-CT reconstruction software provided by Northstar Imaging was used for generating the 3D CT data. The reconstruction software is based on the filtered back-projection algorithm originally proposed by Bracewell and Riddle [95].

The resolution of the CT reconstruction is determined by the pixel size in the detector (0.127 mm for the Varian detector used in this work) and the geometric magnification, which is in turn determined by the dimensions of the detector panel and the dimension of the area of interest. For a typical scan area of 20 mm, a scan resolution

of 12  $\mu\text{m}$  was obtained with an un-sharpness of 7  $\mu\text{m}$  to ensure optimum focus of the cone-beam CT system. Figure 4-3 shows cross-sectional CT images of carbon/epoxy unidirectional curved beam specimens with typical porosity defects obtained from the 3D volumetric model reconstructed in the efX-CT software by North Star Imaging. The 3D reconstructed volume is represented as a set of voxels (3D pixels) where the intensity of each voxel (called the gray value) can be related to the material density [96]. Porosity voids, which often result from air pockets entrapped between the plies of the tape composite material, are identified as the thin black areas in the cross-sectional CT slides.

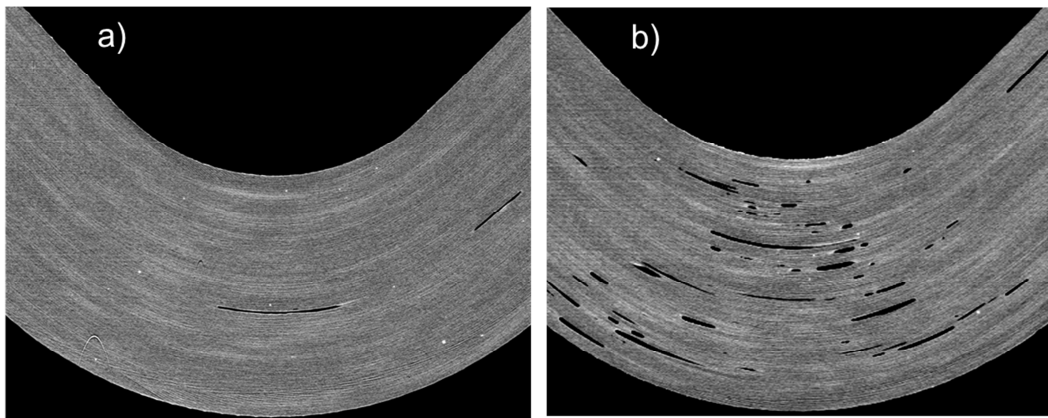


Figure 4-3 Cross-section CT slides of carbon/epoxy unidirectional curved beam specimens manufactured at a) 80 psi curing pressure (nominal) and b) 25 psi showing porosity defects.

Porosity voids typically have larger aspect ratios in the fiber direction, resulting in the thin curved shapes shown along the composite plies and often degenerating into noodle-like shape as shown in Figure 4-1. This geometry can be attributed to expansion of air pockets that exhibit the largest resistance in the thickness direction due to application of the curing pressure. The void thickness was found to be the smallest

dimension in all the specimens considered in this work and was of the order of a ply thickness. The smallest dimension void thickness found was approximately 1/3 of the ply thickness, i.e. 60 $\mu$ m. For comparison, this dimension is about 5 times larger than the 12 $\mu$ m resolution allowed by the Northstar CT system. Therefore, high-fidelity measurements of void geometry could be achieved.

#### 4.2 Measurement of the Three-dimensional Defect Geometry

The interface of the Northstar efX-CT software allows for user measurements of the dimensions of visible features in the 3D CT reconstruction. However this manual process can be time consuming and may also be unreliable due to errors in the interpretation of the CT information. An automatic procedure is therefore preferable. Automatic extraction of the three-dimensional geometry of the porosity defects is also useful for the determination of the total porosity content, i.e. the volume percentage occupied by the porosity void. The porosity volume is typically used in industrial applications to assess the manufacturing quality of composites parts and a porosity content of 2% is commonly considered as acceptable in aerospace applications. An automatic extraction method based on image processing techniques applied to cross-sectional CT slides of the 3D volumetric data was used in this work for detection and measurement of the porosity defects in carbon/epoxy test specimens.

One of the challenges in the accurate automatic detection and measurement of porosity void using the X-Ray micro-CT data is the selection of the gray value threshold that separates solid material from air. Nikishkov et al. [97] proposed a threshold selection method based on the average of the air and material gray value and using a sub-pixel contouring method for material-void separation. They demonstrated the accuracy and



robustness of the method on specimens with drilled micro-holes of known diameter and showed excellent correlation with microscopic measurements for sample voids in cut sections of Carbon/Epoxy composite specimens.

The method developed by Nikishkov et al. [97] is used in this work for automatic measurements of porosity defects. First, the average gray value between air and material in the reconstructed volume is determined from the pixel histogram of the CT scan. The histogram shows the distribution of number of 3D pixels for each level of gray value found in the reconstructed volume. Figure 4-4 shows a typical pixel histogram for the CT reconstruction of a Carbon/Epoxy specimen and the determination of the gray value threshold for air/material between the material and air peaks.

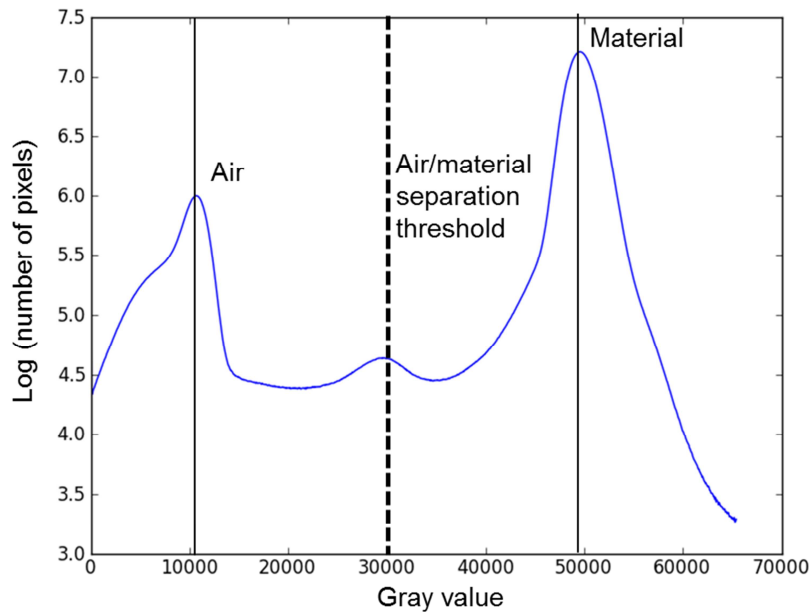


Figure 4-4 Pixel histogram for a Carbon/Epoxy specimen and determination of the gray value threshold for air/material separation

Once the separation threshold is determined, cross-sectional images of the CT volume are generated along the direction perpendicular to the pre-dominant void length. As illustrated in Figure 4-3, the pre-dominant void length direction typically corresponds to the fiber direction in unidirectional curved beam specimens. For each section image from the CT data, the grey value separation threshold is used to apply a binary threshold transformation to the grey scale pixelated image. Contours of the voids are then determined with sub-pixel accuracy from the binary image by using the contouring algorithm available in the Python 2D plotting library package *matplotlib*. The contour of each void can be approximated by fitting a known geometrical shape, from which characteristic dimensions can be extracted. In the case of the porosity voids identified in unidirectional Carbon/Epoxy curved-beam specimen, elliptical fits defined in the cylindrical coordinate system associated to the radius area of the specimen are used, as illustrated on Figure 4-5.

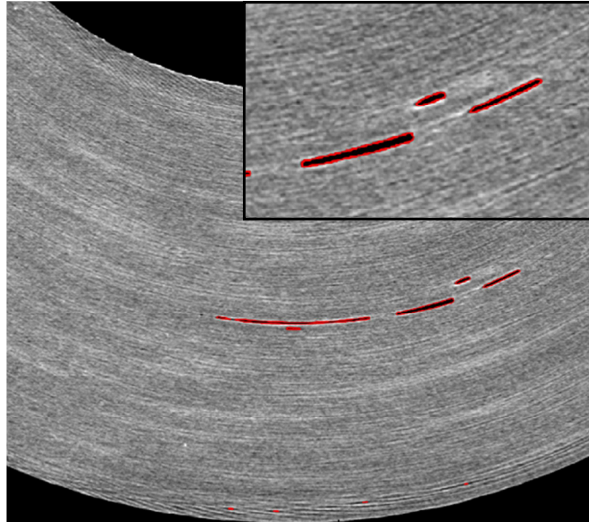


Figure 4-5 Elliptical fits in cylindrical coordinates (in red) for the detection of porosity voids in cross-section CT images of unidirectional carbon/epoxy curved beam specimens

Once all section images are processed, the next step is to connect 2D sections of the voids in three dimensions by finding intersecting void sections in the adjacent sectional images. Once all the cross-sections are connected, the 3D geometric properties of the voids can be determined. Typically, about 1000 cross-sectional CT images are used for measurement of the porosity defects. For measurements of defects in the curved beam specimens illustrated in Figure 4-5, this represents a spatial resolution of about 13  $\mu\text{m}$  along the width direction (0.5 in. wide specimens), which is consistent with the 12  $\mu\text{m}$  resolution in voxel size allowed by the Northstar micro-CT system.

The set of 3D coordinates of the contour points, as well as the parameters of the three-dimensional geometric approximations (a tri-axial ellipsoid in cylindrical coordinate was used in curved-beam specimens) for each void, can be written in a text file for transfer into FE models. The measurement data obtained from the CT reconstruction is

also used to determine the total percentage of porosity voids in the CT volume. For each cross-section, the contour points of the voids are used to calculate the area of the void. The percentage of void area is then calculated for each section, and averaged over the volume.

Accuracy of the CT-based method for extraction of the porosity volume was demonstrated in [97] for Carbon/Epoxy fabric specimen and showed that the method allowed more robust and reliable porosity content measurements compared to results obtained through the teardown and microscopic evaluation of specimens sections.

### 4.3 Effect of Porosity Defects on Interlaminar Tension Performances

#### 4.3.1 *Curved-beam Test*

One of the major barriers to accurately predict failure for polymer-matrix composites has been the lack of reliable matrix-dominated material properties which could be used as a basis for the development of accurate failure criteria. In particular, interlaminar tensile strength (ILTS) and fatigue properties, which are generally the weakest basic structural properties of a laminate composite system, have been challenging to characterize. Accurate measurements of ILT strength and fatigue properties are needed to capture delamination failure which is one of the primary failure modes for aerospace composite structural designs. A major technical challenge to characterizing ILT behavior is extreme sensitivity to manufacturing defects including porosity that could lead to significant scatter in test results. Therefore, test results may be coupon-independent and reflect the manufacturing quality rather than coupon-independent material properties.

The curved-beam test configuration is currently used in the ASTM Standard D 6415 [73] to measure the ILTS of fiber-reinforced polymer-matrix composites. Figure 4-6 shows a typical four-point bending test for the ASTM D 6415 curved-beam test. The failure mode is tensile delamination that starts in the radius area, typically at about two third of the thickness corresponding to the maximum interlaminar tensile stress location, and quickly propagates through the flanges.

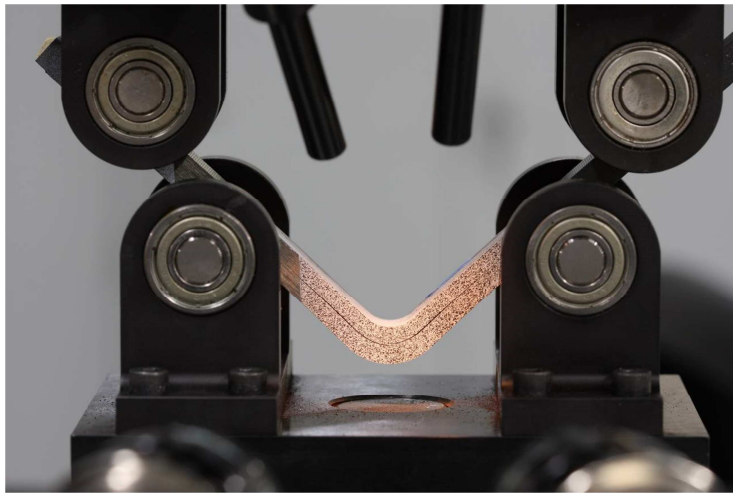


Figure 4-6 ASTM D 6415 test setup and tensile delamination failure of a unidirectional Carbon/Epoxy curved-beam specimen

Curved-beam specimens are applicable to assessment of the effects of porosity on ILT performance. Porosity can be easily introduced in the curved-beam specimens; the curved-beam radius area susceptible to delamination onset is far away from the attachments of the test fixture; and the nondestructive inspections can be limited to the radius area. Therefore, such specimens are the strongest candidate to study the effects of porosity on ILT behavior. Curved-beam specimens are also representative of many structural details found in aerospace composite designs.

#### 4.3.2 Interlaminar Tensile Strength

Ten 36-ply thick IM7/8552 carbon/epoxy unidirectional curved-beam specimens were manufactured per ASTM D 6415 specifications [73], except the width was reduced from 1 in. to 0.5 in. (25.4 mm to 12.7 mm). The width reduction was based on previous tests of both 1-in. and 0.5 in. wide curved-beam specimens which resulted in similar average ASTM D 6415 interlaminar tensile strength and similar scatter. A 0.0072 in. (183  $\mu\text{m}$ ) cured-ply thickness was used, resulting in a 0.26 in. (6.6 mm) thickness of the flat flanges. The average cured ply thickness in the radius of the curved-beam specimens was up to 5% higher compared to the flat flanges. A curved-beam laminate was laid on a male tool (an angle bracket), and a matching female tool (another angle-bracket) was placed on top of the laminate and cured in an autoclave. The outer corner of the male bracket had 0.25 in. (6.4 mm) radius and the inner corner of the female bracket had 0.5 in. (12.7 mm) radius. These two brackets formed the inner and outer surfaces and corners of the curved-beam laminate. After the laminate was cured, it was cut into curved-beam coupons. Figure 4-6 shows the ASTM D 6415 test setup. A standard ASTM D 6415 test fixture was used. The 0.875 in. (22.2 mm) diameter supports are mounted on roller bearings with a distance of 4 in. (10.2 cm) between the top supports and 3 in. (76.2 cm) between the bottom supports. The ASTM D 6415 test fixture was placed in an uniaxial servo-hydraulic load frame with 5.5 kip (25 kN) load cell capacity and the specimens were loaded at the standard 0.05 in/min displacement rate until delamination failure. Delaminations initiated in the curved-beam radius and immediately propagated through the flanges; all specimens exhibited similar behavior.

Failure loads and ILTS values obtained for the ten specimens tested are listed in Table 4-1. The ILTS is obtained from the closed-form approximation of the maximal interlaminar tensile stress developed by Lekhnitskii [98]:

$$\sigma_{max} = -\frac{CBS}{r_o^2 g} \left[ 1 - \frac{1 - \rho^{\kappa+1}}{1 - \rho^{2\kappa}} \left( \frac{r_m}{r_o} \right)^{\kappa-1} - \frac{1 - \rho^{\kappa-1}}{1 - \rho^{2\kappa}} \rho^{\kappa+1} \left( \frac{r_m}{r_o} \right)^{\kappa+1} \right] \quad (4.1)$$

Where:

$$g = \frac{1 - \rho^2}{2} - \frac{\kappa}{\kappa + 1} \frac{(1 - \rho^{\kappa+1})^2}{1 - \rho^{2\kappa}} + \frac{\kappa \rho^2}{\kappa - 1} \frac{(1 - \rho^{\kappa-1})^2}{1 - \rho^{2\kappa}}, \kappa = \sqrt{\frac{E_\theta}{E_r}}, \rho = \frac{r_i}{r_o} \quad (4.2)$$

$$r_m = \left[ \frac{(1 - \rho^{\kappa-1})(\kappa + 1)(\rho r_o)^{\kappa+1}}{(1 - \rho^{\kappa+1})(\kappa - 1)r_o^{-(\kappa-1)}} \right]^{\frac{1}{2\kappa}} \quad (4.3)$$

$$CBS = -\frac{P_f}{2w \cos(\phi)} \left( \frac{d_x}{\cos(\phi)} + (D + t) \tan(\phi) \right) \quad (4.4)$$

Where  $P_f$  is the total load at failure,  $\phi$  is the measured angle of the loading arm from horizontal,  $d_x$  is the horizontal distance between the centerlines of two top and bottom adjacent rollers,  $D$  is the diameter of the loading rollers,  $t$  is the specimen thickness,  $E_r$  and  $E_\theta$  are the moduli in the radial and tangential directions, respectively,  $r_i$  and  $r_o$  are the inner and outer radii of the curved segment.

Table 4-1 Failure load and ASTM D 6415 ILTS for IM7/8552 curved-beam specimens

<b>Specimen</b>	<b>Failure Load, kN, (lbs)</b>	<b>ILTS, MPa (ksi)</b>
<b>1</b>	2.24 (503)	83.4 (12.1)
<b>2</b>	1.34 (302)	52.4 (7.6)
<b>3</b>	1.93 (435)	70.3 (10.2)
<b>4</b>	2.61 (586)	93.1 (13.5)
<b>5</b>	1.27 (286)	50.3 (7.3)
<b>6</b>	0.93 (210)	37.9 (5.5)
<b>7</b>	1.85 (416)	68.9 (10.0)
<b>8</b>	2.47 (555)	94.5 (13.7)
<b>9</b>	2.45 (550)	93.8 (13.6)
<b>10</b>	2.06 (463)	81.4 (11.8)
<b>Average</b>	<b>1.91 (430)</b>	<b>72.4 (10.5)</b>
<b>CV</b>	<b>28.2%</b>	<b>26.5%</b>

An average ILTS of 10.5 ksi (72.4 MPa) is obtained with a large scatter as indicated by the 26.5% Coefficient of Variation (CV). It is worth noting that the locations of delaminations observed in the curved-beam specimens were not uniform; and did not necessarily coincide with the location of the maximum ILT stress predicted by FE analysis for a defect-free specimen. Figure 4-7 shows a theoretical defect-free distribution of ILT stresses in the curved-beam radius area, calculated using three-dimensional finite element (FE) analysis. Details on the FE model can be found in section 4.4.1 and on Fig. 6 (global model). The maximum ILT stress occurs at about two third of the specimen thickness, at the symmetry plane corresponding to the apex of the curved part of the specimen.



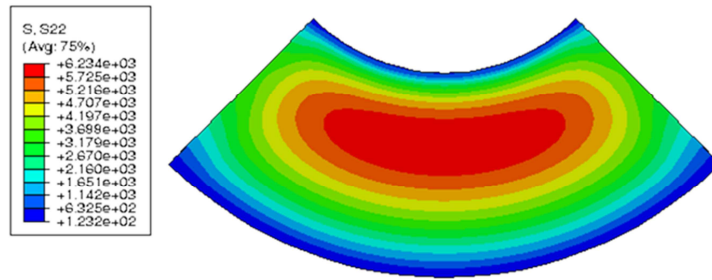


Figure 4-7 FE-based ILT stress distribution in the radius area of the curved-beam specimen at 232 lbs (1.03 kN)

Post failure CT scans of the specimens showed that the delamination cracks typically pass through the longer voids located around the mid-section of the specimens. Figure 4-8 shows typical cracks observed in failed curved-beam specimen, suggesting that failure could be related to the presence of an individual critical void in the radius area.

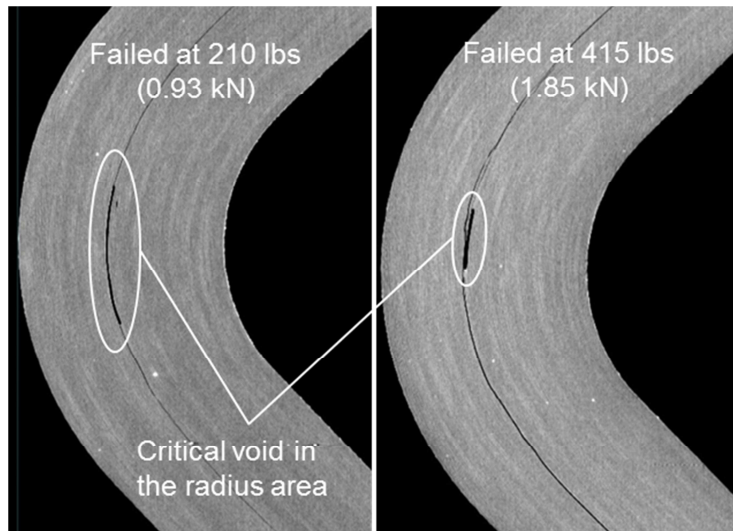


Figure 4-8 Delamination crack passing through critical voids in the radius area of the curved-beam specimens

The total porosity volume was calculated from the CT data. Laminate thickness-based  $0.26 \times 0.26 \times 0.26$  in. ( $6.6 \times 6.6 \times 6.6$  mm) cube volumes throughout the curved-beam area were considered, resulting in porosity content of less than 0.12%. This value is very small compared to aerospace industry standards, where a 2% porosity volume is commonly used as a manufacturing quality threshold for part rejection. Moreover, the porosity volume alone was found to be insufficient for describing the effects of severity of voids and correlate with the large scatter found in the curved-beam ILTS test results. Indeed, a single large void present close to the mid-plane in the curved-beam radius area is worse than a few dispersed smaller voids that add up to the same total volume.

As suggested by Figure 4-8, the knock-down in failure load in the curved-beam specimens seems to be related to the size of the critical void in the radius area. Figure 4-9 shows the trend in the failure load as a function of the void area, calculated from the in-plane dimensions. The failure loads were normalized by 722 lbs (3.21 kN) corresponding to the failure load of a curved-beam specimen without porosity. To calculate the failure load in the pristine curved-beam coupon, a 16.9 ksi ILTS (116.5 kN) value was used based on the short-beam tests, as presented later in section 4.4.3.

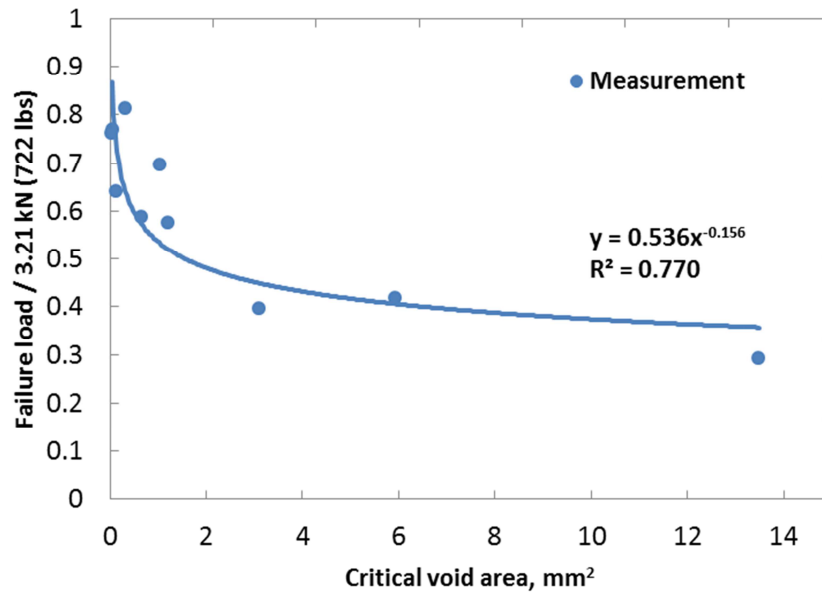


Figure 4-9 Dependency of curved-beam failure load on the area of the critical void

Data suggests that the failure load decreases proportionally to the negative power of the void area. A 0.01 in<sup>2</sup> (6.45 mm<sup>2</sup>) void present in the critical area results in almost 60% knock-down in the failure load according to the trend information. It is worth noting that the locations of the critical voids in the radius area of curved-beam specimens vary in the thickness and hoop directions. The interlaminar tensile stress distribution in a curved-beam coupon is non-uniform, as shown in Figure 4-7, therefore the location of the critical void also has an impact on the failure load and explains scatter in the data presented in Figure 4-9.

#### 4.3.3 Interlaminar Tensile Fatigue S-N Curve

Twenty 36-ply thick IM7/8552 unidirectional curved-beam specimens were manufactured per ASTM D 6415 specifications, as described previously. The specimens were cut from the same panel than the ten coupons used for the ILTS tests presented in section 4.3.2. The ASTM d 6415 test fixture shown in Figure 4-6 was subjected to cyclic loads at 0.1 load ratio and 5 Hz frequency, to delamination failure of the specimens.

Based on monitoring the curved-beam specimens during fatigue tests, delaminations initiating in the curved-beam radius area immediately propagated into the flanges at extremely fast rate, i.e., there was no stable fatigue growth period. Visual monitoring during the fatigue tests was supplemented with a stereo camera system automatically taking images of curved-beam lateral surfaces at peak loads at the specified time-intervals ranging from 1 s. to 1 min. A continuous analog output from the load frame controller was used in the image acquisition software to capture stereo images at specified loads during fatigue tests. Although the images could be captured at 1 Hz or lower frequency, the time-delay for the individual images was of the order of a millisecond. Therefore, the images corresponding to the specified loads could be captured in the fatigue tests.

Figure 4-10 shows examples of fatigue delaminations in curved-beam specimens after fatigue tests. Similar to delaminations in the static specimens, the fatigue delaminations initiated in the radius area of the curved-beam specimens; and quickly propagated through the flanges. The locations of the delaminations were also not uniform among the specimens; and did not necessarily coincide with the location of the maximum ILT stress in the porosity-free specimen. Secondary delaminations as well as delamination branching were observed in some of the curved-beam coupons.

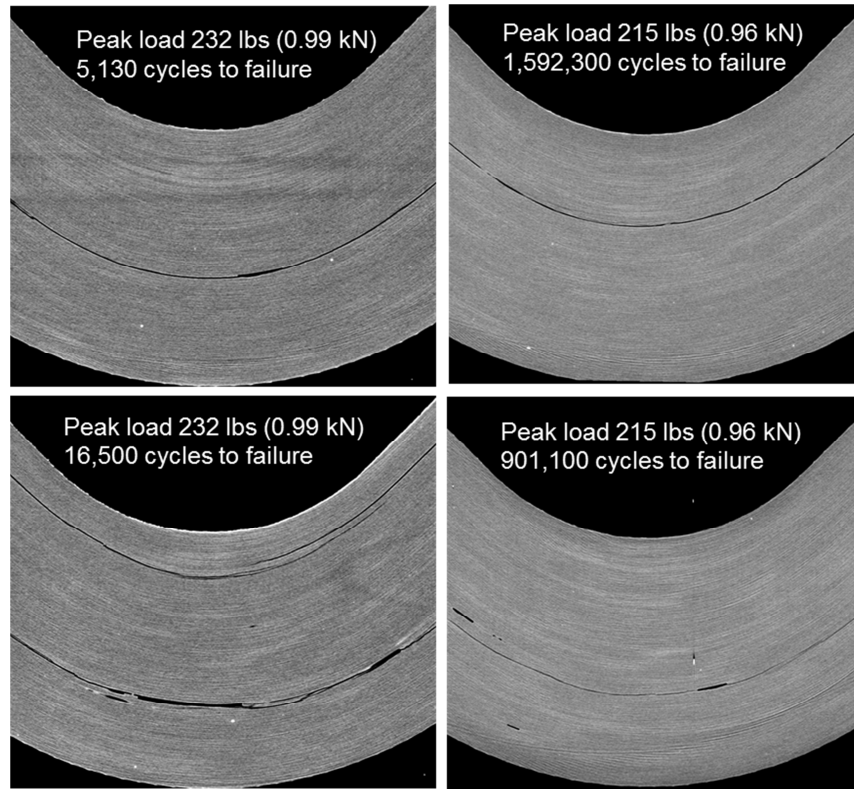


Figure 4-10 Examples of delaminations in IM7/8552 curved-beam fatigue specimens

The ILT peak stresses during fatigue testing are calculated from the closed-form ASTM D 6415 geometric ILT stress approximation given in Eq. (4.1). The deformed shape used in the stress calculation was obtained from initial monotonic loading up to the peak fatigue load value prior to the fatigue testing. The ILT S–N curve is generated by plotting the ratio of the interlaminar tensile peak stress and the interlaminar tensile strength against the log of the number of cycles to failure. The 10.5 ksi (72.4 MPa) ILT strength generated based on the 10 ASTM D 6415 curved-beam tests was used. The interlaminar tensile S–N curve and the least-squares fit for the power-law are illustrated in Figure 4-11. A large scatter with a low  $R^2$  value of 0.337 is reported.

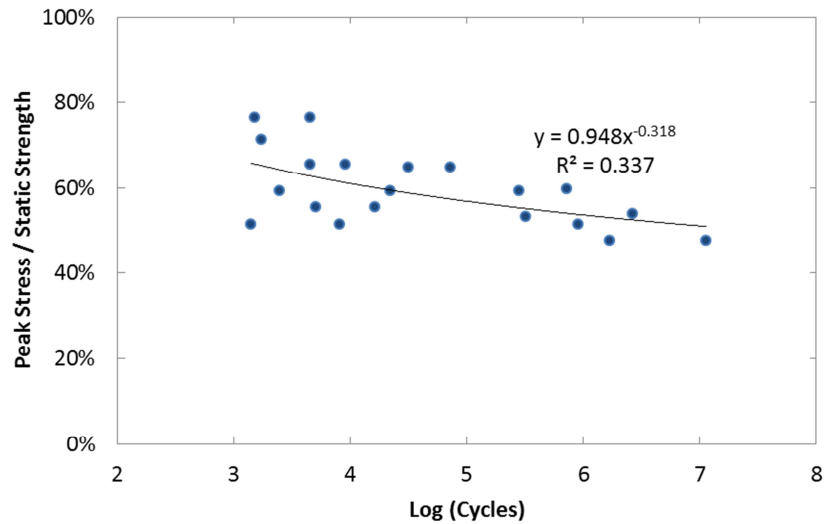


Figure 4-11 ILT S-N curve based on the ASTM D 6414 ILT stress approximation

Similarly to the observations in the static ILTS test specimens, post-failure CT scans of the specimens showed that the fatigue delamination crack typically passes through the longer voids located in the radius area of the curved-beam specimens. The presence of larger voids on the delamination path is illustrated in Figure 4-10. The total void content of the curved-beam specimens tested in fatigue was below 0.12%, as observed in the static specimens. Therefore it is not the porosity volume but the presence of individual voids at critical locations that might cause the scatter in the fatigue results presented in Figure 4-11. Ref. [72], also documents a significant correlation between the presence of a large critical individual void and fatigue life in the region of the laminate associated with the fatigue crack propagation.

## 4.4 Refinement of the Curved-beam Test Method to Account for Porosity

### 4.4.1 *Local Stress Analysis*

Post-failure CT scans showed that the ILT delamination failure in the curved-beam specimens can be related to an individual void present at the crack location. Interlaminar stress concentration develops at the edge of the critical void and initiates delamination failure. CT measurements of the critical void geometry showed that the failure loads of curved-beam specimens could be related to the in-plane area of the defects. However, as the interlaminar tensile stress distribution in a curved-beam coupon is not uniform and the location of the critical voids varies in the radial and hoop directions, the location of critical voids has also an impact on the failure load. Micro-CT inspections revealed that the voids present in the curved-beam specimens had finite radii of curvature, which prompted the application of a stress-based approach to account for the effects of defects. Figure 4-12 shows details of typical voids geometry with smooth edges not resembling sharp cracks, where a fracture mechanics based approach might be more applicable.

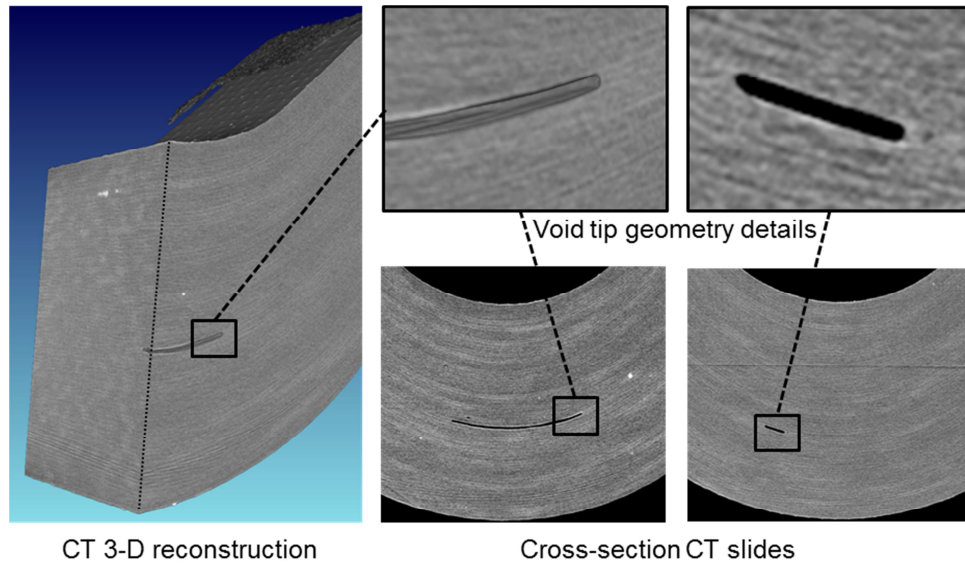


Figure 4-12 Details of the void geometry in the CT scans of curved-beam specimens

This work proposes to capture the combined effects of the void geometry and location by FE analysis of the stress concentration near the critical void. Stress-based failure prediction in the presence of large stress gradients requires inspection of stresses (or spatially averaged stresses) at a characteristic distance that could represent some gage length related to failure. The concept of using characteristic distances to determine failure of composites in the presence of stress concentrations has been proposed in [99]. The same work introduced the point-stress and average-stress failure criteria, where failure is determined by stresses at a finite characteristic distance or stresses averaged over a characteristic distance in the stress concentration region. These methods are applied to characterize the ILT stress concentrations at the failure-critical voids in the curved-beam specimens.



#### 4.4.2 Refinement of the ILTS by Integration of Defects

ABAQUS scripting capability was used to automatically transfer the CT measurements into a FE model and build a structured three-dimensional local mesh representative of the volume of composite material around the critical void. As shown in Figure 4-12, voids in the curved-beam specimens can be approximated by tri-axial ellipsoids in cylindrical coordinates and defined by the thickness and two aspect ratios in the fiber and width directions, as illustrated in Figure 4-13.

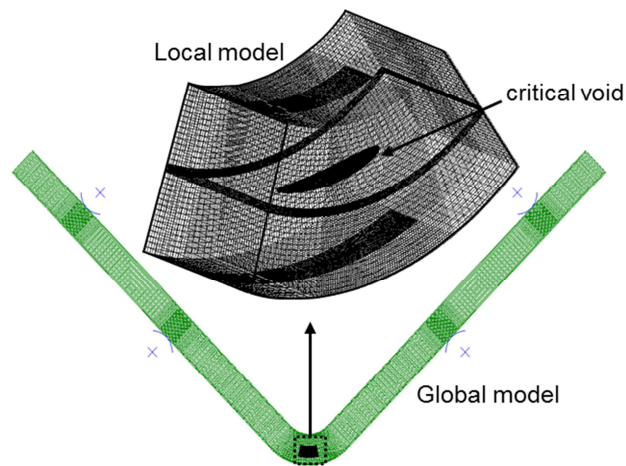


Figure 4-13 3D structured FE global mesh of a curved-beam coupon and a local submodel of the critical void

Local material orientation is assigned to follow the curvature of unidirectional plies in the radius area of the specimens. Mesh sizes around the voids were refined to  $1.5\ \mu\text{m}$  and convergence of local stresses was verified. Linear 8-noded hexagonal 3D elements with reduced integration scheme (C3D8R) from the ABAQUS element library

were used in the local models and the global model. A typical total number of degrees of freedom (DOF) for the converged local models was in the 500–800 K range.

Displacements from the global model of the curved-beam specimen at failure load were applied as boundary conditions for the six faces of the local model volume. Figure 4-13 shows the global model FE mesh including approximately 80 K eight-noded C3D8R hexagonal elements with 560 K degrees of freedom (DOF). The global FE model had 36 elements per specimen thickness while the mesh density in the radius area was refined to an overall element size of 0.1 mm. Geometric and material nonlinearities as well as contact interactions were included. Analytical rigid rollers and frictionless contact conditions were created to represent attachments of the ASTM D 6415 test fixture. The following material constitutive properties for IM7/8552 Carbon/Epoxy composite were utilized:  $E_{11} = 22.7$  msi (157 GPa);  $E_{22} = E_{33} = 1.3$  msi (8.96 GPa);  $\nu_{12} = \nu_{13} = 0.32$ ;  $\nu_{23} = 0.5$ ;  $G_{12} = G_{13} = 0.737$  msi (5.08 GPa); and  $G_{23} = 0.433$  msi (2.99 GPa).

ILT as well as interlaminar shear (ILS) stress concentrations develop at the edges of the tri-axial ellipsoid that defines the critical void. Numerical results for typical void geometries include ILT stress concentration factors ranging between 8 and 20, which is consistent with closed-form solutions provided by Chiang in [100] for a tri-axial ellipsoidal cavity in an infinite isotropic elastic body. The ILT stress concentration and the quick decay of ILT stress with the distance from the void is illustrated in Figure 4-14.

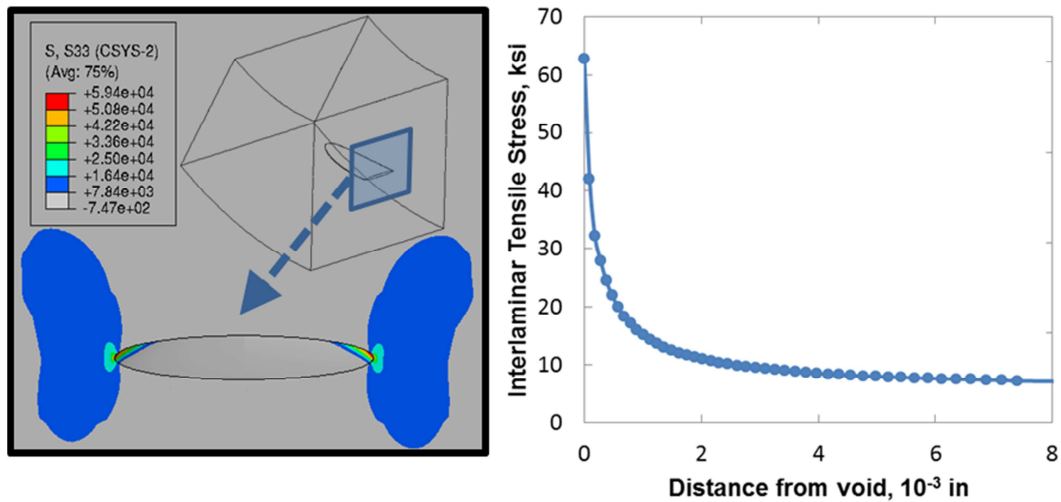


Figure 4-14 ILT stress concentration at the edges of the critical void (left) and decrease of ILT stress versus the radial distance from the void surface (right)

The ILT and ILS stress concentrations are spatially out of phase, with maximum ILS stress found at the tip of the void and maximum ILT stress found at about mid-length of the void, around the location of the maximum width, as shown in Figure 4-15. Local stress analysis results for all curved-beam specimens also demonstrated that the maximum interlaminar shear stresses at the void surface were much lower than the maximum interlaminar tensile stresses. As a consequence, the failure mode in presence of porosity defects can be identified as a predominantly tensile delamination. Post-failure CT scans of the specimens confirmed that delamination initiates at a location close to the maximum width location, where the largest ILT stress is found.

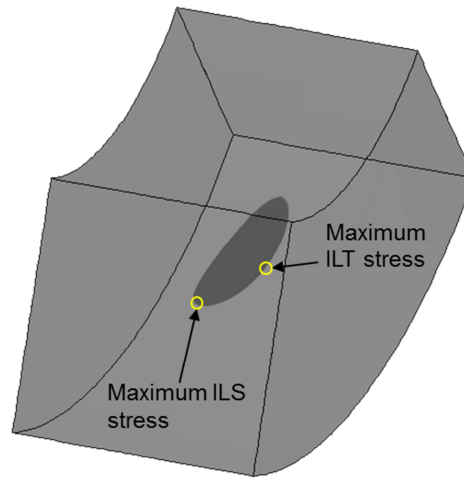


Figure 4-15 Location of the maximum ILT stress and the maximum interlaminar shear (ILS) stress at the surface of the critical void

Point-stress and average-stress methods rely on the calibration of the characteristic distance, which is usually determined through static tests of representative specimens loaded to failure. The characteristic distance is usually determined as the distance at which the stress (or spatially-averaged stress) obtained from closed-form solution or FE analysis at failure load is equal to the material strength [99]. The material strength and failure loads are known, and the characteristic distance obtained by averaging the results for a representative number of test specimens.

In the methodology proposed in this work, characteristic distance and strength can be both determined at the same time, from FE analysis of the stress concentration at the critical void under the known failure load from the ILTS tests. No calibration or a-priori knowledge of characteristic distances is required.

For each of the 10 curved-beam specimens tested, critical voids were detected and CT data transferred into a local FE model. The failure load measured from static test was applied to the global model to determine the displacement boundary conditions of

the local FEM model. In the point-stress method, the local FE model based ILT stresses are plotted for each specimen as a function of the distance from the void in the radial direction, as shown in Figure 4-16. In the average-stress method, the spatial average of the ILT stresses was considered. The average stress is calculated as:

$$\sigma_{av} = \frac{1}{x} \int_0^x \sigma(r) dr \quad (4.5)$$

Where  $x$  is the distance to the void surface and  $\sigma$  is the ILT stress.

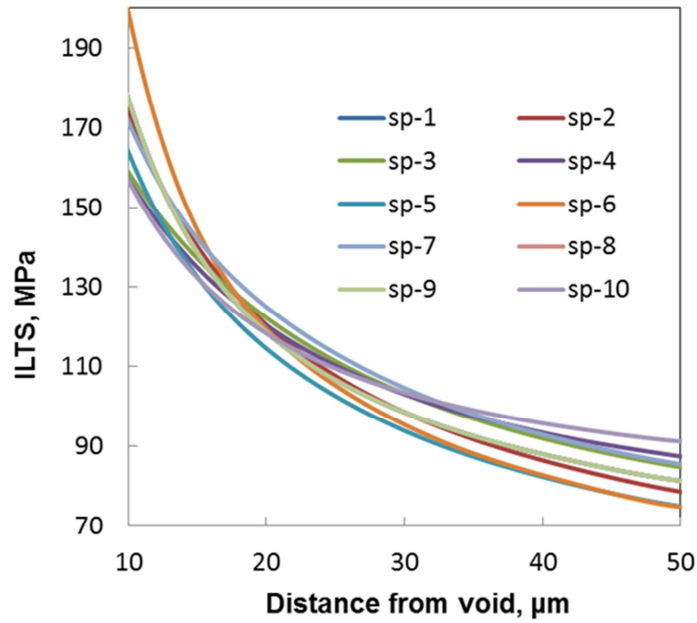


Figure 4-16 ILT stresses as a function of the distance from the critical void for the ten IM7/8552 curved-beam specimens for the point-stress method

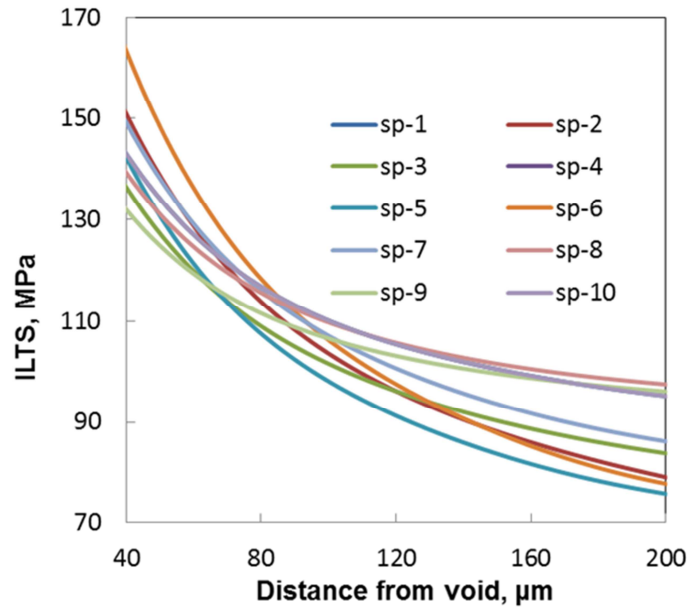


Figure 4-17 ILT stresses as a function of the distance from the critical void for the ten IM7/8552 curved-beam specimens for the average-stress method

At each distance, the coefficient of variation (COV) of the point-stress and the average-stress data were also plotted. By examination of the COV dependence on the distance from the void, a unique and distinctive minimum point was identified as illustrated in Figure 4-18 and Figure 4-19 for the point-stress and average-stress methods, respectively. The distance corresponding to the minimum COV for the entire population of the static curved-beam specimens tested was defined as the optimum characteristic distance, and that distance has been used to determine the refined interlaminar tensile strength value. A characteristic distance of  $7.3 \times 10^{-4}$  in. ( $19 \mu\text{m}$ ) was reported for the point-stress method and  $3.5 \times 10^{-3}$  in. ( $89 \mu\text{m}$ ) for the average-stress method. The average ILT stress among the specimens at the minimum COV point also gives the ILTS value. Results for the ten curved-beam specimens are summarized in

Table 4-2 and compared to the stresses calculated using ASTM D 6415 presented in section 4.3.2. An average ILT strength of 18.0 ksi (124.3 MPa) and 2.1% COV were determined for the point-stress method; and 16.0 ksi (110.4 MPa) with 3.2% COV for the average-stress method. It should be noted that the strength obtained with both methods are significantly higher than the 10.5 ksi (72.5 MPa) ILTS generated from the ASTM D 6415 and show much lower scatter (26.5% COV was found for ASTM D 6415 results).

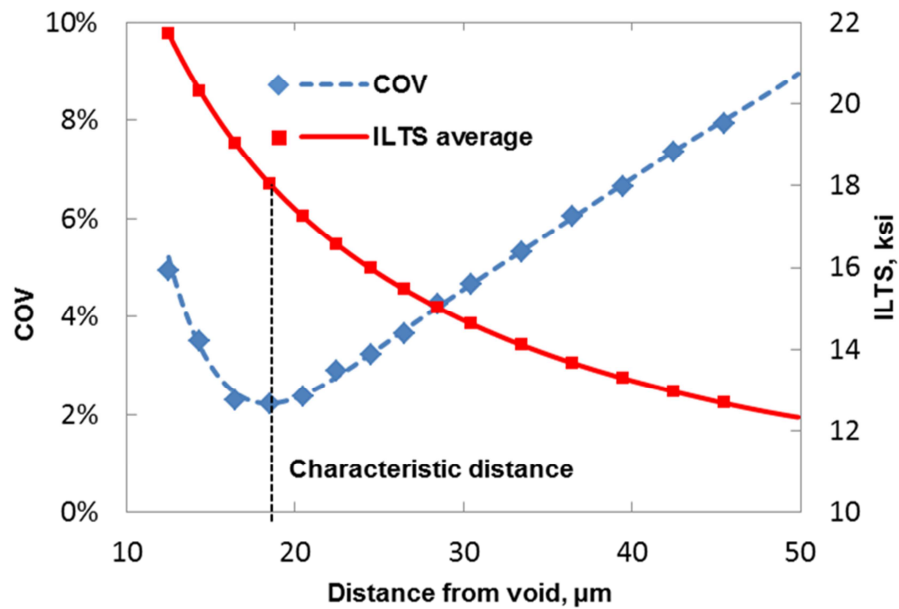


Figure 4-18 Average ILT strength (ILTS) and COV as a function of radial distance from the void surface in the point-stress method

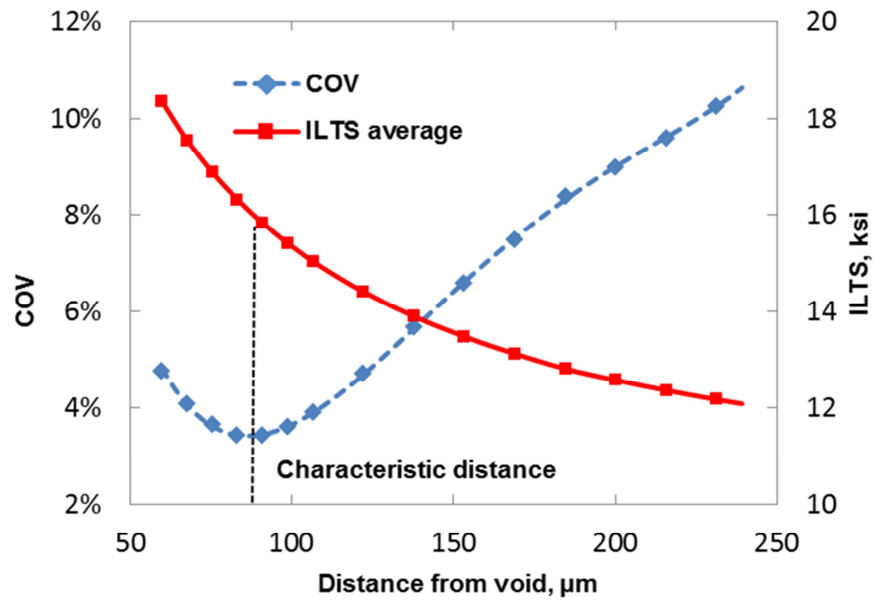


Figure 4-19 Average ILT strength (ILTS) and COV as a function of radial distance from the void surface in the average-stress method

Table 4-2 ASTM D 6415 and refined ILTS for curved-beam specimens with porosity defects

Specimen	ASTM D 6415 ILTS, MPa (ksi)	Refined ILTS point-stress, MPa (ksi)	Refined ILTS average-stress, MPa (ksi)
1	83.4 (12.1)	123.1 (17.9)	115.1 (16.7)
2	52.3 (7.6)	125.1 (18.1)	109.3 (15.8)
3	70.3 (10.2)	125.8 (18.2)	105.7 (15.3)
4	92.8 (13.5)	123.8 (18.0)	109.1 (15.8)
5	50.0 (7.3)	119.0 (17.3)	103.3 (15.0)
6	37.7 (5.5)	125.2 (18.2)	112.9 (16.4)
7	68.8 (10.0)	129.3 (18.7)	112.0 (16.2)
8	94.6 (13.7)	125.8 (18.2)	113.0 (16.4)
9	93.9 (13.6)	123.9 (18.0)	109.3 (15.9)
10	81.5 (11.8)	121.5 (17.6)	113.8 (16.5)
<b>Average</b>	<b>72.5 (10.5)</b>	<b>124.3 (18.0)</b>	<b>110.4 (16.0)</b>
<b>CV</b>	<b>26.5%</b>	<b>2.1%</b>	<b>3.2%</b>



#### 4.4.3 Comparison with ILT Short-Beam Test

Short-beam tests were used as an alternative method to measure the ILT strength and compare with results obtained by integration of the defects in the refinement of the ASTM D 6415 curved beam ILTS. Short-beam specimens are prismatic coupons with uniform rectangular cross sections, easy to manufacture and typically do not include porosity defects. The ILT short-beam test is a derivative of the short-beam test methodology proposed by Makeev et al. in [3] to measure multiple material properties based on DIC full field strain measurements.

Figure 4-20 shows a typical short-beam test setup; schematic of the short-beam specimen configurations; and an example of DIC-based strain assessment. A unidirectional tape panel can be utilized to machine the short-beam coupons in the zero-degree and 90-degree material directions; and apply loading in the 1-2 (in-ply), 1-3 (interlaminar), and 2-3 (interlaminar) principal material planes to characterize multiple basic constitutive relations for a composite material. For reference, the fiber direction is denoted as 1 (zero-degree); the in-ply transverse direction as 2 (90-degree); and the laminate thickness direction as 3 (the interlaminar principal material direction). The failure mode of a short-beam specimen varies depending on the fiber direction, support length-to-thickness ratio, and loading nose/support diameter. Figure 4-21 shows examples of representative failure modes.

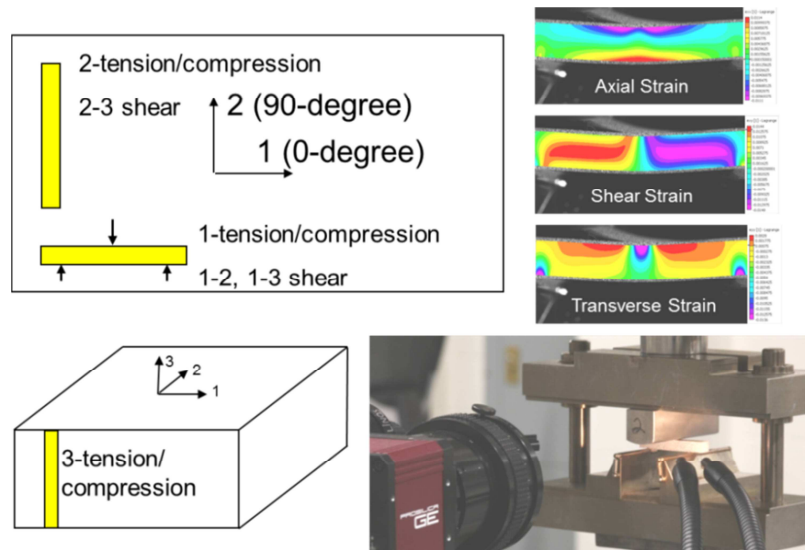


Figure 4-20 A short-beam method to measure multiple stress-strain properties of composites: specimen configurations, test setup, and measured strains (DIC)

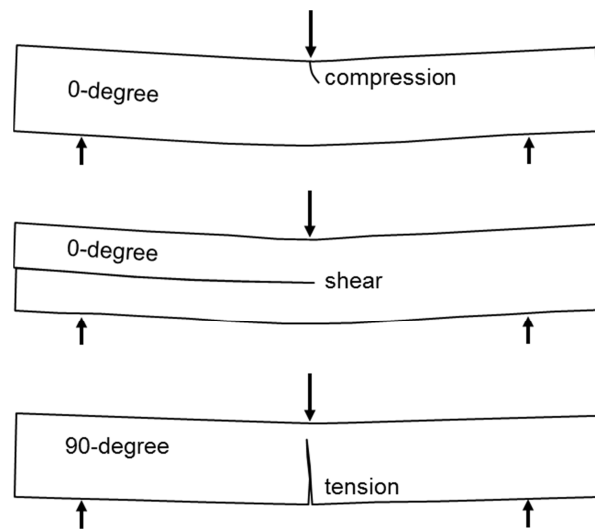


Figure 4-21 Failure modes of short-beam specimens

To assess the ILTS, six short-beam specimens were machined in the thickness direction from a 106-ply thick IM7/8552 carbon/epoxy unidirectional tape panel cured at 350 degrees F per prepreg manufacturer's specifications. The coupons used were 3.8 mm (0.15 in) thick, 2.8 mm (0.11 in) wide and 19.4 mm (0.76 in) long. The coupon thickness corresponds to the 90-degree principal material direction; and the 2-3 material plane was the plane of loading. The specimens were placed in an ASTM D 2344 test fixture with a 0.5-inch diameter loading nose and 0.125-inch diameter supports; and loaded in an electromechanical load frame at a constant 0.05 in/min crosshead displacement rate till failure. The support length was 0.59 inches. All short-beam specimens failed in tension in the middle of the specimen, as shown in Figure 4-21 for 90-degrees coupons. The average failure load value was 47 lbs (209 N), which was too low to introduce any compressive damage under the loading nose or near the lower support locations.

All coupons exhibited linear through-the-thickness axial strain distribution throughout the coupons, including the center cross section corresponding to the failure location. As suggested in 155[3], such observations can be used to derive a simple beam closed-form approximation for the maximum axial normal stress in the short-beam coupon:

$$\sigma_{33} = \frac{My}{I} \text{ with } M = \frac{PL}{4} \quad y = \frac{H}{2} \quad I = \frac{WH^3}{12} \quad (4.6)$$

Where P is the applied force, L is the support length, and H and W are coupon thickness and width. Eq. (4.6) applied to the short-beam coupons tested in this work yields a 115.1 MPa (16.7 ksi) (COV 3%) approximation for the interlaminar tensile strength.

To verify the accuracy of the closed-form ILT stress approximation, a linear three-dimensional finite element model was built in the ABAQUS commercial finite

element analysis code. The average failure load value, the short-beam specimen dimensions as well as the attachment locations and sizes are listed earlier in this section. The finite element model accurately simulated the loading nose and the supports. The following material constitutive properties were utilized<sup>14</sup>:  $E_{11} = 22.7$  Msi (157 GPa);  $E_{22} = E_{33} = 1.3$  Msi (8.96 GPa);  $\nu_{12} = \nu_{13} = 0.32$ ;  $\nu_{23} = 0.5$ ;  $G_{12} = G_{13} = 0.737$  Msi (5.08 GPa); and  $G_{23} = 0.433$  Msi (2.99 GPa). Details of the finite element mesh can be found in [79]. The finite element analysis resulted in a 16.9 ksi (116.5 MPa) interlaminar tensile strength value which was similar to the 16.7 ksi (115.1 MPa) closed-form beam approximation (4.6).

The 16.9 ksi (116.5 MPa) ILTS obtained from the ILT short beam test is in good agreement with the 18.0 ksi (124.3 MPa) (2.1% COV) and 16.0 ksi (110.4 MPa) (3.2% COV) ILTS values found respectively with the refined point-stress and average-stress method for the curved-beam specimens. It should be noted that a flat laminate used to manufacture short-beam specimens is not as prone to porosity as a curved laminate. Therefore, the low scatter in the refined curved-beam ILTS results and the good agreement with the ILT short-beam strength show that the methodology presented in section 4.4.2 enables the integration of the effects of the defects in the assessment of the ILT performance and suggests that the ILTS obtained is appropriate as pristine (defect-free) material property.

#### *4.4.4 Application to ILT Fatigue Behavior*

The defect analysis methodology presented in section 4.4.2 was applied to refine the ILT S–N curve obtained from the ASTM D 6415 approximation of the peak ILT stress for the 20 CB specimens tested in fatigue. For each of the specimen, critical voids in the radius area were detected and measured as presented in section 4.2. Void measurements were transferred into local FE sub-models. Displacement boundary conditions in the local FE models were generated from the global FE models of the curved-beam specimens subject to the peak fatigue loads.

For the point-stress method, the defect-free peak stresses were determined by using the ILT stresses computed from the FE analysis at the  $7.3 \times 10^{-4}$  in. (19  $\mu\text{m}$ ) characteristic distance from the void's surface, as defined in section 4.4.2. In the average-stress method, the ILT stresses were averaged over the  $3.5 \times 10^{-3}$  in. (89  $\mu\text{m}$ ) characteristic distance. The ILT stresses at the peak fatigue loads were normalized by the corresponding ILT strength; and plotted against the log of the number of cycles to failure to generate the ILT S–N curves. The ILT strength values used for normalization were 18.0 ksi (124.3 MPa) for the point-stress method and 16.0 ksi (110.4 MPa) for the average-stress method, as listed in Table 4-2.

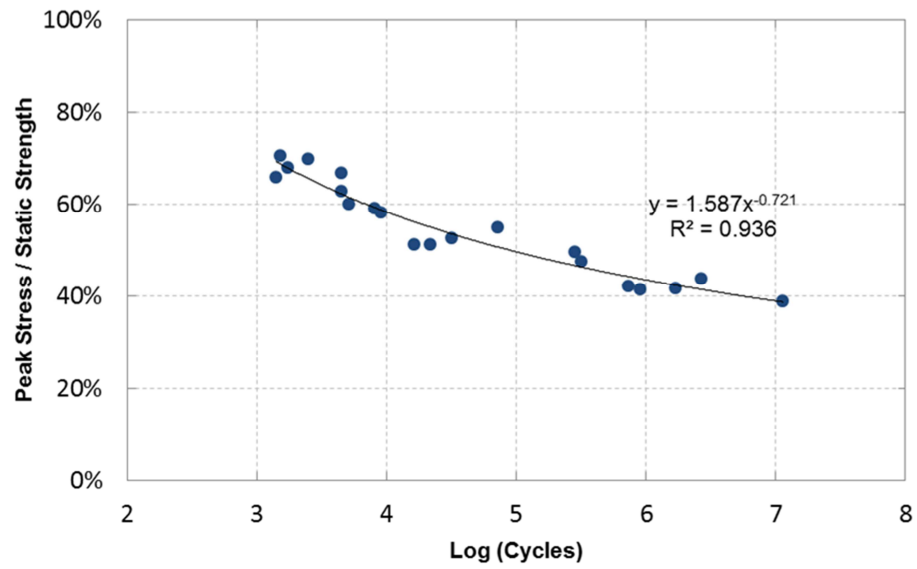


Figure 4-22 Refined ILT S-N curve based on the point-stress method (19  $\mu\text{m}$  characteristic distance)

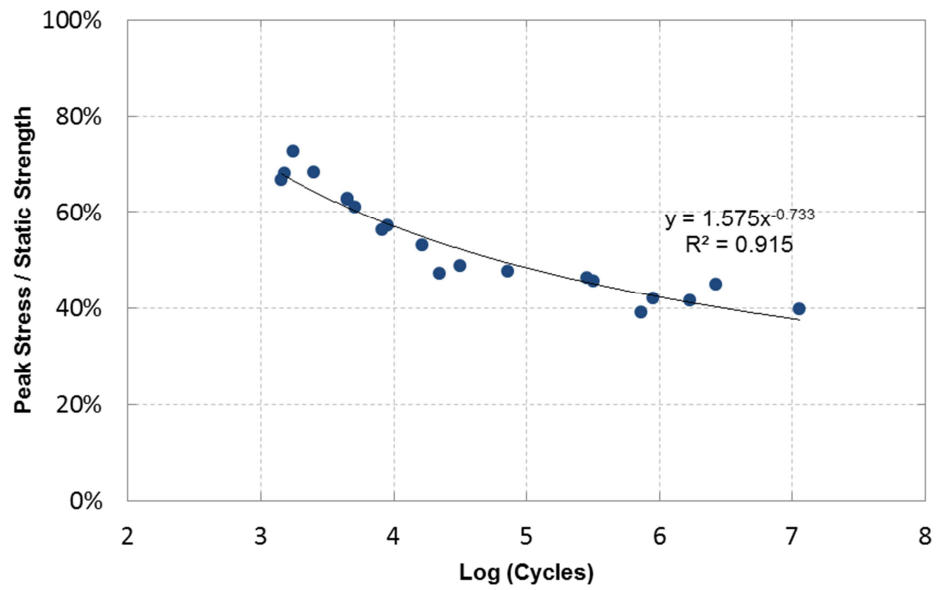


Figure 4-23 Refined ILT S-N curve based on the average-stress method (19  $\mu\text{m}$  characteristic distance)

The ILT S–N curves from both methods are presented in Figure 4-22 and Figure 4-23. The figures list the power law coefficients calculated based on a least-squares fit of the test data. Both S–N curves are similar, with less than 2% relative difference in the exponent. The refined exponent more than doubles the exponent of the fatigue curve based on the ASTM D 6415 ILT stress approximation. A 0.92  $R^2$  value corresponding to the point-stress method and  $R^2 = 0.94$  to the average-stress method are much stronger compared to the  $R^2 = 0.34$  from the ASTM D 6415 ILT stress approximation. The improved correlation coefficients and consistency of the refined ILT S–N curves look promising to using the refined fatigue curves as a pristine (porosity-free) material property. The reduced scatter supports the ability of the refined ILT stress analysis methods to capture the effect of porosity on the ILT fatigue performance.

## Chapter 5

### Transition to the Structural Scale

This chapter presents the results of a feasibility assessment targeting the scaling of knowledge and methods acquired at the material scale, to larger structural composite elements. In Chapter 3, the ability to predict strength and fatigue failure in coupon-scale OHT and OHC specimens was demonstrated. Successful failure predictions increased the confidence in the development of virtual test methods replacing some of the standard tests of multidirectional laminated composite materials with three-dimensional models accurately predicting deformation, damage topography, strength, and cycles to failure. Chapter 4 introduced a methodology for prediction of strength and fatigue behavior in curved-beam specimens including porosity defects, showing that the development of a method to capture the effects of manufacturing defects at the material scale using high-fidelity nondestructive inspection techniques also seems to be on the right track. However, the remaining key questions are related to the ability of transitioning the methodology developed at the material scale to larger composite structures. Structures might have phenomena not encountered in smaller coupons, and therefore transition of material information might be challenging. In particular, manufacturing defects such as ply-waviness and large porosity/voids can be prominent in Carbon/Epoxy and Glass/Epoxy thick laminates used for rotorcraft flight-critical structural components, and require integration of their effects in the failure prediction methodology.



## 5.1 Structural Test Articles

A three-point bend flapping element is selected as a representative structural component found in composite rotorcraft structures. The flapping element is about 22 in. (56 cm) long and includes 5 structural holes for bolted connection with the test fixture, as shown in Figure 5-1. Flapping specimens were manufactured from thick S2-glass/8552-epoxy and IM7-carbon/8552-epoxy laminated flat panels.  $\frac{3}{4}$  in. (19 mm) thick 84-ply symmetric  $[(\pm 45)_2/0_4]_5/45/-45]_s$  layup was used in the Glass/Epoxy specimens and  $\frac{1}{2}$  in. (12.7 mm) thick 68-ply symmetric  $[(\pm 45)_2/0_4]_4/45/-45]_s$  layup was used in the Carbon/Epoxy specimens. Porosity voids representative of structural-scale manufacturing defects were intentionally introduced at critical locations.

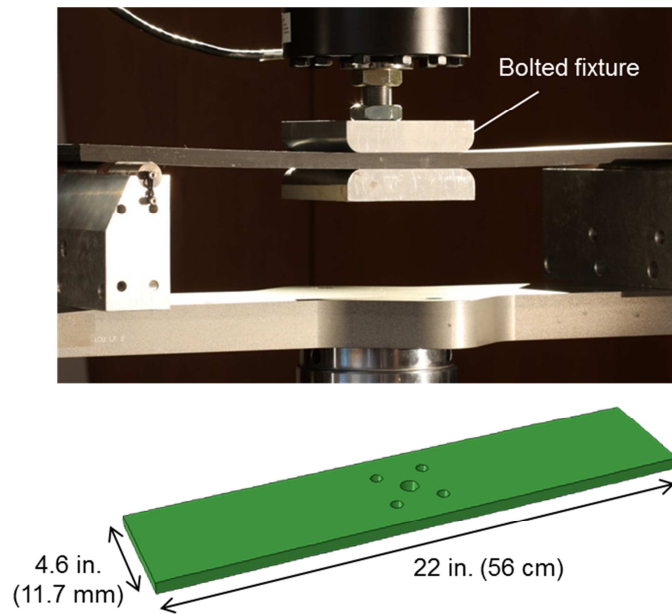


Figure 5-1 Flapping element in a three-point bend test setup with bolted fixture (top) and geometry details (bottom)

The specimens were loaded quasi-statically in bending using an servo-hydraulic load frame at a constant 0.05 in./min. crosshead displacement rate till failure. Fatigue tests were also conducted with a  $R=0.1$  load ratio and 1.5 Hz frequency. A random speckle pattern was applied to the surface of the specimens using black and white spray paint for strain monitoring using the DIC technique with a 16-megapixel stereo camera system. All static and fatigue specimens failed in delamination failure with unstable growth of a delamination crack initiating under the bolted fixture. Figure 5-2 shows a delamination crack in the flapping specimen identified by DIC observation of the interlaminar shear surface strain field. It is worth noting that the locations of the delamination crack were not uniform among the specimens; delaminations were observed under the right or left side of the test fixture and for different locations along the thickness direction.

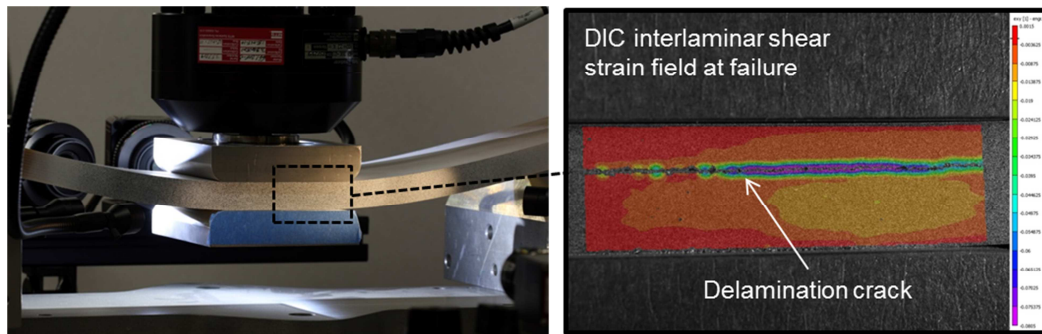


Figure 5-2 Flapping element under bending loading with surface spray-painted for DIC strain measurements (left) and DIC interlaminar shear strain field showing delamination crack at failure load (right)

## 5.2 Measurements of Defects

Manufacturing porosity defects were intentionally introduced in some of the flapping elements. To capture volumetric porosity/void data, all specimens have been CT-scanned and their volumes reconstructed using the 225 kV micro-focus X-Ray Computed Tomography system manufactured by North Star Imaging before structural tests were completed.

CT scans of the approximately 5 x 5 in. (12.7 x 12.7 cm) clamped area under the bolted fixture of Glass/Epoxy flapping specimens were completed at 210 kV tube voltage, 300  $\mu$ A target current and the speed of 2.8 frames per second (fps) while averaging 6 frames per angle increment and using 0.06 in. (1.5 mm) copper filter on the tube. The radiographs were taken at each  $\frac{1}{4}$  of a degree resulting in 1440 radiographs for the full rotation, to allow full X-Ray penetration through the specimens and maximize contrast in the reconstruction. Geometric magnification of the scan was 2X and the 3D reconstruction of the specimen had pixel resolution of approximately  $2.5 \times 10^{-3}$  in. (64  $\mu$ m). Carbon/Epoxy flapping specimens were scanned at 140 kV, 400  $\mu$ A, 2.5 fps speed and 0.03 in. (0.76 mm) copper filter, at the same pixel resolution.

The volume reconstruction of a CT scan is a volumetric point cloud where each point (or voxel) contains “gray values” that ranges from 0 to 65536 and approximately represents the material density at a point. The through-the-thickness sections of the 3D volume were used for identifying void shapes, sizes and locations in the specimens, and for calculation of porosity volume distribution. The density-based contouring method introduced in [97] and presented in section 4.2 is used to separate material from voids and identify void boundaries. Figure 5-3 and Figure 5-4 show examples of the scans for Glass/Epoxy and Carbon/Epoxy specimen sectioned in the middle of the specimen

thickness. The figures demonstrate seeded voids and porosity visible in the clamped area scans.

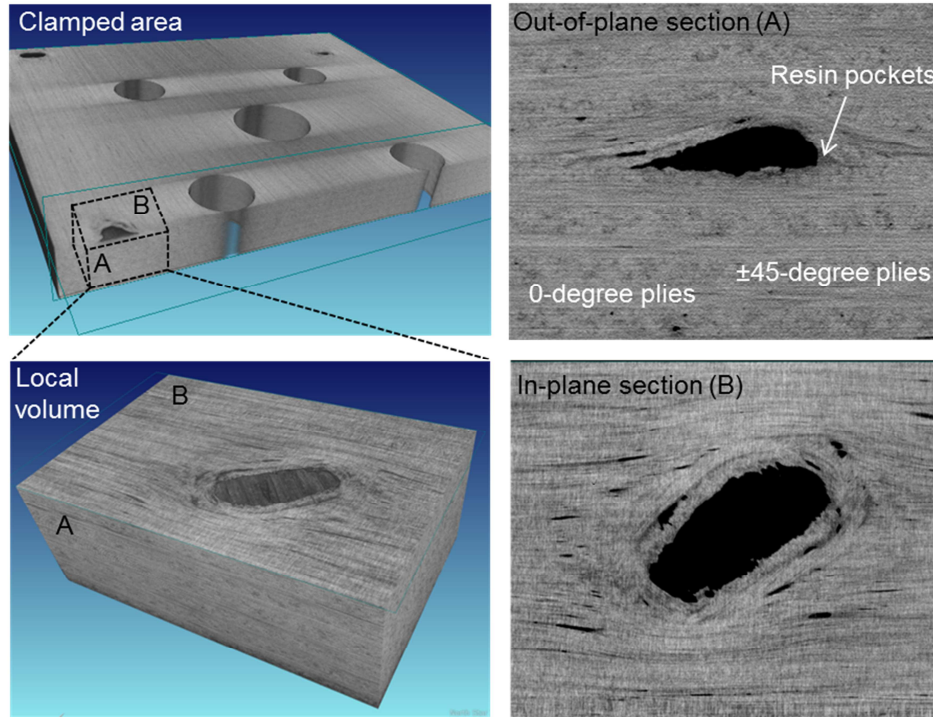


Figure 5-3 CT scan details in S2/8552 Glass/Epoxy flapping element showing out-of-plane (top right) and in-plane (bottom right) fiber waviness around a seeded void defect

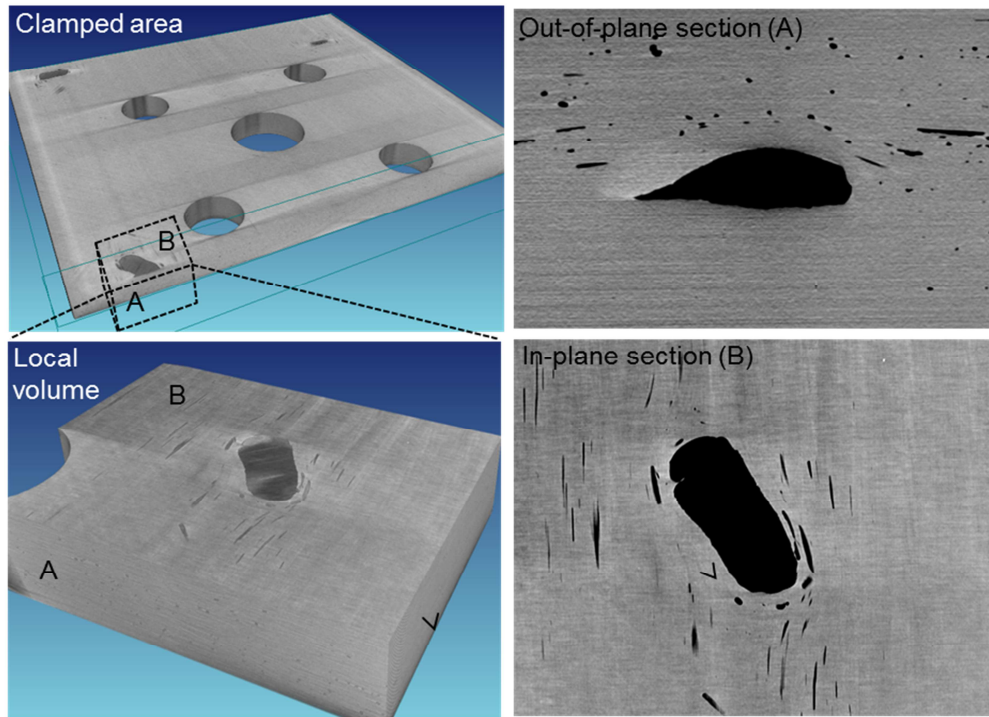


Figure 5-4 CT scan details in IM7/8552 Carbon/Epoxy flapping element showing out-of-plane (top right) and in-plane (bottom right) fiber waviness around a seeded void defect

It is worth noting that the pixel resolution of  $2.5 \times 10^{-3}$  in. ( $64 \mu\text{m}$ ) obtained in the scans of the 5 x 5 in. (12.7 x 12.7 cm) clamped area of the specimen was not sufficient for resolving the local geometry of the piles around the seeded defects. In order to improve the CT scan resolution and enable local structural analysis in the areas of seeded voids, local scans have been accomplished. The local scans of void areas were completed at 150 kV tube voltage, 160  $\mu\text{A}$  target current, 0.65 fps speed, 4 frame-averaging and 0.03 in. (0.76 mm) copper filter for the Glass/Epoxy specimens; and at 70 kV, 360  $\mu\text{A}$ , 3.5 fps, 10 frame-averaging and 2x2 pixel binning for the Carbon/Epoxy specimens. The scans were done at 10X geometric magnification and had a pixel resolution of about  $0.5 \times 10^{-3}$  in. ( $12.7 \mu\text{m}$ ), approximately 5 times smaller than the

clamped area scans. Figure 5-3 and Figure 5-4 demonstrate vastly improved level of detail in the local scans that allows clear identification of the ply-scale features and geometric topography around the seeded voids. Voids identified in Figure 5-3 and Figure 5-4 typically span multiple plies, leading to significant in-plane and out of-plane fiber waviness. In addition to ply waviness the local scans in the out-of-plane direction show resin pockets around voids: darker areas for Glass/Epoxy specimens and lighter areas for Carbon/Epoxy specimen, which is due to glass fibers being denser than resin and resin denser than carbon fibers. Resin pockets and occasional porosity/voids are typical between the glass fiber bundles in Glass/Epoxy sections in Figure 5-3.

Porosity/voids are more common in the Carbon/Epoxy composite, as shown in Figure 5-4, which also demonstrates that porosity is not uniformly distributed in the specimen. Distribution of porosity volume through the specimen thickness was determined for Carbon/Epoxy composite flapping elements based on their CT scans. All through-the-thickness section images (corresponding to  $2.5 \times 10^{-3}$  inch thick slices) were analyzed by the porosity detection software to find porosity in the sections. Maximum section porosity in the specimen was found to reach 2% while the average volumetric porosity was around 0.5%. These measurements were used to select specimen orientation during the test such that the upper (under longitudinal compression) section of the specimen has less porosity to minimize developments of potential delaminations due to defected plies.

### 5.3 Methodology for Failure Predictions

#### 5.3.1 Principle

The methodology for failure predictions in the structural flapping elements follows the principles of the FE-based approach developed at the material scale in the previous chapters. Three-dimensional finite element models at the ply scale level are used for stress analysis. A constitutive model using material properties and failure allowables for S2-glass/8552-epoxy and IM7-glass/8552-epoxy is used. The constitutive model includes non-linear shear stress-strain behavior in both longitudinal and transverse directions and is implemented in a user subroutine UMAT, as presented in section 2.2.2.1. Initiation of matrix-dominated failure by delamination is identified using the stress-based mixed-mode modified LaRC04 failure criterion for delamination, as given in Eq. (2.24). Material *S-N* curves are used to adjust the strength values in the LaRC04 and solve for the number of cycles to failure for fatigue predictions. As mentioned previously, static and fatigue delaminations occurred instantaneously with unstable crack growth after failure initiation. Therefore, no damage propagation scheme for crack growth is included in the failure prediction methodology.

Both a global and local approach is used for failure predictions. A global FE model of the flapping specimens is used to identify stress concentrations and predict failure assuming pristine (defect-free) conditions in the specimens where no seeded manufacturing defects were introduced. Stress calculation is improved by using the interlaminar stress recovery procedure introduced in section 2.4. The global model is also used for displacement boundary conditions for the FE models used in the local analysis. The local analysis is used for failure prediction in flapping specimens where seeded voids

have been incorporated. Defect locations and sizes obtained from CT scans are automatically extracted and transferred to build a local three-dimensional FE model of the laminate volume around the defects. Local failure predictions are based on the accurate modeling of stress concentration due to the detected void shape and ply waviness around the voids.

### *5.3.2 Global Model*

The global FE model used in simulations typically includes linear 8-noded reduced integration elements (C3D8R) and one element per ply in the thickness direction and. Figure 5-5 shows the global FE mesh used for the 68-ply  $[(\pm 45)_2/0_4]_{4/45/-45}$   $\frac{1}{2}$  in. (12.7 mm) thick IM7-carbon/8552-epoxy flapping laminate, including approximately 190,000 elements and 900,000 DOF. Frictionless contact is defined between the specimen and the 0.75 in. (19 mm)-diameter support rollers modeled as analytical surfaces. Contact interactions are also assigned between the specimen and the rigid surfaces used to represent the bolted fixture on both sides of the specimen. Material behavior, including shear non-linearity in the interlaminar and transverse planes, is defined in the user subroutine UMAT as introduced previously.



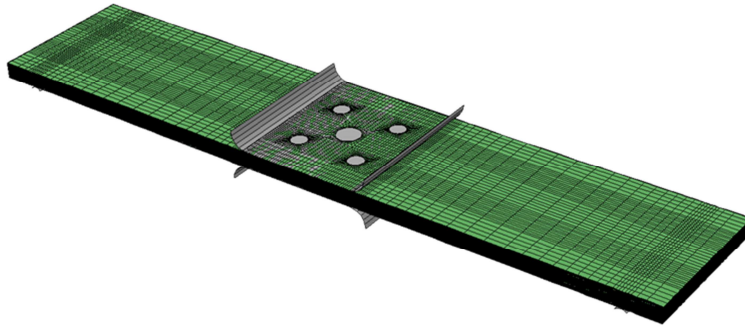


Figure 5-5 Global FE model of the flapping specimen

The analysis is completed in two steps. First, a prescribed uniform displacement is applied to the top part of the bolted fixture to simulate the compression of the specimen during tightening of the 4 assembly bolts. The displacement is defined such as the applied compressive strain is equal to 150 micro-strains, which corresponds to the average deformation obtained from the DIC strain measurements after tightening of the bolts under the nominal torque. Second, the bending load is applied to the support rollers, while fixed displacement boundary conditions are maintained for the rigid analytical surfaces representing the bolted fixture.

Prediction of failure initiation is based on the modified stress-based LaRC04 failure criterion (see Eq. (2.24)). The global model analysis is used to identify failure in the specimens without defects and to determine the displacement boundary conditions for the local FE models of the defects. Global response is validated with tests to ensure that accurate deformations and structural properties are captured by the global FE model. Figure 5-6 shows comparison of the global load-displacement curve between FEM and test results for a Glass/Epoxy flapping specimen loaded to 1200 lbs (5.34 kN). Figure 5-7 compares the global interlaminar shear strain field at the surface of the Glass/Epoxy specimen for FE-based simulations and DIC measurements. Excellent correlation

between FE global response and test results is documented; similar results were found for the Carbon/Epoxy flapping elements.

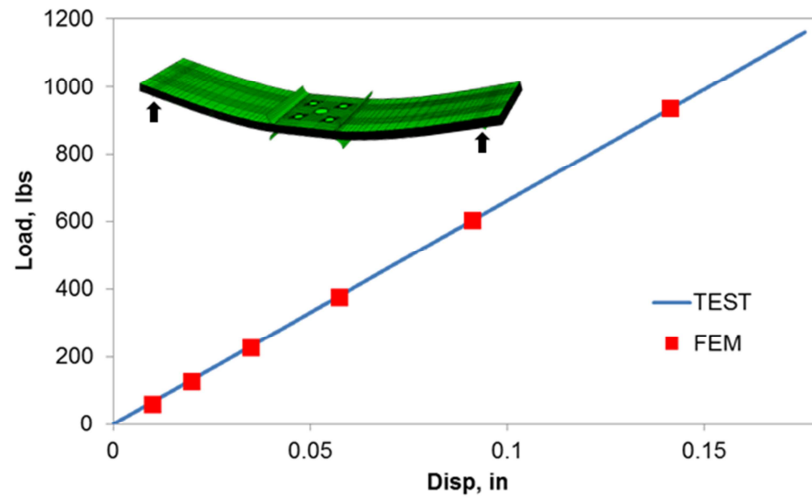


Figure 5-6 Comparison of FE-based global load-displacement response with test results for Glass/Epoxy flapping specimens

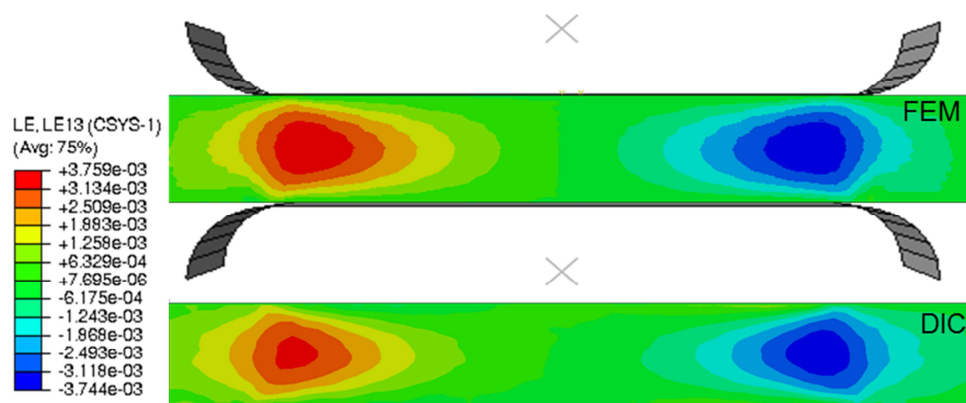


Figure 5-7 Comparison of FE-based and DIC test measurements for global interlaminar surface shear strain field in Glass/Epoxy flapping specimens at 1350 lbs (6.0 kN)

### 5.3.3 Local Model

A local model enables more detailed representation of the critical void geometry with appropriate mesh refinements for stress calculations. Void geometries are obtained with high degree of confidence from the CT measurements of two perpendicular slices at the void location. The local analysis uses a local FE submodel mesh based on the true shape of the void identified from the CT scans. Detection of void shapes in CT data using the density-based contouring technique produced points of the 3D surface of the void that are used by the local meshing code to automatically create a FE mesh of the defect. Figure 5-8 demonstrates the ability of the density-based contouring technique using the CT data to provide with a high-fidelity geometric representation of the seeded defects. The 3D volumetric representation of the defect in the CT data (left in Figure 5-8) was generated by isolating the grey values corresponding to air density in the CT histogram. The slight visible difference in the global shape is due to slightly different 3D perspective renderings in the CT reconstruction software (left) and ABAQUS CAE, where the contouring points have been plotted (right).

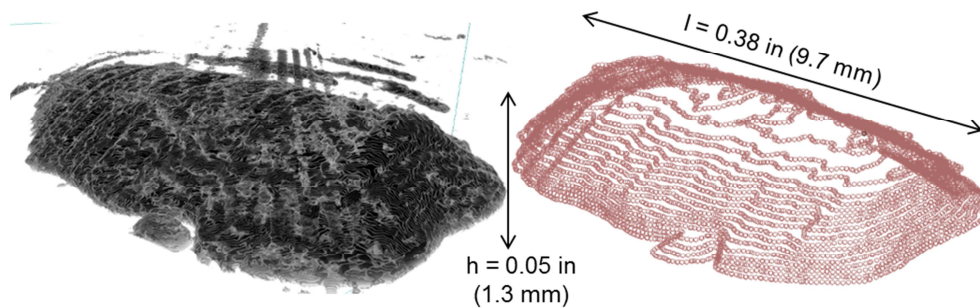


Figure 5-8 CT data (left) and approximation of the void 3D surface using density-based contouring (right) for a seeded porosity defect in the flapping specimens

Linear 8-noded hexagonal 3D elements with reduced integration scheme (C3D8R) are used in the local FE models, with a typical total number of DOF in the 1.0-1.2M range. Displacements from the global model were applied as boundary conditions for the external surfaces of local models. The LaRC04 failure criterion applied to matrix-dominated delamination failure is used to predict failure initiation in the local models.

Detailed description of the technique used for local meshing, including high fidelity representation of defect features extracted from the CT data, is provided in the next section.

## 5.4 Local Meshing of Defect Areas

### 5.4.1 *Mesh Morphing Technique*

One of the key technical challenges of the methodology is the transfer of the CT data into a FE structural mesh able to capture accurately the essential geometric features of the defects, including complex topography of the in-plane and out-of-plane fiber waviness. Mesh morphing techniques are used to simplify and optimize the generation of the local FE mesh that includes accurate geometric representation of the defects while ensuring proper mesh quality for the local stress analysis.

Morphing has been commonly used in the computer graphic community to transform one shape into another [101]. When applied to the generation of a target FE mesh, morphing requires correct mapping of element connectivity, in addition to mapping of the geometry. Elements in the target mesh should not self-intersect or collapse. The Python scripting capability of ABAQUS CAE provides a convenient interface for mesh morphing, with the ability to directly edit and move the nodes of an existing orphan mesh

into the target mesh. This procedure ensures that element connectivity is automatically conserved during the mesh morphing.

Linear morphing transformations were used in Cartesian and Polar coordinate systems depending on convenience of the source mesh description. The procedures for Cartesian and polar mesh morphing are detailed in section 5.4.2.

#### 5.4.2 Mesh Morphing in Cartesian and Polar Coordinates

For illustration purposes, a 2D unidirectional mesh morphing in Cartesian coordinates is considered. The objective is to define the transformation to apply to the source mesh  $\mathcal{M}$  to generate the target mesh  $\mathcal{M}'$ , as illustrated in Figure 5-9. The functions  $f_A$ ,  $f_B$ ,  $f'_A$  and  $f'_B$  that represent respectively the boundaries of the source and the target mesh are supposed to be known.

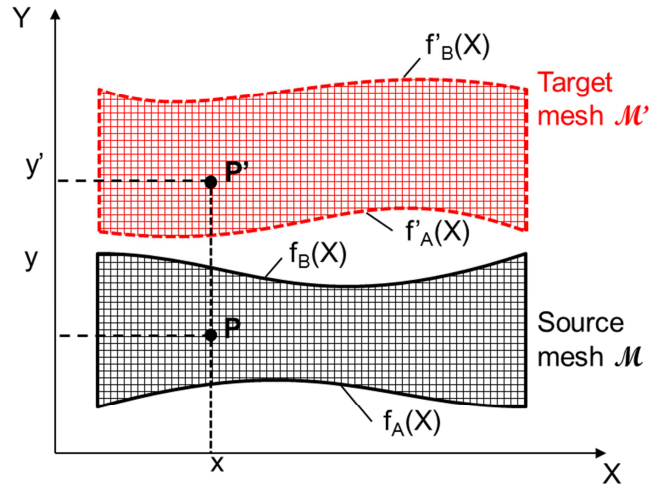


Figure 5-9 Source and target mesh for morphing in Cartesian coordinates

The linear morphing is defined as the transformation from node  $P$  into node  $P'$ , such as the relative distance from node  $P$  to the boundaries  $f_A$  and  $f_B$  is conserved and the X-coordinate remains unchanged:

$$\frac{y' - f'_A(x)}{f'_A(x) - f'_B(x)} = \frac{y - f_A(x)}{f_A(x) - f_B(x)} \quad (5.1)$$

where  $(x,y)$  and  $(x',y')$  are the 2D Cartesian coordinates of target node point  $P$  and source node point  $P'$ , respectively.

Note that this transformation must be continuous and bijective to avoid resulting mesh self-intersections or gaps, i.e. the morphism transformation is an isomorphism. Using Eq. (5.1), the isomorphism  $m_Y$ , can be defined as:

$$m_Y: \begin{matrix} x \\ y \end{matrix} \rightarrow \begin{matrix} x \\ f'_A(x) + \frac{f'_A(x) - f'_B(x)}{f_A(x) - f_B(x)} (y - f_A(x)) \end{matrix} \quad (5.2)$$

Morphing transformations in multi-directions can be easily obtained from composition of unidirectional isomorphisms:

$$m_{XYZ} = m_X \circ m_Y \circ m_Z \quad (5.3)$$

where  $m_X$ ,  $m_Y$  and  $m_Z$  are unidirectional isomorphisms.

The 2D unidirectional mesh morphing linear transformation defined in Eq. (5.2) can be extended to mesh morphing in polar coordinates, where  $r_A(\theta)$  and  $r_B(\theta)$  are the boundaries of the source mesh and  $r'_A(\theta)$  and  $r'_B(\theta)$  the boundaries of the target mesh, as shown in Figure 5-10.

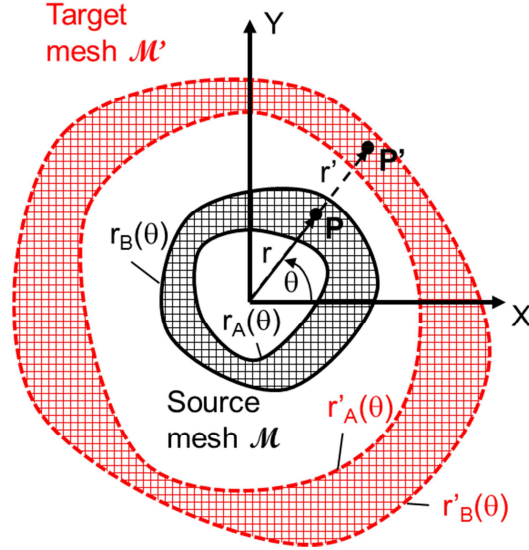


Figure 5-10 Source and target mesh for morphing in polar coordinates

A unidirectional linear mesh morphing transformation along the radial polar coordinate is defined by:

$$m_r: \begin{matrix} r \\ \theta \end{matrix} \rightarrow \begin{matrix} r'_A(\theta) + \frac{r'_A(\theta) - r'_B(\theta)}{r(\theta) - r_B(\theta)} (r - r_A(\theta)) \\ \theta \end{matrix} \quad (5.4)$$

The rule of composition also applies, for a multidirectional polar morphing transformation composed of unidirectional isomorphisms:

$$m_{r\theta Z} = m_r \circ m_\theta \circ m_Z \quad (5.5)$$

#### 5.4.3 Meshing of Defects with In-plane Fiber Waviness

Cartesian and polar linear mesh morphing techniques were used to generate a circular local mesh with in-plane waviness around a void. The resin-rich area typically observed in the CT scans around the air pocket is also represented. Each ply is modeled

as a separate layer. The source mesh for the elements representing the composite material is built from two structured and oriented half circle meshes, as illustrated in Figure 5-11. Oriented half circle meshes are generated using the script described in Appendix C. A symmetric mesh is shown in Figure 5-11 for simplicity. 2D linear Cartesian mesh morphing is applied to generate a target mesh that follows the boundaries of the resin-rich area. The mesh for the resin-rich region is obtained from linear polar morphing of a regular ring mesh, as shown in Figure 5-11.

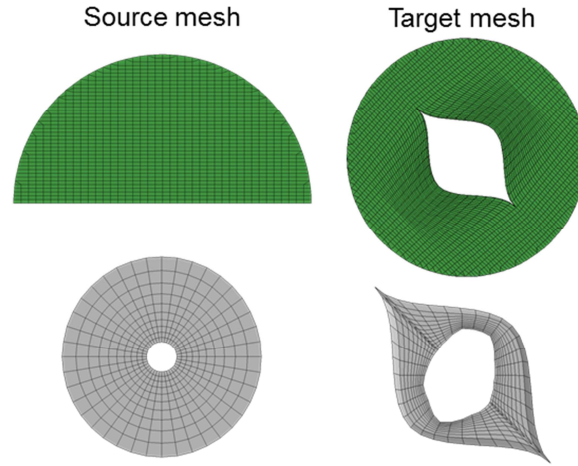


Figure 5-11 Source and target mesh for the composite material (top) and resin-rich area (bottom) for one ply layer of the local FE model with in-plane fiber waviness

It should be noted that the polar morphing for the resin-rich area is composed of two 2D unidirectional isomorphisms, as defined in Eq. (5.5). First, a  $\theta$ -transformation is applied for the angular coordinates of the nodes at the interface between composite material and resin area. Then, a radial isomorphism is applied to superimpose the external and internal boundaries of the resin-rich area with the composite material and the shape of the air pocket, respectively. Nodes at the interface between the resin and



composite material can then be merged. Boundaries for the air pocket and the composite material are extracted as a set of points from the CT data and used to generate continuous boundary spline functions  $f'$  and  $r'$  for the target mesh, as defined previously in Eqs. (5.2) and (5.4).

As illustrated in Figure 5-11, using regular hexahedral elements for the source mesh allows generating a target mesh with elements oriented along the fiber direction. Element edges can then be used to assign local material orientation. Nodal coordinates extracted using Python scripting in the ABAQUS CAE are used to define element-local discrete orientation based on element edges. Local material orientations around the defect with in-plane fiber waviness are illustrated in Figure 5-12 where arrows represent fiber direction.

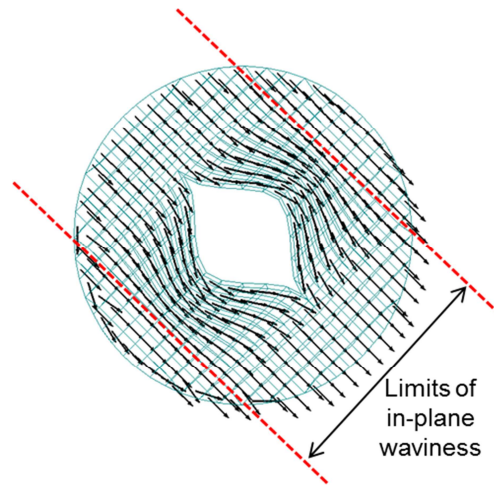


Figure 5-12 Local fiber orientation around the defect in the local FE model with in-plane fiber waviness

It is worth noting that a coarse mesh has been used in Figure 5-12 for visualization purposes only. Also, an additional constraint was applied during the mesh

morphing transformation in order to limit the in-plane waviness to a certain area, based on measurements in CT data. Ply layers are assembled by surface-based tie constraints to build the local sub-model, as shown in Figure 5-13.

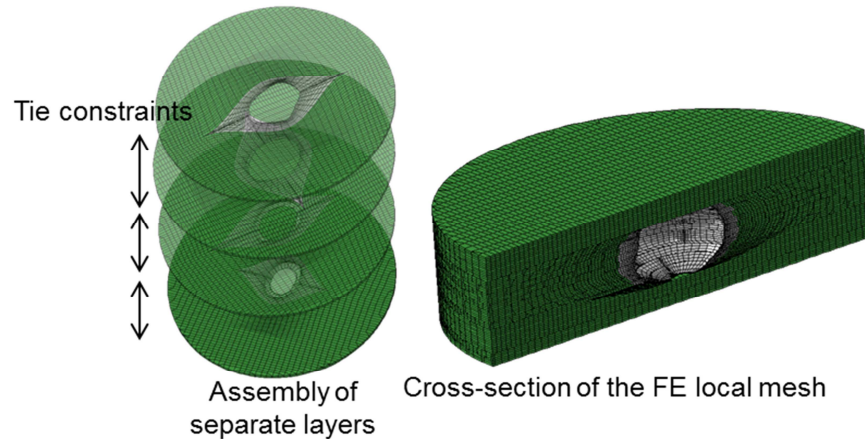


Figure 5-13 Assembly of oriented ply layers and cross-section of the local FE model with in-plane fiber waviness

#### 5.4.4 Meshing of Defects with Out-of-plane Waviness

Mesh morphing was also used to generate local meshes for the defects with out-of-plane waviness. Typical source and target meshes for one ply layer of composite material, and the associated resin-rich area, are illustrated in Figure 5-14. As shown in Figure 5-15, ply layers are assembled to build the final local FE mesh of the defect. Interface nodes are merged for layers with the same mesh discretization. Tied constraints are applied to layer groups with incompatible meshes. This allows using more refined mesh in the area close to a defect as illustrated in Figure 5-15. Element faces are used to compute the discrete field that defines the local orientation for the out-of-plane waviness.

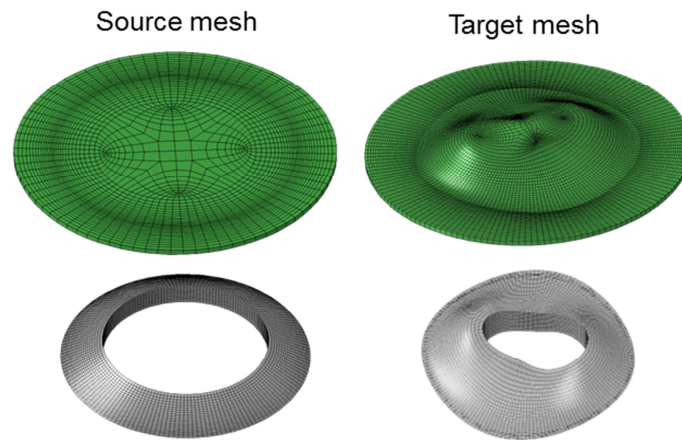


Figure 5-14 Source and target mesh for the composite material (top) and resin-rich area (bottom) for one ply layer of the local FE model with out-of-plane ply waviness

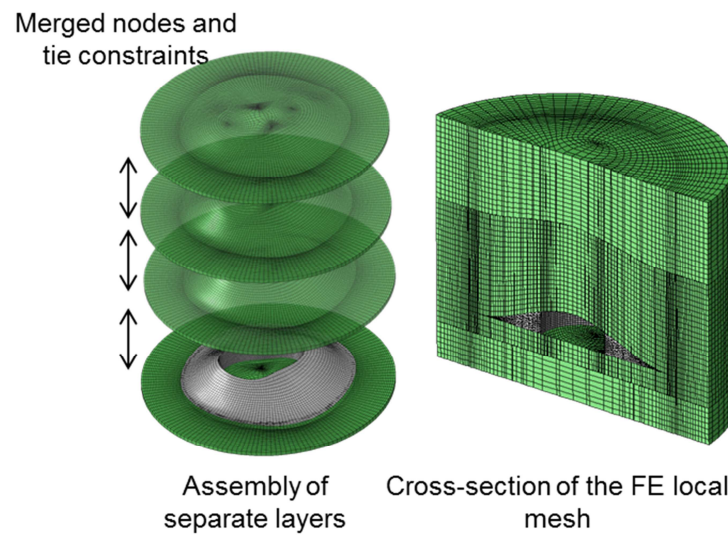


Figure 5-15 Assembly of ply layers and cross-section of the local FE model with out-of-plane ply waviness

## 5.5 Failure Predictions in Caron/Epoxy Flapping Specimens

### 5.5.1 Predictions of Static Failure in Defect-free Specimens

The global FE model is used for prediction of delamination failure in the 68-ply  $[(\pm 45)_2/0_4/45/-45]_s$  IM7/8552 Carbon/Epoxy defect free-specimen under the quasi-static loading. As the loading is applied, interlaminar shear stress concentrations develop under the bolted fixture as shown in Figure 5-16. Failure initiates by delamination due to the combination of interlaminar shear stresses in the (1-3) and (2-3) material planes; where 1 refers to the fiber direction, 2 the transverse direction and 3 the laminate thickness direction. Immediate unstable propagation of delamination after failure onset was observed in tests; therefore prediction of damage progression is not required.

Contour plot of the LaRC04 failure index at 5640 lbs (25.1 kN) is shown in Figure 5-17 for specimen R2, which corresponds to the initiation of delamination failure. The onset of failure is predicted next to the bolted holes, at the 10<sup>th</sup> interface between 0°-plies and  $\pm 45^\circ$ -plies and below the mid-thickness of the specimen. It is worth noting that the contour plots in Figure 5-16 and Figure 5-17 are generated using interlaminar stress calculated at element integration points.

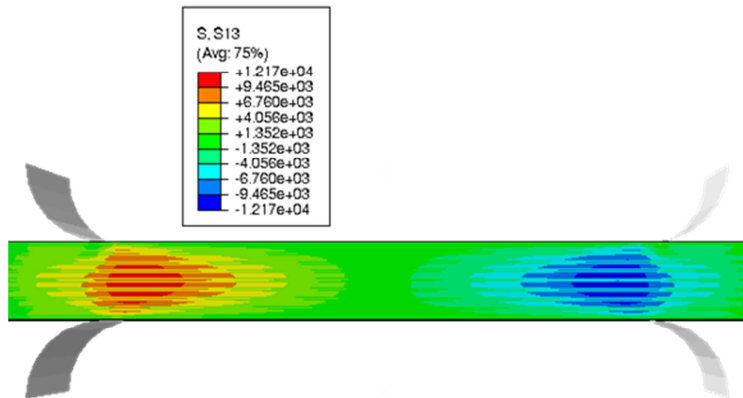


Figure 5-16 Interlaminar shear stress concentration in the global FE model for IM7/8552 flapping element at 4100 lbs (18.2 kN)

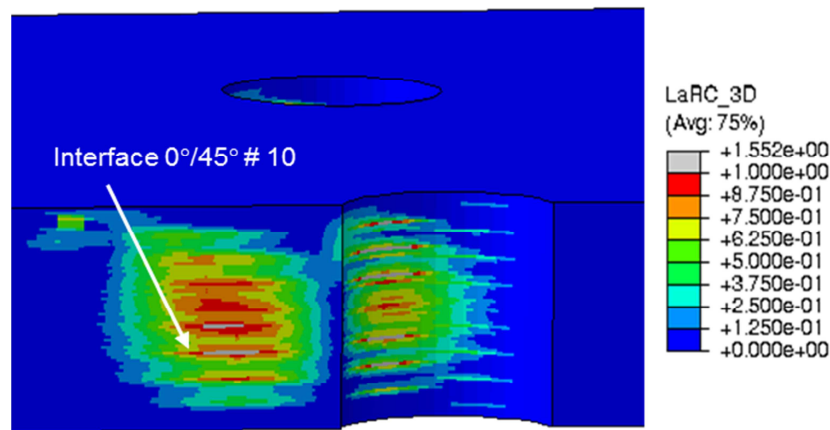


Figure 5-17 LaRC04 failure criteria in the defect-free global FE mesh for IM7/8552 flapping element at 5640 lbs (25.1 kN)

Stress results calculated at element integration points are compared with predictions using the interlaminar stress recovery procedure. Figure 5-18 shows the LaRC04 failure index at failure load at critical ply interfaces, for both integration point and stress-recovery results. The stress recovery-based predictions differ from the predictions

at integration points, as illustrated. A simultaneous failure around 5530 lbs (24.6 kN) is predicted at the 10<sup>th</sup> and 4<sup>th</sup> 0°/45° ply-group interfaces using the stress-recovery procedure, whereas integration-points results show that failure should occur only at the 10<sup>th</sup> 0°/45° interface, at 5640 lbs (25.1 kN). The stress recovery-based prediction of delamination failure at 5050 lbs (22.5 kN) at the 4<sup>th</sup> 0°/45° interface is in excellent agreement with test results.

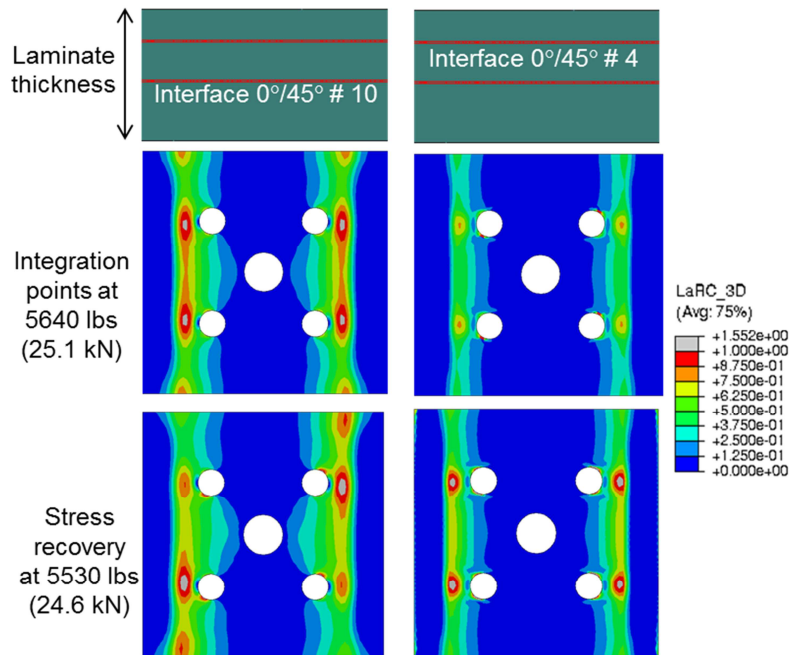


Figure 5-18 LaRC04 failure criteria calculated from stresses at element integration points (top) and using the interlaminar stress-recovery procedure (bottom) at two critical 0°/45° ply interfaces

### 5.5.2 Failure Prediction Using the Local Model

A local FE mesh is built for the most critical seeded defect in IM7/8552 flapping specimen L3. The specimen was quasi-statically loaded to failure using the same test procedure than defect-free specimen R2. The critical defect is selected as the closest seeded defect to the area with interlaminar shear stress concentrations, as shown in Figure 5-16. Location of the defect is determined from the CT data. The CT data also provides with boundary points for the air pocket/resin-rich area and resin-rich area/composite material interfaces. The dimensions of the ply-waviness area are also determined from CT measurements. Mesh-morphing techniques are used to automatically build a local FE sub-model of the defect.

Only out-of-plane waviness is considered, as the effects of in-plane loading in the global model were found negligible compared to the effects of out-of-plane loading. Figure 5-19 shows a cross-sectional view of the global mesh with embedded local mesh including out-of-plane waviness around the critical porosity defect.

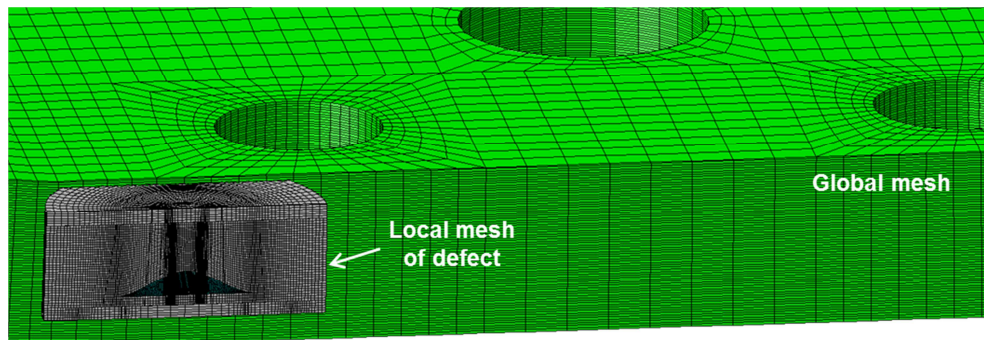


Figure 5-19 Cross-section cut showing local mesh of the critical defect embedded in the global FE mesh

A failure load of 5050 lbs (22.5 kN) is predicted using the local model and the LaRC04 failure criteria, which is in very good agreement with the 4900 lbs (21.8 kN) failure load from tests. Figure 5-20 shows the through-the-thickness contour plot of LaRC04 failure criteria at 5050 lbs (22.5 kN), for the global model alone (top) and the global model with embedded local mesh (bottom). The effects of the defect are clearly identified. Interlaminar stress concentrations develop on top of the defect, at the  $0^\circ/45^\circ$  ply interface where out-of-plane ply waviness is the most severe and initiates delamination failure. Figure 5-21 shows the comparison of the failure pattern with the CT scan of specimen L3. The CT slice is taken approximately at the same section at the location of the void and shows delamination cracks for the plies with strong waviness due to the presence of the void. Note that the void in the CT scan appears smaller due to resin pocket not being clearly visible in this section of the scan. However, including resin pocket in the analysis model appears essential for correct modeling of the out-of-plane waviness defect at the void.



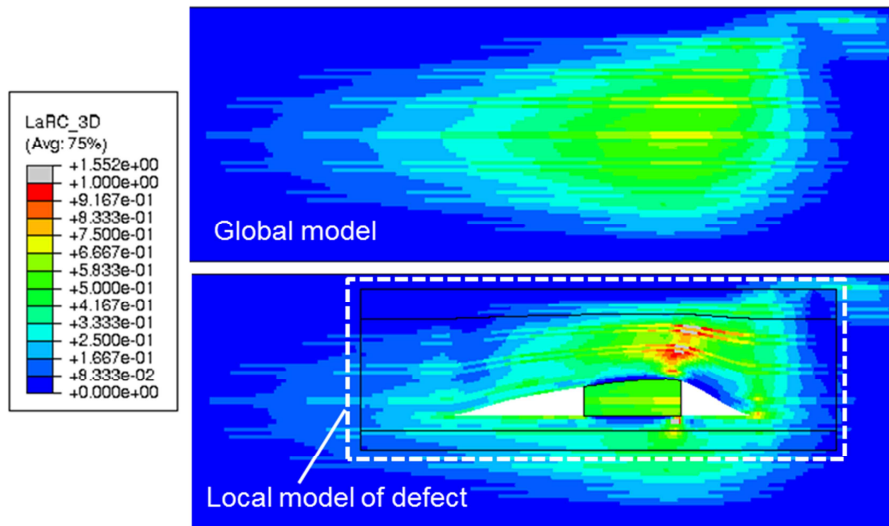


Figure 5-20 LaRC04 failure criteria for the defect-free global model (top) and embedded local model with defect (bottom) at the same cross-section of specimen L3 at 5050 lbs (22.5 kN)

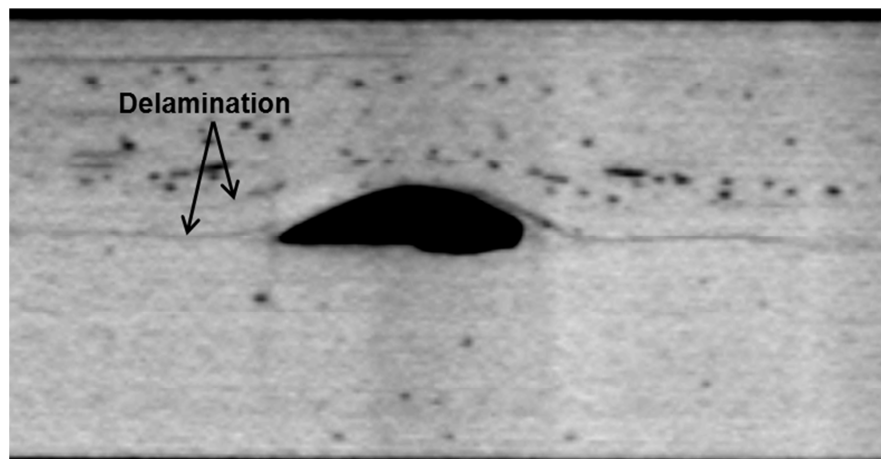


Figure 5-21 Failed void section of the CT scan of L3 specimen (failed at 4900lbs (21.8 kN))

### 5.5.3 Predictions of Fatigue Failure

IM7/8552 flapping specimen R3 with seeded defects was tested in fatigue under 3400 lbs (15.1 kN) peak load with  $R=0.1$  and 1.5 Hz frequency. The DIC technique was used to monitor surface strains in the areas of shear stress concentrations under the fixture, as shown in Figure 5-16. DIC pictures were taken every 250 cycles, enabling accurate detection of delamination failure. Immediate unstable propagation of delamination after failure onset was observed, similar to static tests; therefore no damage propagation scheme was included in fatigue failure predictions.

To predict fatigue failure, the interlaminar tensile and shear strength values used in the LaRC04 criterion are adjusted using the IM7/8852 S-N curves obtained for a load ratio  $R=0.1$  [6]:

$$\begin{aligned} S_{33}(N) &= 1.575S_{33,static}(\log N)^{-0.733} \\ S_{13}(N) &= 1.284S_{13,static}(\log N)^{-0.4123} \\ S_{23}(N) &= 1.284S_{23,static}(\log N)^{-0.4123} \end{aligned} \quad (5.6)$$

where  $S_{ij,static}$  are the interlaminar tensile and shear strengths.

Eqs. (4.6) are substituted in the expression of the failure criteria and the algebraic equation obtained is solved for the number of cycles  $N_f$  to failure for each elements, using stresses calculated under application of the fatigue peak load. The minimum number of cycles  $N_f$  predicts initiation of fatigue failure.

A local FE model of the most critical seeded defect was built from CT data and using mesh morphing techniques, as described previously. Displacement boundary conditions for the local model are provided by the global model under the 3400 lbs (15.1 kN) peak load. Figure 5-22 shows the contour plot of the number of cycles to failure for IM7/8552 flapping specimen R3 with defects, using a local FE model with out-of-plane

waviness for the critical defect. Displacement boundary conditions for the local model are provided by the global model under the 3400 lbs (15.1 kN) peak load. Failure is predicted at 9,200 cycles at the 0°/45° ply interface below the defect, as illustrated. The Figure also shows excellent agreement with CT data for the location of the delamination crack, as it passes through the location of maximum damage in the FEM model.

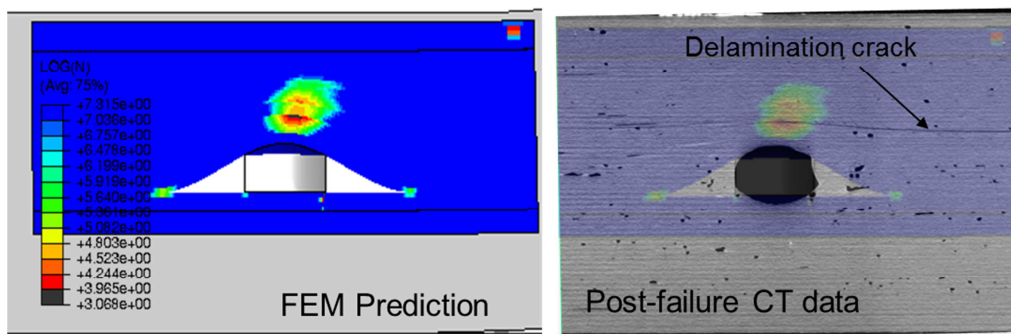


Figure 5-22. Contour plot of the Log (number of cycles to failure) in the local model for specimen R3b (left) and comparison with the crack location from the CT data (right). The contour plot from FEM simulation is superimposed using transparency on the CT image (right)

#### 5.5.4 Summary of Failure Predictions

Table 5-1 summarizes the prediction results for static and fatigue failures of the 68-ply [(±45)2/04]4/45/-45]s IM7/8552 flapping specimens. Comparison with test results is also provided. Very good agreement between FEM simulations and test data is documented.

Table 5-1 Comparison between FE simulation and test data for static and fatigue failures of IM7/8552 flapping elements

Specimen	FE Simulation		Test data	
	Failure load, lbs (kN)	Cycles to failure	Failure Load, lbs (kN)	Cycles to failure
<b>R2 (defect-free)</b>	5,530 (24.6)	-	5,500 (24.5)	-
<b>L3 (with defects)</b>	5,050 (22.4)	-	4,900 (21.8)	-
<b>R3 (with defects)</b>	-	9,250	-	11,000

## Chapter 6

### Conclusion and Future Work

A virtual test methodology for predictions of failures in composites is proposed in this work. The method uses three-dimensional FE modeling for predicting the onset and progression of matrix-dominated failures, which are the primary modes of failure in composite laminates utilized in aerospace composite structural designs. LaRC04 stress-based failure criteria were combined with a continuum damage model implemented for all failure mechanisms, including delamination failure. The formulation enabled predicting both the onset and propagation of intralaminar and interlaminar failures until they reach a detectable size, without a priori knowledge of initial damage or pre-determined paths for crack propagation. The model was also able to account for the interactions between matrix cracking and delamination, which can be critical for accurate failure prediction in laminate composite designs used in aerospace applications. The progressive damage model was extended to fatigue loading by combining stress-based fatigue element failure and damage accumulation due to variable stress conditions.

The capacity of the method to predict strength, damage topography and fatigue cycles to failure was verified for open hole tension and open hole compression Carbon/Epoxy laminate test articles. DIC monitoring of surface stains allows tracking the growth of matrix cracks in the surface ply, and very good correlation with FE predictions was demonstrated. Three-dimensional visualization using X-Ray computed Tomography, including CT inspection under loading, was used and provided an unparalleled insight in the sub-surface damage tomography and failure mode interactions. Both simulation and CT visualization show that the progression of delamination is highly dependent on the interaction with matrix cracks in the adjacent plies. Predictions of sub-surface damage

developments in the FE models, including sizes and locations, were in excellent agreement with CT data. The virtual test methodology seems feasible at the material scale, and virtual tests will undoubtedly allow reducing the cost and increasing the efficiency of material qualification.

The development of methods to capture the effects of manufacturing defects at material scale, using high-fidelity nondestructive inspection techniques, also seems to be on the right track. High-resolution non-destructive evaluation (NDE) methods such as 3D X-ray microfocus computed tomography (CT) have introduced a major change in defect analysis, as automatic detection of porosity/voids in composites and accurate measurement of their three-dimensional geometry becomes feasible due to high quality of the CT scans. Moreover, the ability to integrate accurate high-fidelity measurements of defects into structural analysis could represent a major shift from just detection of defects to understanding their effects. In this work, CT measurements of porosity defects present in curved-beam test specimens were integrated into finite element stress analysis to capture the effects of defects on ILT performance. Once the effects of defects were captured through transfer of the CT measurements into a three-dimensional finite element model, the scatter in the curved-beam static and fatigue test data was reduced; and reliable material ILT strength and fatigue properties could be determined. The ILTS properties derived from the curved-beam tests with integration of the effects of defects were compared with data from a derivative ILTS test based on defect-free prismatic short-beam specimens, and excellent agreement was demonstrated. This work showed that it is not the porosity volume content, but the presence of individual small voids at critical locations that affects ILT behavior. Indeed, the presence of individual microscopic voids at critical locations of curved-beam specimens caused large scatter in the ILT fatigue performance despite extremely low porosity content (less than 0.12%).

The potential benefits of the ability to accurately characterize the material structure and transfer associated non-destructive measurements into structural failure models (virtual testing) extend beyond the curved-beam tests. It was found that accuracy of non-destructive inspection is needed to quantify the defects and paramount in determining their effects on structural performance. Once knowledge of the part condition in terms of critical defect location and size, and their influence on residual strength and useful life are established, a shift from statistic-based to condition-based structural substantiation could be realized. However, one question is the ability of transitioning the material scale methodology to larger composite structures. Structures might include features and phenomena that are not encountered in smaller coupons.

The methodology developed at the material scale was applied to the prediction of failures in 2-feet (60 cm) long thick laminates representative of structural components found in composite rotorcraft structures. Porosity voids representative of structural-scale manufacturing defects were intentionally introduced at critical locations in the specimens. CT inspections revealed that porosity defects were not a simple scale-up of voids observed at the material scale in unidirectional curved-beam coupons. Complex laminate topography was observed around the defects, with the presence of significant in-plane and out-of-plane waviness and resin rich areas. Advanced meshing techniques were successfully implemented to automatically transfer the defect information into local finite element models, including void locations, sizes and shapes, and in-plane and out-of-plane ply waviness. Out-of-plane fiber waviness was found especially important in virtual test simulations. Predicted stress concentrations due to out-of-plane waviness resulted in excellent correlations in failure loads (for static loading) and cycles to failure (in fatigue), as well as in accurate predictions of failure locations.

However, these results should be considered with some reservations. Transitioning the material scale method to the structural scale is far from being a simple task. Accurate numerical predictions of static and fatigue failure in structural elements seem only feasible provided that the structure of manufacturing defects is adequately represented in the computational model. Indeed, some of the structural elements tested showed unexpected early failures at very low load levels. CT inspections suggested a lower laminate quality for these specimens, including increased porosity content. However, the scatter in test data could not be quantified using the current prognosis method.

These difficulties suggest future improvements for the methodology. In particular, statistical approaches could improve the transfer of CT information into structural analysis when a methodology based on discrete modelling of critical individual defects is not straightforward or possible. Projection that speed and spatial resolution of the CT technology will continue to increase in the future also implies that the level of details that can potentially be incorporated into structural models will also improve. The challenge is to formulate constitutive models that allow for integration of such level of details, while being useful for engineering purposes. High-resolution computed tomography, such as CT based on synchrotron radiation, has already proven its ability to achieve microscale resolution suitable for observation of individual composite fiber breakage and debonding. Such technology offers promising perspectives in the development of micro-mechanics-based failure models, which could eventually lead to the establishment of a comprehensive method for integration of all material discontinuities into structural analysis. High resolution in CT scans is typically traded for larger fields of view. However, development of new X-ray technology, such as high flux coherent X-Ray sources, as well as algorithms for reconstruction of partial scans, could overcome this trade-off. The



technology might improve one day to the point of permitting CT scanning of structural subcomponents with microscopic resolution. Such capability could establish the path for the challenging task of linking micromechanics-based models to models representative of the performance and response of composite structures under service loading and conditions.

Short term improvements of the virtual test methodology presented in this work could also be part of a follow-up effort to ameliorate the virtual test method at the material scale. Accurate calculations of interlaminar stresses are critical to capture the onset and progression of delamination failure. A stress recovery based on a tied-contact formulation was proposed in this work to improve the predictions. However, tied-contact implemented for three-dimensional elements typically introduces a large number of Lagrange multiplier variables in the FE model and can quickly increase computational costs. A user-defined three-dimensional element integrated at the ply interface, that combines a continuum damage model for delamination failure consistent with the kinematics of intralaminar failure, with features for accurate evaluation of the three-dimensional stress state at the ply interface, could be an efficient alternative. Improvements of the regularization method should also be considered. Crack band regularization based on the limitation of the element size perpendicular to the fracture plane has been used in this work. However, this approach requires calibration with tests results to determine the correct crack band width. A better way to implement the regularization would be to ensure conservation of the strain energy released within the finite element during crack progression. The difficulty in this approach is the availability of meaningful fracture toughness data. The recent development of an integrated customized load frame for the Northstar CT system used in this work has shown promising perspectives in high fidelity inspections of specimens under loading, enabling accurate in-situ measurements of crack growth and

three-dimensional evaluation of the progression of damage topography in laminates. Such data could lead to the characterization of relevant critical fracture energy quantities that could be used as a basis for the regularization of the continuum damage model.

## Appendix A

### Determination of the Number of Cycles to Failure for Matrix Tensile Failure

Details on the determination of the number of cycles to failure for transverse tensile matrix failure using the LaRC04 failure criterion and fatigue S-N curves are provided in this Appendix. The procedure is similar for any other failure criteria.

Fatigue S-N curves for transverse tension and in-plane shear obtained by Log-Linear least-squares fit of the test data are given as:

$$\begin{aligned} S_{22}^f(N) &= S_{22}^{static} a_{22} (\log N)^{b_{22}} \\ S_{12}^f(N) &= S_{12}^{static} a_{12} (\log N)^{b_{12}} \end{aligned} \quad (7.1)$$

Using  $X = \log(N)$  and  $a_{ij} = S_{ij}^{static} a_{ij}$ , the fatigue curves are written as:

$$\begin{aligned} S_{22}^f(X) &= a_{22} X^{22} \\ S_{12}^f(X) &= a_{12} X^{b_{12}} \end{aligned} \quad (7.2)$$

Replacing the strengths  $S_{22}$  and  $S_{12}$  by fatigue strengths given in Eqs. (7.2) in the the LaRC04 criterion for matrix tensile cracking gives:

$$f(X) = (1 - g) \frac{\sigma_{22}}{a_{22} X^{b_{22}}} + g \left( \frac{\sigma_{22}}{a_{12} X^{b_{12}}} \right)^2 + \frac{\frac{\tau_{12}^2}{2G_{12}} + \frac{K_{12}}{\frac{1}{n_{12}} + 1} \left( \frac{|\tau_{12}|}{K_{12}} \right)^{\frac{1}{n_{12}} + 1}}{\frac{a_{12}^2 X^{2b_{12}}}{2G_{12}} + \frac{K_{12}}{\frac{1}{n_{12}} + 1} \left( \frac{a_{12} X^{b_{12}}}{K_{12}} \right)^{\frac{1}{n_{12}} + 1}} \quad (7.3)$$

– 1

Where finding the number of cycles to failure  $N^f$  for matrix tensile cracking is equivalent to finding the root  $X^f = \log(N^f)$  such as  $f(X^f) = 0$ .

Numerical approximations of the roots are found using the Newton-Raphson iterative procedure:

$$X_{n+1} = X_n - \frac{f(X_n)}{f'(X_n)} \quad (7.4)$$

Where  $f'$  is the derivative of function  $f$ .

The root  $X$  is found by starting with a first guess  $X_0$  in Eq. (7.4) and repeating the process until convergence is achieved.

The analytical expression of  $f'$  is given by:

$$f'(X) = - \left[ (1-g) \frac{\sigma_{22}}{a_{22}^2 X^{2b_{22}}} + 2g \frac{\sigma_{22}^2}{a_{22}^3 X^{3b_{22}}} \right] b_{22} a_{22} X^{b_{22}-1} \\ - \frac{\frac{\tau_{12}^2}{2G_{12}} + \frac{K_{12}}{\frac{1}{n_{12}} + 1} \left( \frac{|\tau_{12}|}{K_{12}} \right)^{\frac{1}{n_{12}}+1}}{\left[ \frac{a_{12}^2 X^{2b_{12}}}{2G_{12}} + \frac{K_{12}}{\frac{1}{n_{12}} + 1} \left( \frac{a_{12} X^{b_{12}}}{K_{12}} \right)^{\frac{1}{n_{12}}+1} \right]^2} \left[ \frac{a_{12} X^{b_{12}}}{G_{12}} \right. \\ \left. + \left( \frac{a_{12} X^{b_{12}}}{K_{12}} \right)^{\frac{1}{n_{12}}} \right] b_{12} a_{12} X^{b_{12}-1} \quad (7.5)$$

With  $\sigma_{22} > 0$  for transverse tension,  $b_{22}$  and  $b_{12} < 0$ ,  $a_{22}$  and  $a_{12} > 0$ :

$$f'(X) > 0 \text{ for all } X > 0 \text{ (} N > 1 \text{)}$$

$$\lim_{X \rightarrow 0} f(X) = -1 \quad (7.6)$$

$$\lim_{X \rightarrow +\infty} f(X) = +\infty$$

Therefore  $f$  has a unique root  $X^f$  that can be found numerically using Eq. (7.4).  $X_0=5$  (N=100,000) was used.

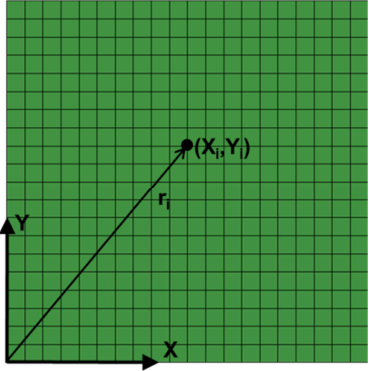
## Appendix B

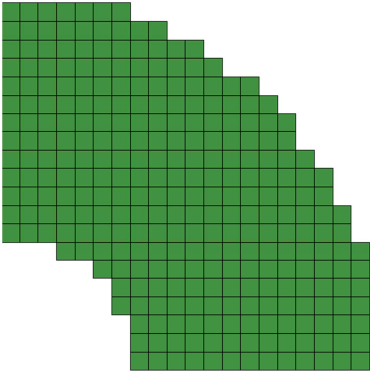
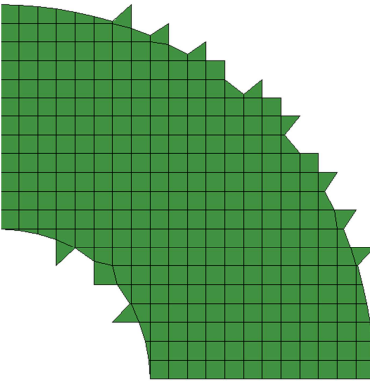
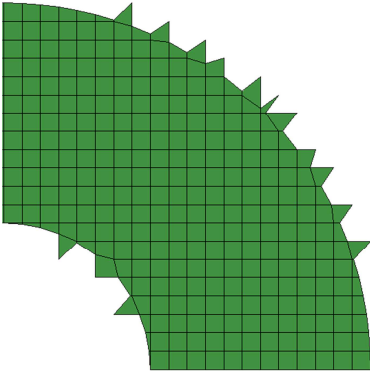
### Generation of a Circular Oriented Mesh

This Appendix describes the Python algorithm used to generate a regular oriented circular mesh for the local FE submodels presented in this work for OHC and OHT coupons and local models with in-plane waviness.

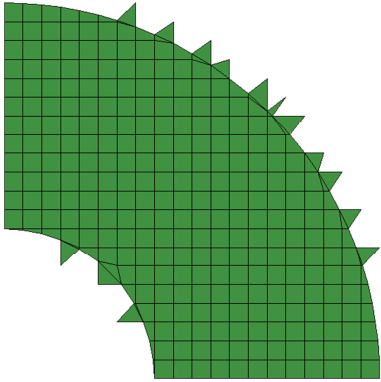
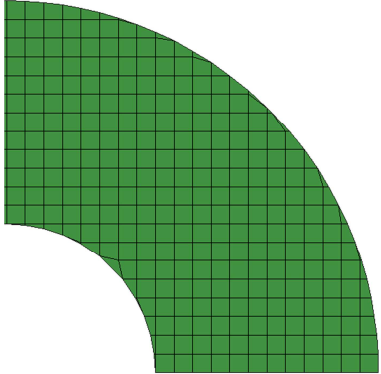
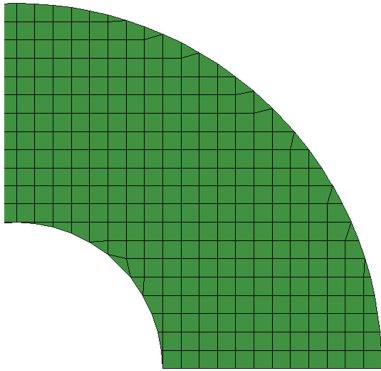
The steps of the algorithm for generation for one quarter of the circular mesh are illustrated here. The full mesh can be easily built by using symmetric duplication. For illustration purposes, squared elements are used. The procedure is the same if elements with different aspect ratios and mesh refinements are included.

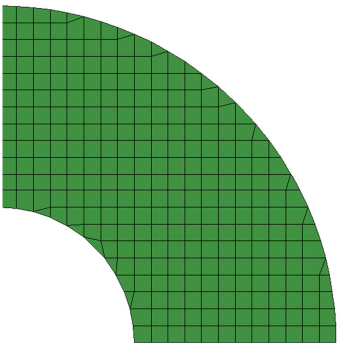
For references,  $R_o$  and  $R_i$  are the outer and inner radius of the circular mesh, respectively.  $(X_i, Y_i)$  refers to the X-axis and Y-axis coordinates of a node  $i$  in the  $(X, Y)$  Cartesian coordinate system and  $r_i$  is the radius of the node in polar coordinate, as illustrated in the first figure below.

Step	Operation	Resulting mesh
1	Create a regular mesh of a square of side $R_o$ .	

2	<p>For each elements, find the number of nodes <math>N</math> outside the boundaries (<math>r_i &lt; R_o</math> or <math>r_i &gt; R_i</math>).</p> <p>If <math>N = 4</math>, delete element</p>	
3	<p>If <math>N = 2</math>, move the 2 nodes outside to match boundaries <math>r = R_o</math> or <math>r = R_i</math> such as:</p> <p>if <math>Y_i</math> is the same for the 2 nodes:  <math>X_i = \text{constant}</math>  else:  <math>Y_i = \text{constant}</math></p>	
3	<p>If <math>N = 1</math>, move node outside to match boundary <math>r = R_o</math> or <math>r = R_i</math> such as:</p> <p>if <math>X_i &lt; Y_i</math>:  <math>X_i = \text{constant}</math>  else:  <math>Y_i = \text{constant}</math></p>	



5	<p>If <math>N = 3</math>, split quad element into 2 triangular elements using the 2 nodes lying on the boundary <math>r = R_o</math> or <math>r = R_i</math></p>	
6	<p>Delete Triangular elements with one node outside the boundaries</p>	
7	<p>For small triangular elements with area <math>&lt; A_{min}</math>, delete element and move node that was inside the boundary such as:</p> <p>if <math>X_i &lt; Y_i</math>:  <math>X_i = \text{constant}</math>  else:  <math>Y_i = \text{constant}</math></p> <p>Convert degenerated quad elements into triangular elements</p>	

8	<p>New small triangular elements can be created at the end of step 7.</p> <p>Repeat step 7 until there is no small triangular elements at the end of the step.</p>	
---	--	--

## References

- [1]. Guyett, P. R., & Cardrick, A. W. (1980). The certification of composite airframe structures. *Aeronautical Journal*, 84, 188-203.
- [2]. Cox, B., & Yang, Q. (2006). In quest of virtual tests for structural composites. *science*, 314(5802), 1102-1107.
- [3]. Makeev, A., He, Y., Carpentier, P., & Shonkwiler, B. (2012). A method for measurement of multiple constitutive properties for composite materials. *Composites Part A: Applied Science and Manufacturing*, 43(12), 2199-2210.
- [4]. Makeev, A., He, Y., & Schreier, H. (2013). Short-beam Shear Method for Assessment of Stress–Strain Curves for Fibre-reinforced Polymer Matrix Composite Materials. *Strain*, 49(5), 440-450.
- [5]. Makeev, A., Carpentier, P., & Shonkwiler, B. (2014). Methods to measure interlaminar tensile modulus of composites. *Composites Part A: Applied Science and Manufacturing*, 56, 256-261.
- [6]. Makeev, A. (2013). Interlaminar shear fatigue behavior of glass/epoxy and carbon/epoxy composites. *Composites Science and Technology*, 80, 93-100.
- [7]. US Department of Defense. Military handbook – MIL-HDBK-17-1F (2002). *Composite materials handbook, Polymer Matrix composites guidelines for characterization of structural materials*, 2002(1).
- [8]. Dobyns, A., Rousseau, C. Q., & Minguet, P. (2000). Helicopter applications and design. *Delaware Composites Design Encyclopedia*, 5, 223-242.
- [9]. Fagiano, C., Abdalla, M. M., Kassapoglou, C., & Gürdal, Z. (2010). Interlaminar stress recovery for three-dimensional finite elements. *Composites Science and Technology*, 70(3), 530-538.
- [10]. Bazant, Z. P., & Planas, J. (1997). Fracture and size effect in concrete and other quasibrittle materials (Vol. 16). CRC press.
- [11]. Makeev, A., Seon, G., & Lee, E. (2010). Failure predictions for carbon/epoxy tape laminates with wavy plies. *Journal of composite materials*, 44(1), 95-112.
- [12]. Nikishkov, Y., Makeev, A., & Seon, G. (2010). Simulation of damage in composites based on solid finite elements. *Journal of the American Helicopter Society*, 55(4), 42009.
- [13]. Nikishkov, Y., Makeev, A., & Seon, G. (2013). Progressive fatigue damage simulation method for composites. *International Journal of Fatigue*, 48, 266-279.
- [14]. Nikishkov, Y., Seon, G., & Makeev, A. (2013). Structural analysis of composites with porosity defects based on X-ray computed tomography. *Journal of Composite Materials*, 0021998313494917.

- [15]. Seon, G., Makeev, A., Nikishkov, Y., & Lee, E. (2013). Effects of defects on interlaminar tensile fatigue behavior of carbon/epoxy composites. *Composites Science and Technology*, 89, 194-201.
- [16]. Makeev, A., Seon, G., Nikishkov, Y., & Lee, E. (2014). Methods for assessment of interlaminar tensile strength of composite materials. *Journal of Composite Materials*, 0021998314525979.
- [17]. Tsai, S. W., & Wu, E. M. (1971). A general theory of strength for anisotropic materials. *Journal of composite materials*, 5(1), 58-80.
- [18]. O'Brien, T. K. (2001). Fracture mechanics of composite delamination. *Materials Park, OH: ASM International, 2001.*, 241-245.
- [19]. Wang, S. S. (1983). Fracture mechanics for delamination problems in composite materials. *Journal of Composite Materials*, 17(3), 210-223.
- [20]. Krueger, R., Minguet, P. J., & O'Brien, T. K. (2003). Implementation of interlaminar fracture mechanics in design: an overview. *TECHNICAL PAPERS-SOCIETY OF MANUFACTURING ENGINEERS-ALL SERIES*.
- [21]. Hashin, Z., & Rotem, A. (1973). A fatigue failure criterion for fiber reinforced materials. *Journal of composite materials*, 7(4), 448-464.
- [22]. Rotem, A., & Hashin, Z. (1975). Failure modes of angle ply laminates. *Journal of Composite Materials*, 9(2), 191-206.
- [23]. Hashin, Z. (1980). Failure criteria for unidirectional fiber composites. *Journal of applied mechanics*, 47(2), 329-334.
- [24]. Sun, C. T., Quinn, B. J., Oplinger, D. W. (1996). Comparative evaluation of failure analysis methods for composite laminates (No. DOT/FAA/AR-95/109).
- [25]. Puck, A. (1996). Festigkeitsanalyse von Faser-Matrix-Laminaten: Modelle für die Praxis. München: Hanser.
- [26]. Puck, A., & Schürmann, H. (1998). Failure analysis of FRP laminates by means of physically based phenomenological models. *Composites Science and Technology*, 58(7), 1045-1067.
- [27]. Salençon, J. (2001). Handbook of continuum mechanics: general concepts-thermoelasticity. Springer.
- [28]. Hahn, H.T., Johannesson, T. (1983). In: Dvorak GJ, editor. Mechanics of composite materials. AMD; 1983, 135-42
- [29]. Davila, C. G., Camanho, P. P., & Rose, C. A. (2005). Failure criteria for FRP laminates. *Journal of Composite materials*, 39(4), 323-345.
- [30]. Pinho, S. T., Dávila, C. G., Camanho, P. P., Iannucci, L., & Robinson, P. (2005). Failure models and criteria for FRP under in-plane or three-dimensional stress states including shear non-linearity. *NASA Technical Memorandum*, 213530, 18.

- [31]. Talreja, R. (1985). Transverse cracking and stiffness reduction in composite laminates. *Journal of composite materials*, 19(4), 355-375.
- [32]. Laws, N., Dvorak, G. J., & Hejazi, M. (1983). Stiffness changes in unidirectional composites caused by crack systems. *Mechanics of Materials*, 2(2), 123-137.
- [33]. Nuismer, R. J., & Tan, S. C. (1988). Constitutive relations of a cracked composite lamina. *Journal of Composite Materials*, 22(4), 306-321.
- [34]. McCartney, L. N. (2005). Energy-based prediction of progressive ply cracking and strength of general symmetric laminates using an homogenisation method. *Composites Part A: Applied Science and Manufacturing*, 36(2), 119-128.
- [35]. Kachanov, L. M. (1958). Time of the rupture process under creep conditions. *Isv. Akad. Nauk. SSR. Otd Tekh. Nauk*, 8, 26-31.
- [36]. Maimí, P., Camanho, P. P., Mayugo, J. A., & Dávila, C. G. (2007). A continuum damage model for composite laminates: part I—constitutive model. *Mechanics of Materials*, 39(10), 897-908.
- [37]. Maimí, P., Camanho, P. P., Mayugo, J. A., & Dávila, C. G. (2007). A continuum damage model for composite laminates: part II—computational implementation and validation. *Mechanics of Materials*, 39(10), 909-919.
- [38]. Camanho, P. P., & Dávila, C. G. (2002). Mixed-mode decohesion finite elements for the simulation of delamination in composite materials. *NASA-Technical paper*, 211737(1), 33.
- [39]. Rybicki, E. F., & Kanninen, M. F. (1977). A finite element calculation of stress intensity factors by a modified crack closure integral. *Engineering Fracture Mechanics*, 9(4), 931-938.
- [40]. Dugdale, D. S. (1960). Yielding of steel sheets containing slits. *Journal of the Mechanics and Physics of Solids*, 8(2), 100-104.
- [41]. Barenblatt, G. I. (1962). The mathematical theory of equilibrium cracks in brittle fracture. *Advances in applied mechanics*, 7(1), 55-129.
- [42]. Goyal, V. K., Jaunky, N. R., Johnson, E. R., & Ambur, D. R. (2004). Intralaminar and interlaminar progressive failure analyses of composite panels with circular cutouts. *Composite Structures*, 64(1), 91-105.
- [43]. Iarve, E. V., Gurvich, M. R., Mollenhauer, D. H., Rose, C. A., & Dávila, C. G. (2011). Mesh-independent matrix cracking and delamination modeling in laminated composites. *International Journal for Numerical Methods in Engineering*, 88(8), 749-773.
- [44]. Hallett, S. R., Jiang, W. G., Khan, B., & Wisnom, M. R. (2008). Modelling the interaction between matrix cracks and delamination damage in scaled quasi-isotropic specimens. *Composites Science and Technology*, 68(1), 80-89.

- [45]. Maimí, P., Mayugo, J. A., & Camanho, P. P. (2008). A three-dimensional damage model for transversely isotropic composite laminates. *Journal of Composite Materials*, 42(25), 2717-2745.
- [46]. Miner, M. A. (1945). Cumulative damage in fatigue. *Journal of applied mechanics*, 12(3), 159-164.
- [47]. Broutman, L. J., & Sahu, S. (1972). A new theory to predict cumulative fatigue damage in fiberglass reinforced plastics. *Composite materials: testing and design*, 497, 170-188.
- [48]. Post, N. L., Case, S. W., & Lesko, J. J. (2008). Modeling the variable amplitude fatigue of composite materials: A review and evaluation of the state of the art for spectrum loading. *International Journal of Fatigue*, 30(12), 2064-2086.
- [49]. Halpin, C., Jerina, K. L., & Johnson, T. A. (1973). Characterization of composites for the purpose of reliability evaluation. In *Analysis of the Test Methods for High Modulus Fibers and Composites: A Symposium* (Vol. 521, p. 1). ASTM International.
- [50]. Philippidis, T. P., & Passipoularidis, V. A. (2007). Residual strength after fatigue in composites: theory vs. experiment. *International Journal of Fatigue*, 29(12), 2104-2116.
- [51]. Hashin, Z. (1985). Cumulative damage theory for composite materials: residual life and residual strength methods. *Composites Science and Technology*, 23(1), 1-19.
- [52]. Reifsnider, K. L., & Stinchcomb, W. W. (1986). A critical-element model of the residual strength and life of fatigue-loaded composite coupons. *Composite materials: fatigue and fracture*, ASTM STP, 907, 298-313.
- [53]. Shokrieh, M. M., & Lessard, L. B. (2000). Progressive fatigue damage modeling of composite materials, Part I: Modeling. *Journal of Composite Materials*, 34(13), 1056-1080.
- [54]. Shokrieh, M. M., & Taheri-Behrooz, F. (2010). Progressive fatigue damage modeling of cross-ply laminates, I: Modeling Strategy. *Journal of composite materials*, 44(10), 1217-1231.
- [55]. Chou, P. C., & Croman, R. (1979). Degradation and sudden-death models of fatigue of graphite/epoxy composites. *Composite Materials: Testing and Design*, ASTM STP, 674, 431-454.
- [56]. Tserpes, K. I., Papanikos, P., Labeas, G., & Pantelakis, S. (2004). Fatigue damage accumulation and residual strength assessment of CFRP laminates. *Composite Structures*, 63(2), 219-230.
- [57]. Lian, W., & Yao, W. (2010). Fatigue life prediction of composite laminates by FEA simulation method. *International Journal of Fatigue*, 32(1), 123-133.
- [58]. Basu, S., Waas, A. M., & Ambur, D. R. (2007). Prediction of progressive failure in multidirectional composite laminated panels. *International Journal of Solids and Structures*, 44(9), 2648-2676.

- [59]. Hufner, D. R., & Accorsi, M. L. (2009). A progressive failure theory for woven polymer-based composites subjected to dynamic loading. *Composite Structures*, 89(2), 177-185.
- [60]. Hsu, D. K., & Uhl, K. M. (1987). A morphological study of porosity defects in graphite-epoxy composites. In *Review of progress in quantitative nondestructive evaluation* (pp. 1175-1184). Springer US.
- [61]. Judd, N. C. (1978). Voids and their effects on the mechanical properties of composites--an appraisal.
- [62]. Olivier, P., Cottu, J. P., & Ferret, B. (1995). Effects of cure cycle pressure and voids on some mechanical properties of carbon/epoxy laminates. *Composites*, 26(7), 509-515.
- [63]. de Almeida, S. F. M., & Neto, Z. D. S. N. (1994). Effect of void content on the strength of composite laminates. *Composite structures*, 28(2), 139-148.
- [64]. Costa, M. L., Almeida, S. F. M., & Rezende, M. C. (2001). The influence of porosity on the interlaminar shear strength of carbon/epoxy and carbon/bismaleimide fabric laminates. *Composites Science and Technology*, 61(14), 2101-2108.
- [65]. Wisnom, M. R., Reynolds, T., & Gwilliam, N. (1996). Reduction in interlaminar shear strength by discrete and distributed voids. *Composites Science and Technology*, 56(1), 93-101.
- [66]. Hagstrand, P. O., Bonjour, F., & Månson, J. A. (2005). The influence of void content on the structural flexural performance of unidirectional glass fibre reinforced polypropylene composites. *Composites Part A: Applied Science and Manufacturing*, 36(5), 705-714.
- [67]. Madsen, B., & Lilholt, H. (2003). Physical and mechanical properties of unidirectional plant fibre composites—an evaluation of the influence of porosity. *Composites Science and Technology*, 63(9), 1265-1272.
- [68]. Huang, H., & Talreja, R. (2005). Effects of void geometry on elastic properties of unidirectional fiber reinforced composites. *Composites Science and Technology*, 65(13), 1964-1981.
- [69]. Ricotta, M., Quaresimin, M., & Talreja, R. (2008). Mode I strain energy release rate in composite laminates in the presence of voids. *Composites Science and Technology*, 68(13), 2616-2623.
- [70]. Lopes, C. S., Remmers, J. J., & Gürdal, Z. (2008). Influence of porosity on the interlaminar shear strength of fibre-metal laminates. *Key Engineering Materials*, 383, 35-52.
- [71]. Zhu, H., Wu, B., Li, D., Zhang, D., & Chen, Y. (2011). Influence of voids on the tensile performance of carbon/epoxy fabric laminates. *Journal of Materials Science & Technology*, 27(1), 69-73.

- [72]. Lambert, J., Chambers, A. R., Sinclair, I., & Spearing, S. M. (2012). 3D damage characterisation and the role of voids in the fatigue of wind turbine blade materials. *Composites Science and Technology*, 72(2), 337-343.
- [73]. ASTM Standard D6415/D6415M (2006). Standard test method for measuring the curved beam strength of a fiber-reinforced polymer-matrix composite. West Conshohocken, PA, USA: ASTM International, 2006.
- [74]. Jackson, W. C., & Martin, R. H. (1993). An interlaminar tensile strength specimen. *ASTM SPECIAL TECHNICAL PUBLICATION*, 1206(11), 333-354.
- [75]. Reddy, J. N. (1987). A generalization of two-dimensional theories of laminated composite plates. *Communications in Applied Numerical Methods*, 3(3), 173-180.
- [76]. Drugan, W. J., & Willis, J. R. (1996). A micromechanics-based nonlocal constitutive equation and estimates of representative volume element size for elastic composites. *Journal of the Mechanics and Physics of Solids*, 44(4), 497-524.
- [77]. Hashash, Y. M. A., Jung, S., & Ghaboussi, J. (2004). Numerical implementation of a neural network based material model in finite element analysis. *International Journal for numerical methods in engineering*, 59(7), 989-1005.
- [78]. ABAQUS 6.11. User's manual. Pawtucket (RI): ABAQUS, Inc.; 2011.
- [79]. He, Y., Makeev, A., & Shonkwiler, B. (2012). Characterization of nonlinear shear properties for composite materials using digital image correlation and finite element analysis. *Composites Science and Technology*, 73, 64-71.
- [80]. Ramberg, W., & Osgood, W. R. (1943). *Description of stress-strain curves by three parameters*. National advisory committee for aeronautics.
- [81]. Sandhu, R. S. (1976). Nonlinear behavior of unidirectional and angle ply laminates. *Journal of Aircraft*, 13(2), 104-111.
- [82]. Camanho, P. P., Dávila, C. G., Pinho, S. T., Iannucci, L., & Robinson, P. (2006). Prediction of in situ strengths and matrix cracking in composites under transverse tension and in-plane shear. *Composites Part A: Applied Science and Manufacturing*, 37(2), 165-176.
- [83]. Fagiano, C., Abdalla, M. M., & Gürdal, Z. (2010). Interlaminar stress recovery of multilayer composite shell structures for three-dimensional finite elements. *Finite Elements in Analysis and Design*, 46(12), 1122-1130.
- [84]. Pipes, R. B., & Pagano, N. J. (1970). Interlaminar stresses in composite laminates under uniform axial extension. *Journal of Composite Materials*, 4(4), 538-548.
- [85]. Makeev, A., & Armanios, E. A. (2000). An iterative method for solving elasticity problems for composite laminates. *Journal of applied mechanics*, 67(1), 96-104.
- [86]. Lemaitre, J., & Chaboche, J. L. (1978). Aspect phénoménologique de la rupture par endommagement. *J Méc Appl*, 2(3).
- [87]. Bazant, Z. P., & Cedolin, L. (1979). Blunt crack band propagation in finite element analysis. *Journal of the Engineering Mechanics Division*, 105(2), 297-315.



- [88]. Pietruszczak, S. T., & Mroz, Z. (1981). Finite element analysis of deformation of strain-softening materials. *International Journal for Numerical Methods in Engineering*, 17(3), 327-334.
- [89]. ASTM Standard D5766 (2007). Standard Test Method for Open-Hole Tensile Strength of Polymer Matrix Composite. *West Conshohocken, PA, USA: ASTM International*, 2007.
- [90]. ASTM Standard D7615 (2011). Standard practice for open-hole fatigue response of polymer matrix composite laminates. *West Conshohocken, PA, USA: ASTM International*, 2011.
- [91]. ASTM Standard D6484/D6484M (2009). Standard Test Method for Open-Hole Compressive Strength of Polymer Matrix Composite. *West Conshohocken, PA, USA: ASTM International*, 2009.
- [92]. Hounsfield, G. N. (1973). Computerized transverse axial scanning (tomography): Part I. Description of system.
- [93]. Schilling, P. J., Karedla, B. R., Tatiparthi, A. K., Verges, M. A., & Herrington, P. D. (2005). X-ray computed microtomography of internal damage in fiber reinforced polymer matrix composites. *Composites Science and Technology*, 65(14), 2071-2078.
- [94]. Stock, S. R. (1999). X-ray microtomography of materials. *International Materials Reviews*, 44(4), 141-164.
- [95]. Bracewell, R. N., & Riddle, A. (1967). Inversion of fan-beam scans in radio astronomy. *The Astrophysical Journal*, 150, 427.
- [96]. Curry, T. S., Dowdey, J. E., & Murry, R. C. (1990). *Christensen's physics of diagnostic radiology*. Lippincott Williams & Wilkins.
- [97]. Nikishkov, Y., Airolidi, L., & Makeev, A. (2013). Measurement of voids in composites by X-ray Computed Tomography. *Composites Science and Technology*, 89, 89-97.
- [98]. Lekhnitskii, S. G. (1968). *Anisotropic plates* (No. FTD-HT-23-608-67). FOREIGN TECHNOLOGY DIV WRIGHT-PATTERSON AFB OH.
- [99]. Whitney, J. M., & Nuismer, R. J. (1974). Stress fracture criteria for laminated composites containing stress concentrations. *Journal of Composite Materials*, 8(3), 253-265.
- [100]. Chiang, C. R. (2008). Stress concentration factors of a general triaxial ellipsoidal cavity. *Fatigue & Fracture of Engineering Materials & Structures*, 31(12), 1039-1046.
- [101]. Gomes, J. (Ed.). (1999). *Warping and morphing of graphical objects* (Vol. 1). Morgan Kaufmann.

## Biographical Information

Guillaume Seon began his bachelor studies in Aerospace Engineering in 2004 at the Institut Supérieur de l'Aéronautique et de l'Espace (ISAE) – SUPAERO in Toulouse, France. In 2006, he started a 10-month engineering Co-op position at SAFRAN-Herakles in Bordeaux, France, where he worked on the development of FE simulation methods for the dynamic response of composite structures subject to vibratory and acoustic environments. He received his Master of Science in Aerospace Engineering from ISAE-SUPAERO in June 2007. In August 2007, he started a Master's Degree program abroad at the Aerospace Engineering department of the Georgia Institute of Technology, Atlanta, USA, under the supervision of Dr. Makeev. He received his Master of Science in Aerospace Engineering from Georgia Tech in Spring 2009. From April 2009 to January 2012, he worked as an aerospace engineer at SAFRAN-Herakles in Bordeaux, France. His responsibilities included the post-launch vibratory analysis of the Solid Rocket Engines of the European Space launcher Ariane 5 and technical support in structural dynamics for the design and certification of the thermal protection system of the ESA IXV (Intermediate eXperimental Vehicle) re-entry spacecraft demonstrator. In Spring 2012, Guillaume Seon left SAFRAN-Herakles to pursue his academic education with a doctoral degree in Aerospace Engineering at the University of Texas at Arlington, under the advisement of Dr. Makeev. His research at UT Arlington has been focused on the development of Finite Element based failure prediction methods for polymer composites. His interests include structural dynamics analysis and prediction of performance of composite structures for aerospace applications.